SAND REPORT

SAND2002-0699
Unlimited Release
Printed March 2002

Mechanisms of Atmospheric Copper Sulfidation and Evaluation of Parallel Experimentation Techniques

J. C. Barbour, J. P. Sullivan, M. J. Campin, A. F. Wright, N. A. Missert,
J. W. Braithwaite, K. R. Zavadil, N. R. Sorensen, S. J. Lucero, W. G. Breiland,
and H. K. Moffat

Prepared by
Sandia National Laboratories
Albuquerque, New Mexico 87185 and Livermore, California 94550

Sandia is a multiprogram laboratory operated by Sandia Corporation,
a Lockheed Martin Company, for the United States Department of
Energy under Contract DE-AC04-94AL85000.

Sandia National Laboratories

Issued by Sandia National Laboratories, operated for the United States Department of Energy by Sandia Corporation.

Available to DOE and DOE contractors from
U.S. Department of Energy
Office of Scientific and Technical Information
P.O. Box 62
Oak Ridge, TN 37831

Telephone: (865)576-8401
Facsimile: (865)576-5728
E-Mail: reports@adonis.osti.gov
Online ordering: http://www.doe.gov/bridge

Available to the public from
U.S. Department of Commerce
National Technical Information Service
5285 Port Royal Rd
Springfield, VA 22161

Telephone: (800)553-6847
Facsimile: (703)605-6900
E-Mail: orders@ntis.fedworld.gov
Online order: http://www.ntis.gov/ordering.htm

=- SAND2002-0699
Unlimited Release
Printed March 2002

Mechanisms of Atmospheric Copper Sulfidation and Evaluation of Parallel Experimentation Techniques

J. C. Barbour, J. P. Sullivan, M. J. Campin, A. F. Wright, and N. A. Missert
Nanostructure and Semiconductor Physics Department

J. W. Braithwaite, K. R. Zavadil, N. R. Sorensen and S J. Lucero
Corrosion Science and Technology Department

W. G. Breiland
Chemical Processing Science Department

H. K. Moffat
Multiphase Transport Processes Department

Sandia National Laboratories
P.O. Box 5800
Albuquerque, NM 87185-1415

Abstract

A physics-based understanding of material aging mechanisms helps to increase reliability when predicting the lifetime of mechanical and electrical components. This report examines in detail the mechanisms of atmospheric copper sulfidation and evaluates new methods of parallel experimentation for high-throughput corrosion analysis. Often our knowledge of aging mechanisms is limited because coupled chemical reactions and physical processes are involved that depend on complex interactions with the environment and component functionality. Atmospheric corrosion is one of the most complex aging phenomena and it has profound consequences for the nation's economy and safety. Therefore, copper sulfidation was used as a test-case to examine the utility of parallel experimentation. Through the use of parallel and conventional experimentation, we measured: (1) the sulfidation rate as a function of humidity, light, temperature and O_2 concentration; (2) the primary moving species in solid state transport; (3) the diffusivity of Cu vacancies through Cu_2S; (4) the sulfidation activation energies as a function of relative humidity (RH); (5) the sulfidation induction times at low humidities; and (6) the effect of light on the sulfidation rate. Also, the importance of various sulfidation mechanisms was determined as a function of RH and sulfide thickness. Different models for sulfidation-reactor geometries and the sulfidation reaction process are presented.

CONTENTS

1.0 Introduction

Degradation of mechanical and electrical components through materials aging consumes enormous amounts of energy in reduced functionality and cost. Government estimates [1] put the annual cost of corrosion alone at over $100 billion. This degradation of components often results from a complex phenomenon in which materials are exposed to an environment that invokes many coupled chemical reactions and physical processes. In particular, corrosion of electrical components has been identified as a leading concern for the Department of Energy (DOE) technologies and so a predictive understanding of material corrosion is key to reducing the economic burden of the DOE in its missions.

The basis for developing predictive capabilities is physics-based mechanistic understanding of the relevant degradation processes. At this time, most predictive capabilities are limited to relatively simple, single degradation processes (e.g., mechanical stress). The challenge at this point is to formulate similar capabilities for the many forms of substantial degradation that involve complex, coupled processes. These processes may include wear, fatigue, fracture of many types, plastic deformation, and corrosion of many types. Of these, corrosion is one of the most complex phenomena. Our hypothesis in this project was that unexpected corrosion often occurs because of synergistic, coupled phenomena which are inadequately predicted from traditional serial experimentation. Therefore, a key component of our work was to identify where unexpected corrosion mechanisms could occur and determine methodologies for this identification. One such approach is to map the corrosion mechanisms in the complex "corrosion-phase-space" and determine where boundaries between mechanisms occur by developing and apply emerging parallel-experimentation techniques. The ultimate goal of any such endeavor is to build all of the tools to determine the corrosion mechanisms which can then form the physical basis for a predictive mathematical/computer model. This project provided major inroads toward that endeavor and identified new areas of research that should be pursued to its end.

A primary focus of the work was on mapping the atmospheric corrosion of copper in a sulfidizing environment. The resulting methodology may later be applied to other forms of corrosion and to other degradation mechanisms such as wear, interface delamination, and thermomechanical fatigue. To ultimately be useful, the mechanistic information must be available in a clearly understandable format. Our goal is to define or map the complex phase space in which the corrosion of copper exists, for example like the hypothetical diagram presented in Fig. 1.1a. Such mechanism maps are plots of the dominant material response of multiple independent variables. The 2D map in Fig. 1.1b represents a slice taken from that multidimensional corrosion-space map. For example, mechanism A for Cu sulfidation might be gas-phase limited transport and mechanism B might be solid-state limited transport. In fact, much like the lever rule is used with binary phase diagrams, the predominance of mechanism A over B in a two-mechanism region (depicted as cross-hatch region) may be deduced through a lever rule.

This mapping of mechanistic information is not a new concept as demonstrated by the two examples shown in Figs. 1.1c and 1.1d. The Pourbaix diagram (Fig. 1.1c) defines regions of potential corrosion in the limited dimensions of solution pH and electrochemical potential. These diagrams show the relative equilibrium stabilities of solid phases and soluble ions that are produced by reaction between metal and aqueous environments. Thus, regions where corrosion is impossible or where passivating oxide layers would be formed are identified. However, no kinetic information is available because these diagrams are based solely on thermodynamics. The desire in this project is to extend this concept to map mechanisms in real multi-dimensional corrosion space. Then, regions where one primary mechanism or phenomenon applies are identified as well as regions where unexpected corrosion could occur from presently unknown effects of synergistic coupled mechanisms. A product closer in principle to this desire is the deformation-mechanism map for Ni given in Fig. 1.1d. This figure was derived by solving the various constitutive equations for each deformation mechanism with recognition given to respective mechanistic interdependencies or independences. The map reveals over which parameter range a particular mechanism is dominant (within its stress-temperature boundary) [3-5].

Atmospheric corrosion is an important degradation mode observed in many electrical and

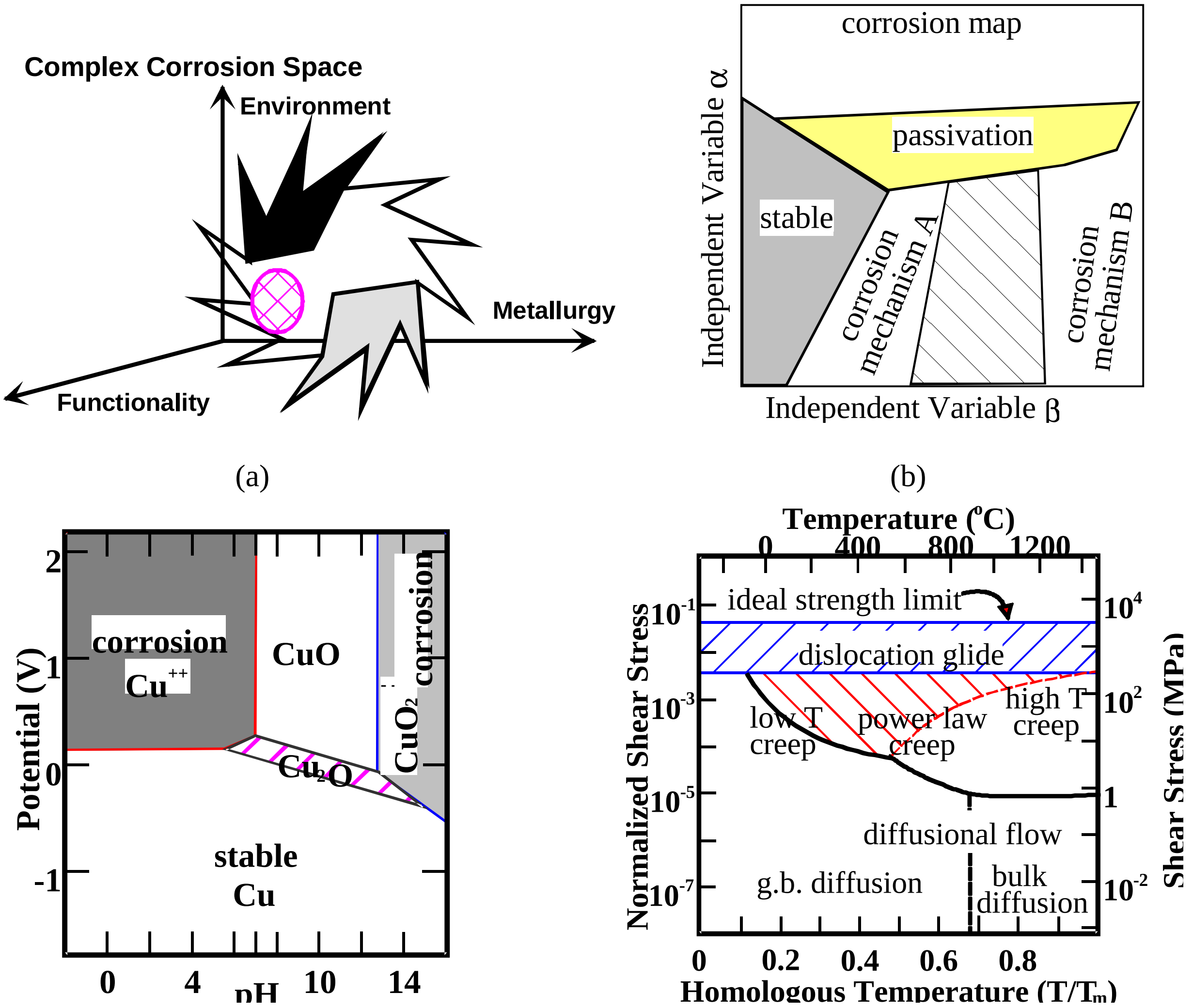

(a) (b)

(c) (d)

Fig. 1.1. Mechanistic phase space diagrams: (a) 3D and (b) 2D hypothetical representations for a complex corrosion process, (c) first generation corrosion diagram for copper [2] (Pourbaix), (d) deformation mechanism map for nickel [3].

electronic components. To assess the effects of corrosion on the performance and reliability of these types of devices, we are developing a comprehensive science-to-engineering tool-set. For this tool-set to be truly predictive, a mechanistic understanding of the relevant corrosion processes must be incorporated. Computational considerations (e.g., multi-dimension device length scales, simulation time) require the core of the tool-set to be a deterministic, continuum-level mathematical model. The capability to perform uncertainty analyses must also be included to permit the stochastic nature of corrosion and variable environmental conditions to be addressed. The primary output from the tool-set will consist of a time-based distribution of a material property change (e.g., electrical resistance). To ultimately determine reliability, this distribution must be input into age-aware electrical models of component/system performance.

An analysis of the historical occurrences of corrosion in our hardware systems led to the identification of two general types of corrosion that degrade the performance of electrical devices: (I) product layer growth and (II) metallization voiding. In Type I corrosion, the product layer either forms an undesirable resistive barrier (e.g., on connectors, contacts), or an undesirable conductive layer (e.g., across a diode). Type II corrosion typically results in the electrical opening of conductive lines (e.g., nichrome wire in resistor or aluminum line in an integrated circuit).

This report describes the results of a study that was performed specifically to identify how and at what rate copper sulfidizes under atmospheric conditions. This information is applicable to corrosion that occurs on contacts and connectors. It constitutes the physics/mechanistic foundation required in our analytical model and also provides many of the materials properties needed in actual simulations (e.g., ionic diffusivity, kinetic rate constants).

2.0 Project Objectives and Approach

The objectives of this project were two fold: 1) determine the utility of combinatorial experimentation approaches for rapidly performing physical-chemistry experiments and 2) build a tool-set for understanding atmospheric copper sulfidation mechanisms. The work resulting from these objectives is presented in sections 4 and 5 with concluding interpretation given in sections 6 and 7. First, note that the combinatorial approach when applied to solid-state physical chemistry was found to be closer in kind to parallel-experimentation using miniature laboratories. In order to perform these experiments to gain quantitative analysis then ultrasensitive microanalytical techniques are needed to efficiently explore this phase space that is the combinatorial microlab. Several approaches to microanalytical experiments were developed and will be described in this report. Combinatorial experiments (arrays of microlabs) were used to determine relative synergistic effects of metallurgical variables (alloying, defect density in the Cu oxide and bulk) and functionality (e.g., electric-current conduction). Also, the effects of environmental variables were examined such as the sulfur content in air, light exposure, and relative humidity. Traditional experimentation was also used where needed, such as the use of marker experiments to determine primary moving species in solid-state diffusion transport through growing Cu_2S product layers at different relative humidities. Novel diagnostics were developed, including a planar microelectrode sensor platform for making corrosion chemistry measurements, and the use of a stable pH sensor for atmospheric environments was demonstrated. A qualitative detection scheme was shown also for O_2 partitioning into adsorbed, low dimensional H_2O films responsible for driving atmospheric corrosion. In-situ electrical conductivity, light scattering, X-ray photoelectron spectroscopy (XPS), transmission electron microscopy (TEM), scanning electron microscopy (SEM), and X-ray diffraction were used to monitor corrosion reactions.

Finally, an important component of this experimental approach was the exposure to atmospheric environments with very controlled gas flow characteristics. Therefore, considerable attention will be given in this report to the design and implementation of a well controlled sulfidizing reactor termed the stagnation-flow reactor (see section 4.2 and appendix A).

3.0 General Copper Sulfidation Behavior

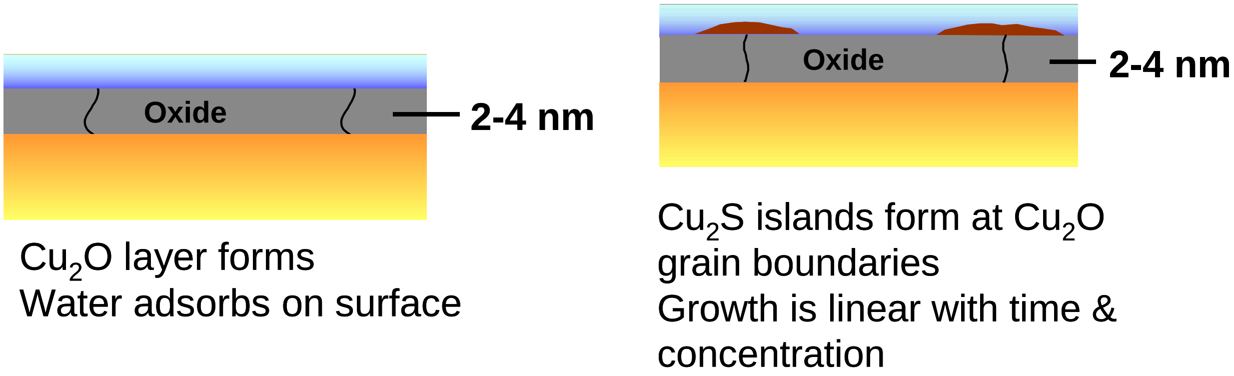

(a) Initial exposure to humid atmosphere

(b) Early part of Stage-I

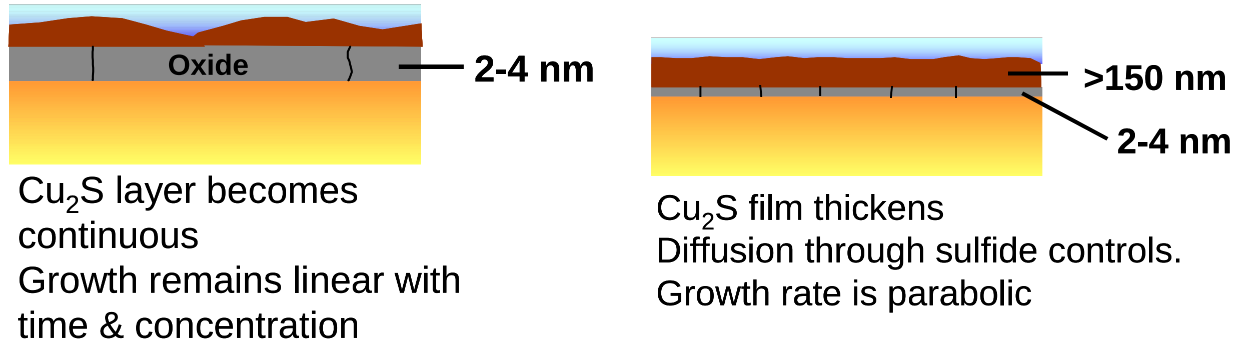

(c) Advanced Stage-I

(d) Stage-II

Fig. 3.1 Schematic representation of the processes involved with the two primary stages of copper sulfidation. These stages and descriptions are based on the information presented by Graedel and co-workers [6, 7].

Copper is an important, widely used material in a number of high-reliability electrical applications, including those associated with the telecommunications, transportation, and defense industries. These widespread uses coupled with its thermodynamic instability in most terrestrial environments have motivated numerous atmospheric copper corrosion studies over the years. To enable a clearer understanding of why the approach noted in the section above was selected and specifically why the various techniques were developed and subsequent measurements made, this section presents some information about the general characteristics of copper sulfidation. Of note, some of the details associated with this information will become clearer in Sections 4 and 5. In general, the goal of previous investigators was to characterize and mitigate any detrimental corrosion effects. Contrary to the corrosion processes that occur on many engineering alloys in which localized attack is prevalent, corrosion of copper has been typically viewed as a "relatively simple" uniform phenomenon [1,6-9] (modeled pictorially in figure 3.1) with the following processes proposed by Graedel and co-workers [6,7]:

1. <u>Copper oxidation and water adsorption:</u> upon exposure of a bare copper surface to an atmosphere containing water and/or oxygen, the surface rapidly oxidizes, forming a Cu_2O layer approximately 2-4 nm thick that covers the entire surface. In the initial stage of the corrosion process, a layer of "water" adsorbs on the Cu_2O surface, coming to equilibrium relatively quickly and at a thickness primarily dependent on the relative humidity (RH) [10]. At RH levels > 80%, the equivalent of several monolayers of water are thought to be present which constitute an aqueous quasi-solution phase. At moderate RH levels (20-80%), the surface is covered, on average, by at least one monolayer. At low RH (<20%), the average water layer is not even one monolayer thick. However, the water film is believed to exist in clusters or puddles at all RH levels. Thus, local water thickness should exceed the average thickness [11].

2. <u>Sulfidation reaction – Stage I:</u> sulfur containing reactants interact at the "water" oxide interface, possibly at Cu oxide grain-boundaries. During this stage, solid-state diffusion of Cu through Cu_2O is thought to control the kinetics of Cu_2S island growth on Cu_2O. The thin islands of copper sulfide that form eventually grow laterally until a uniform but porous film exists. Further sulfidation then occurs at the sulfide-water surface. The rate may be controlled by the supply of H_2S to the surface, and is thus linear with both time and the supply of H_2S (ppm-hr). Copper metal oxidation itself must occur at the metal/oxide interface. Such a process is possible because of the relatively good conductivity of Cu_2S (ionic and electronic) and Cu_2O (electronic). The cuprous ions and electrons that result from the oxidation diffuse to the external surface where the sulfidation reactions occur.

The presence of adsorbed water layers significantly affects the sulfidation rate and the general response is usually represented by a sigmoidal curve [12]. If the RH is < 20%, the sulfidation rate was thought to be minimal. The reaction process was essentially dry, thus requiring a direct gas-metal ambient-temperature interaction. At the moderate RH levels, up to a few monolayers of water are present on the surface and several rate enhancing processes occur: (1) the very soluble H_2S dissolves, forming more chemically active and available HS^- and H^+ ions, (2) accommodation coefficients increase (fraction of H_2S molecules striking surface and adsorbing), and (3) water is available to catalyze or effect coordination-chemistry related electrochemical charge-transfer reactions. At high RH levels (>80%), the sulfidation rate should dramatically increase, reaching levels 10 times the dry sulfidation rate. The average critical H_2O thickness appears to be about 3+ monolayers. At this point, the quasi-aqueous phase exists and absorption of H_2S can occur. The ionic species are more mobile, more reactants are dissolved into solution, and other electrochemical (e.g., galvanic) effects become operative.

3. <u>Sulfidation reaction – Stage II</u>: As the Cu_2S sulfide product layer thickens to beyond about 150 nm, the sulfidation rate becomes independent of the rate of H_2S supply and control shifts to diffusion of a reactant or product through the layer's restricted defect structure.

However, we have learned that the actual Cu corrosion mechanism(s) are far more complicated than the literature had initially indicated. Relatively thick sulfide layers were

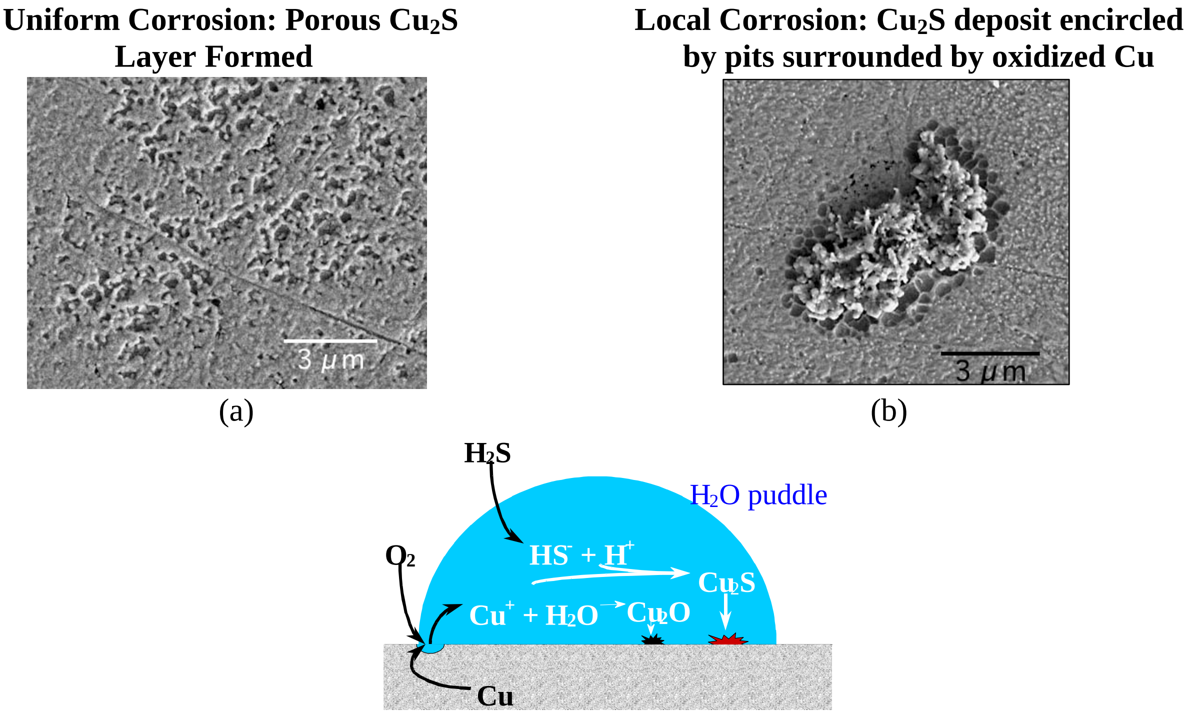

(c)

Fig. 3.2. SEM images of Cu surface after about sulfidation at 67% RH (a), and 40% RH (b). Equal quantities of Cu_2S are formed, but the entire surface in (a) is Cu_2S except for observable pores, whereas the only Cu_2S present in (b) is the flowery deposit within the "pitted" region. (c) The lower figures depict possible sulfidation mechanisms that may occur in a puddle of water on an oxidized Cu surface.

formed with variable morphology in a wide range of environmental conditions and in fact discontinuous flowery-rosette structures encircled by pits can be formed as shown in Fig. 3.2b.

The mechanisms for this Cu_2S growth is clearly more complex than the simple model proposed by Graedel [9] for atmospheric sulfidation of Cu single crystals.

The following two examples demonstrate the complexity of understanding the key mechanisms that control copper corrosion. First, a conventional, serial experimental approach was undertaken to identify the kinetics of flat-plate copper sulfidation as a function of several environmental variables and it was determined that in some circumstances the sulfidation rate could be an order of magnitude greater than predicted from the work of Graedel. The cause of this enhanced corrosion rate is assumed to result from synergistic coupled mechanisms which depend upon environmental variables. A second, somewhat perplexing observation was obtained during the same sulfidation study. A small change in the RH produced dramatic differences in corrosion product morphology as shown in Fig. 3.2, yet the overall sulfidation rate (as determined by mass change) remained quite similar. A further complication to this observation was that at even higher humidity levels (>80%), the morphology changed again such that the typical Stage-II parabolic growth kinetics were never produced. For this latter situation, SEM examination did not identify any discernable morphology differences. The kinetic results from these examples possibly indicate that gas-phase mass transport may control the initial rate. However, the apparent lack of dependence on humidity is certainly contrary to the normally accepted belief that the corrosion rate dependence on humidity is sigmoidal.

Product-layer morphological changes can be important from a practical perspective (e.g., effect on function of electrical devices). The unexpected morphology results described above may be due to poorly understood coupled processes involving adsorbed water puddle spatial distribution and thickness, speciation of absorbed chemicals, and corrosion product (Cu_2S and Cu_2O) nucleation and growth. The quantity of adsorbed water primarily depends on the humidity level. However, its distribution probably depends on many surface-related factors including the characteristics of the native oxide layer. If the water puddles are indeed more spatially separated at lower humidity, but also much larger, then the corrosion could proceed as depicted in the schematic Fig. 3.2c. Initial pitting would logically occur along the edges of the puddle where the oxygen concentration is highest. Alternately, with more-or-less full surface coverage at the higher humidity levels (schematic below Fig. 3.2a), nucleation is adequate and the entire surface is effectively covered with water and the deposit uniformly grows at the macroscopic level.

Overall, copper corrodes under atmospheric conditions that contain H_2S according to the following reaction:

$$H_2S + 2Cu + \tfrac{1}{2}O_2 \rightarrow Cu_2S + H_2O \tag{1}$$

The kinetics of the reaction can therefore be affected by environmental conditions (temperature, O_2 and H_2S partial pressures, and RH) and by physical properties (e.g., Cu^+ and H_2S diffusivity). Importantly, thermodynamics can be used to show that an oxidant (e.g., O_2) must be present. That is, the hydrogen contained in H_2S and H_2O will not oxidize copper. X-ray diffraction studies performed here and by previous investigators have confirmed that cuprous sulfide ($\sim Cu_2S$) is the primary product formed under these conditions.

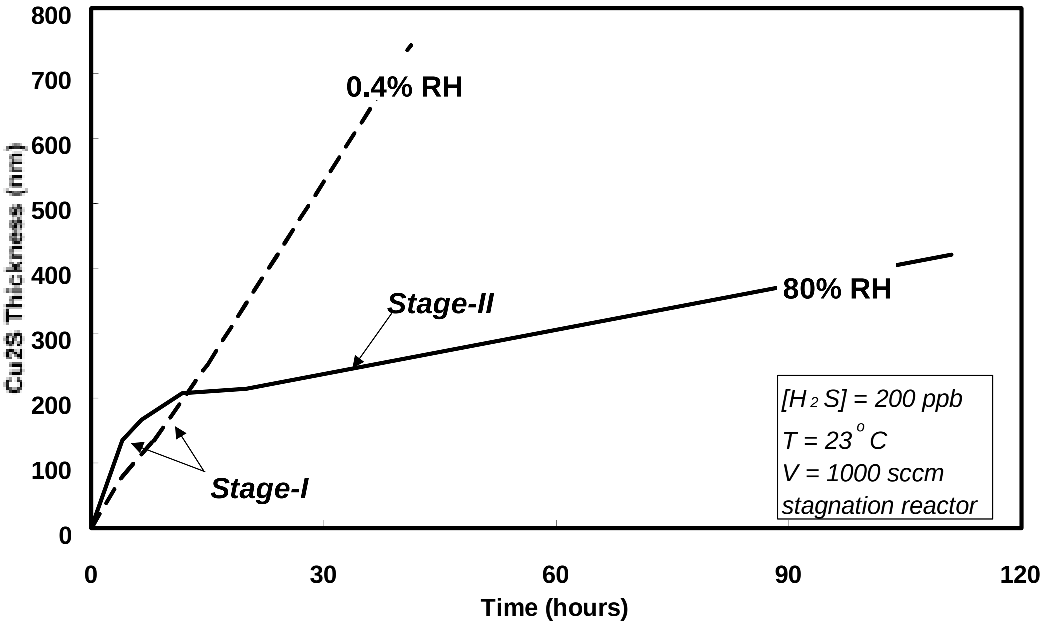

Fig. 3.3 Two stages of copper-sulfide film growth: linear Stage I and “parabolic” Stage II.

In Summary, Graedel and co-workers earlier showed that the growth of copper-sulfide films occurs in two distinct stages [6-8]. They proposed the chemical and physical processes schematically depicted in figure 3.1 are relevant. The kinetic characteristics shown in figure 3.3 typically result. Stage-I kinetics are linear and first-order with respect to the concentration of H_2S in the gas phase [H_2S] and are controlled either by a surface reaction or by gas-phase mass transport. Stage-II is proposed to be controlled by diffusion of Cu^+ ions through the thickening product layer and thus the kinetics have a relatively parabolic shape. Graedel also noted that the thickness of copper sulfide that is observed on fielded copper components associated with the telecommunications industry normally does not exceed about 150 nm, a value reported to be similar to the thickness at which the transition from Stage-I to Stage-II occurs. However, in our applications, we have seen copper-sulfide thickness levels that have exceeded 1 μm on field-returned electrical devices.

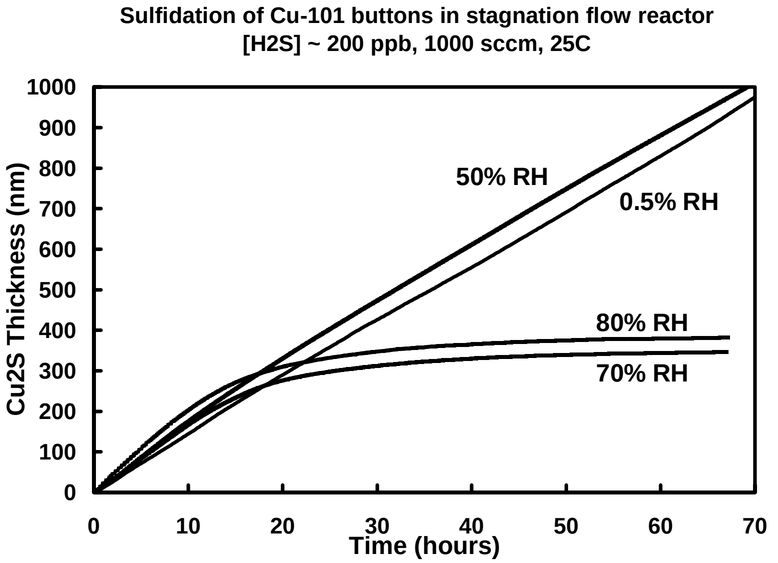

(a)

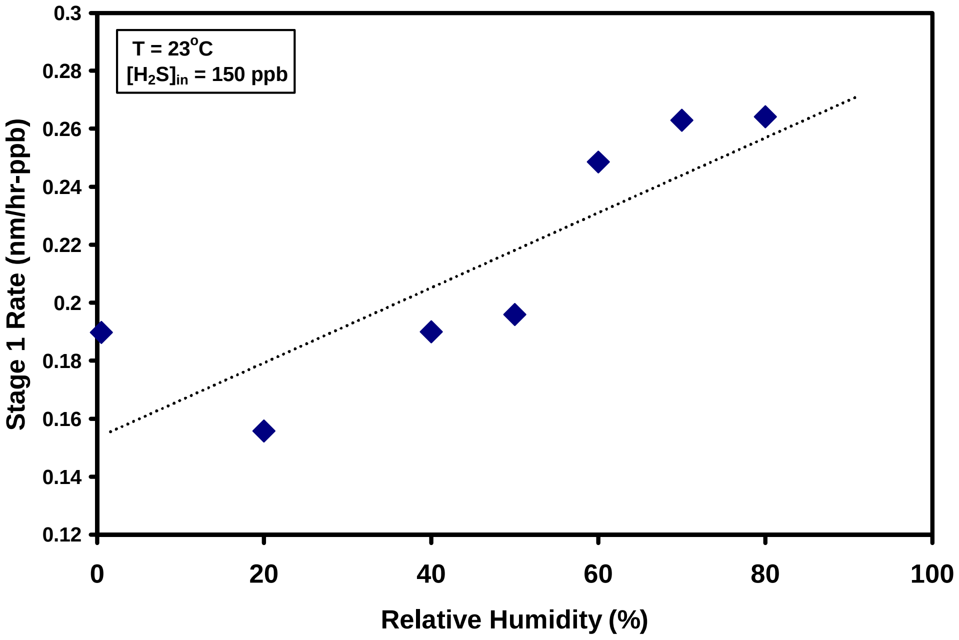

(b)

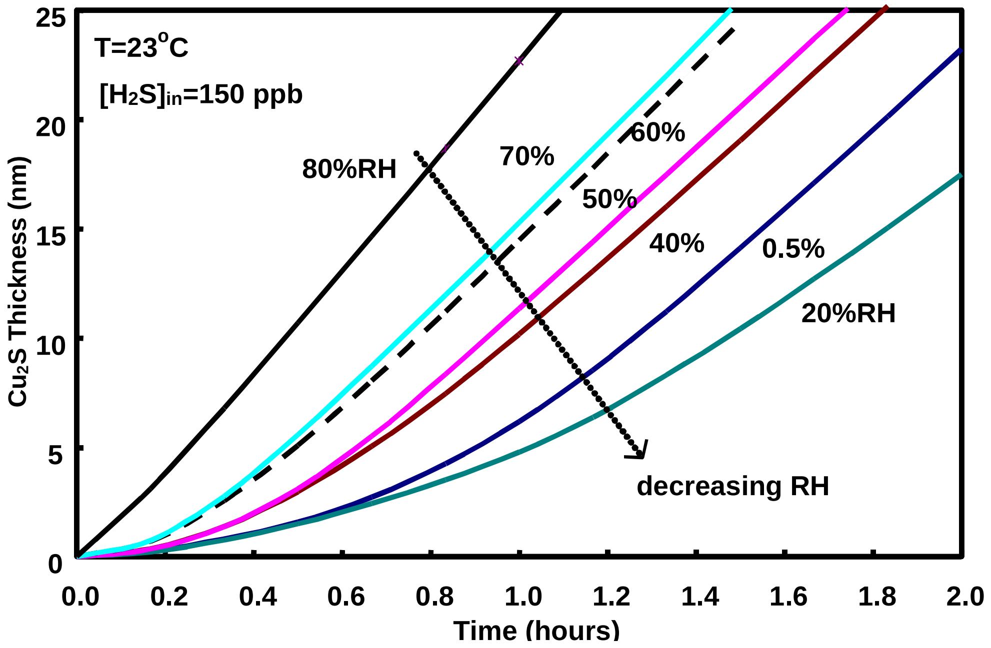

(c)

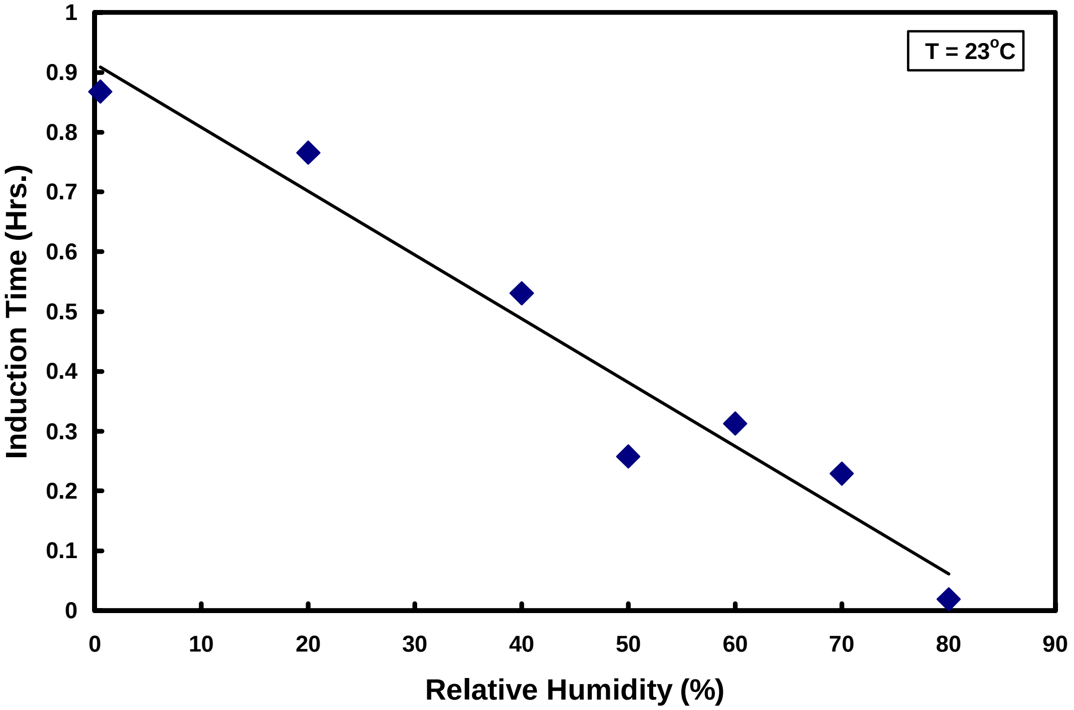

(d)

Fig. 3.4 Effect of RH on several aspects of copper sulfidation: (a) general kinetics (Cu_2S thickness vs. time), (b) Stage-I rate (initial linear portion of (a), (c) existence of an induction time (plot of data similar to that in (a) except at very short time), and (d) actual induction times as f(RH). (Note the anomalous behavior exhibited by the higher sufidation rate for 0.5% RH shown in figures (b-c) requires further work to identify if caused by a change in mechanisms)

Further interesting general characteristics of copper sulfidation are evident from our studies of the effect of relative humidity. As shown in figure 3.4a, at low to moderate humidity levels, the transition to Stage-II is not observed even at relatively significant Cu_2S thickness levels. The rate of reaction during Stage-I (the initial linear portion) increases slightly as the humidity increases (b,c). Another characteristic of the sulfidation process is the existence of an induction period, in which the process does not fully enter Stage-I for a small length of time (c) that is an inverse function of the humidity (d). This induction effect is probably related to some associated change in the character or properties of the native copper-oxide layer that involves interactions with water.

4.0 Advanced Characterization Techniques

4.1 Combinatorial/Parallel Experimentation

This section gives the description of an advanced experimental methodology used for addressing key issues and phenomena given above. The focus of this work was to develop a new tool, which we have termed the "Combinatorial Microdomain Laboratory" (combinatorial microlab), that combines parallel miniature experimentation with ultrasensitive microanalytical techniques. Many of the fundamental underpinnings for this tool were developed in this project but not all were fully implemented. One lesson that was learned in this project is that to perform combinatorial microlab experiments on condensed matter, with all of the parameters well controlled, takes a great deal of time, effort, and knowledge of the material-environment-interaction space. Also, free access to the microfabrication tools commonly used in microelectronics development and research was essential. Nevertheless, great advances were found and we learned that the combinatorial microlab can be used to explore corrosion space and identify mechanisms and kinetic parameters. In fact, early work brought recognition [13] in Science to our program as uniquely turning combinatorial chemistry on its head in order to unwrap the mechanisms behind complex phenomena. In this combinatorial microlab work, we are able to use parallel micro-laboratory experiments to screen the physical and chemical mechanisms occurring when classes of materials are exposed to different environmental factors and utilized in different functions. This technique also enables better standardization and environmental control between experiments. Using our selected experimental and analytical techniques, we have the opportunity to characterize processes that occur in the multivariable, corrosion space and identify the regions of well-established behavior and the regions of unexpected behavior. This section will describe the basics of the combinatorial microlab methodology and give specific design aspects for electrical resistance sensors and in-situ chemistry sensors.

We recognized that several specific topics must be included in a combinatorial microlab experiment of copper sulfidation. These include: (1) characterization of the copper oxide, water layer (including chemical speciation), and product layer as a function of RH, pH, pH_2O, pO_2, pH_2S, Cu-oxide species, temperature, point-defect level, and metallurgical composition, and (2) determination of the reactants and products transport in the gas, liquid and solid phases as a function of the changing morphologies of water and solid layers. An accurate determination of sulfidation mechanisms depends critically on understanding the close link between the rate of Cu sulfidation and the chemical composition and the flow conditions in the corrosive environment. Therefore, a separate section was dedicated to the design of the corrosive environment reactor

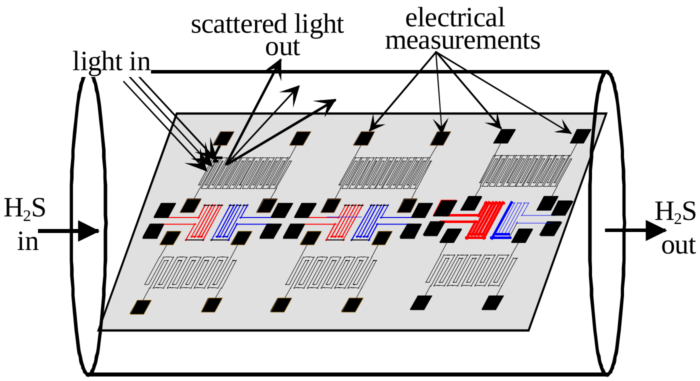

Fig. 4.1.1 Schematic - integrated Cu corrosion and environmental sensors measure the dependence of sulfidation on local pH_2S and pH_2O, and conductivity measurements are combined with light scattering measurements.

used in this work. Critical environmental parameters include pH_2O, pO_2, and pH_2S. In order to quantify the effect of each parameter, a great number of separate experiments are required or knowledge is required of the sulfidation reaction in real-time. In-situ microsensors and variable water-puddle test structures were developed and in the future will be integrated to measure and control the composition of the corrosive environment and thus the rate of sulfidation. Confined Cu volumes of different size (2-50 µm in width), will be used to design known thickness liquid layers and control the air exposure surrounding the water puddle on Cu. Microdomain sensor techniques developed under this project will be applied in combinatorial experiments (arrays of microlabs) to study atmospheric Cu corrosion. This combinatorial microlab approach differs from convention by focusing on microscopic length scales, the relevant scale for corrosion, and by quantitatively measuring both direct and synergistic effects in corrosion space.

Figure 4.1.1 provides a schematic representation of how these microsensors for H_2S and H_2O detection could be integrated with Cu meander-line corrosion monitors and light scattering experiments. Different conductivity sensors could be integrated to measure pH_2Sor pH_2O. All three conductivity sensors will be integrated within small mm-sized regions and repeated throughout the sample. For constant supply of H_2S, H_2O, and O_2, the reactant concentrations change as these three are depleted from the supply stream. This gives rise to changes in the downstream gas environment, thus permitting measurement of Cu sulfidation as a function of chemical environment all in one experimental run.

The combinatorial microlab approach to understand H_2S sulfidation of Cu actually started with a computational derivation of the difference in vacancy migration energies in copper and copper oxide doped with small amounts of In or Al. This work was suggested by work on $CuInSe_2$ and $CuInS_2$ solar cell materials [14] in which anti-site defects (In on Cu sites) are thought to trap Cu di-vacancies and thereby decrease the Cu mobility yielding an amazing tolerance and stability for highly defected solar cells. Solid-state diffusion of vacancies and di-vacancies in Cu, Cu_2O, CuO, and Cu_2S were thought to be key mechanisms in determining the kinetics of Cu sulfidation in one region of corrosion space. Cu atoms reach the liquid-solid interface through vacancy and di-vacancy diffusion, but the role and energetics of vacancy diffusion has eluded current macroscopic experiments. Historically, diffusion parameters (formation and migration energies) are difficult to determine, but by combining first-principles calculations with controlled combinatorial microlab experiments we will address the role of vacancy diffusion in corrosion product layer formation. Therefore, by varying the oxide thickness and oxide species in a first sample matrix, we could determine the relative passivation strength of the different types of oxide as well as test the mechanism of solid-state, diffusion-controlled growth by determining the amount of corrosion product formed for different thickness oxides.

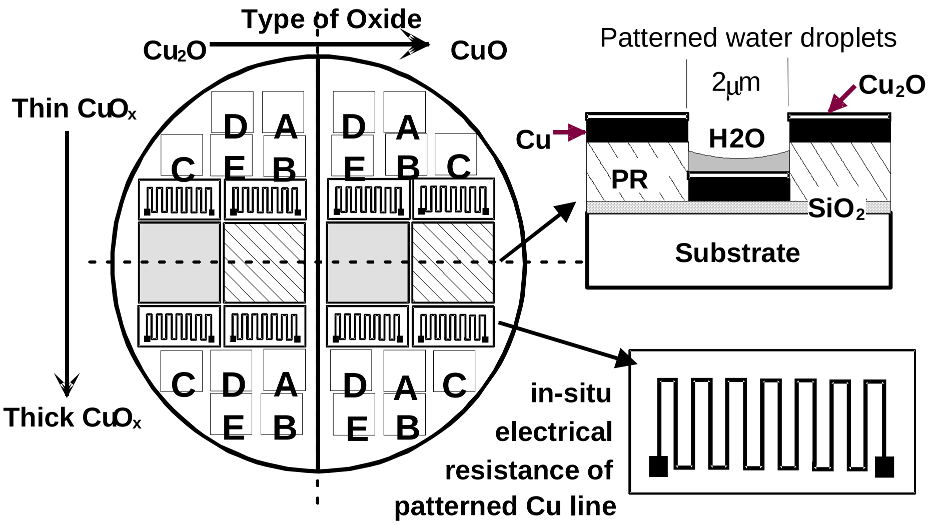

Fig. 4.1.2 Schematic view of a combinatorial microlab experiment using electron beam evaporation of Cu onto an inert substrate such as an oxidized Si wafer, and then using in-situ plasma oxidation techniques combined with masking to control the thickness and type of oxide formed (from pure Cu_2O to mixed oxide to pure CuO).

To this end, a simple matrix of parallel experiments was envisioned on a single wafer to begin testing some of these approaches and to gain knowledge about sulfidation parameters. A schematic view of such a matrix is shown in Fig. 4.1.2. Full integration of all of the “components” of this experiment have not yet been reached, but the preliminary results demonstrate the important role of copper oxide, point defects, and sample morphology. In fact, as described in sections below, an unexpected result was found that small Cu lines corrode faster than broad area samples – possibly due to competing mechanisms of gas-phase transport and solid-state transport, or the stress state in the Cu.

Copper films are electron beam evaporated onto SiO_2 coated Si wafers and then exposed in-situ to either a backfill of O_2 gas at 1 Torr pressure, or an electron cyclotron resonance (ECR) O_2 plasma. The corrosion rates from the deposited Cu was compared to that for “bulk” Cu 101 foils and found to be equal. The different O_2 exposures were meant to simulate a native dry-air-formed oxide for the O_2 backfill, and a more aggressive but controlled oxidizing environment in an O_2 plasma. The native oxide is predominantly Cu_2O while the ECR-grown oxide is fully oxidized to CuO at the surface and changes to Cu_2O at depth. The thickness of the ECR oxide layer is controlled by masking the sample to control the sample exposure time to the plasma. In addition, regions labeled A, B, C, D, and E in Fig. 4.1.2 represent sections of the sample in which either the alloy composition is varied by codeposition or by ion implantation, or in which the point defect level is varied by ion irradiation. Again the different regions are delineated by masking techniques: A = O_2 implant (compare 101 to O-rich Cu), B = bulk Cu defects (Cu implant), C = control (no implant), D = hydrogen stimulated defects (deuterium implant), E = vacancy traps (Al or In implant). As an example, the ion range and vacancy depth profiles for 200 keV Cu^+ ion implantation into an ECR-oxidized region is given in figure 4.1.3 for a fluence of $1x10^{14}$ ion/cm^2. The level of defect production can be varied with ion species, and ion energy.

The inner portions of the wafer show repeated meandering lines of Cu which are photolithographically patterned to form resistance lines for in-situ electrical resistance measurements to determine the corrosion rate and the effect of electron transport through the Cu lines on the corrosion rate. Each Cu meander line can be treated in a different fashion to test the effects of composition, point defect concentration, oxide species and oxide thickness. Finally, the gray and cross-hatched squares in the middle of the wafer represent test regions for varying the water environment. These portions of the wafer could be patterned to form arrays of openings which are: 1. smaller than the typical size of water droplets (e.g., 2μm diameter vias separated 10 μm apart, cross-hatch regions) forming a closed environment as shown at right in Fig. 4.1.2, or 2. larger than typical water droplets (e.g., 50μm diameter vias separated 400 μm apart, gray region) forming discontinuous patches of a water layer. The corrosion behavior of these two micro-environments could then be compared to that for the adjacent broader areas between the arrays of openings.

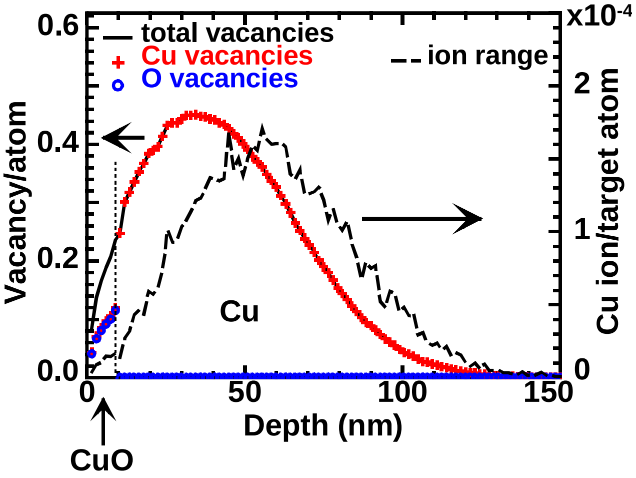

Fig. 4.1.3 Ion range and vacancy depth profiles for 200 keV Cu $^+$ ion implantation to a fluence of 1x10^{14} Cu/cm^2 were calculated using the TRIM-92 computer code. [15]

The simple combinatorial matrix shown in Fig. 4.1.4 demonstrates the important role played by point defects which were created in a dense plasma-grown oxide by Cu ion irradiation (the doping of Cu in the oxide layer is

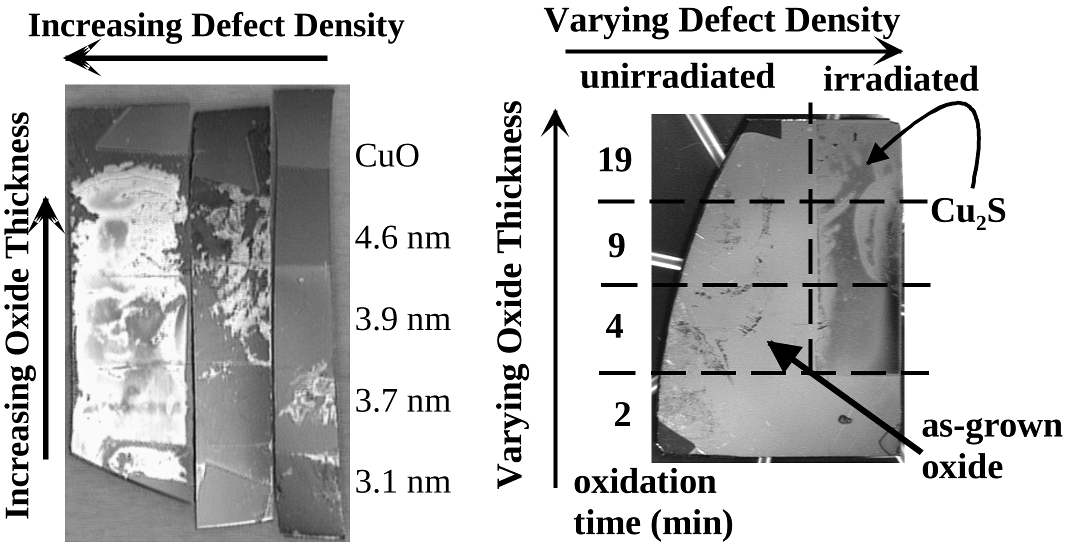

(a) (b)

Fig. 4.1.4. Optical image of a portion of a combinatorial matrix testing the effect of point defects and oxide thickness on Cu_2S formation. After growing different thicknesses of CuO for different oxidation times, the sample was irradiated with 200 keV Cu$^+$ ions to varying fluences. The fluences in (a) from right to left were 1x10^{12} Cu/cm^2, 1x10^{13} Cu/cm^2, and 1x10^{14} Cu/cm^2; and in (b) from left to right were unirradiated and 1x10^{15} Cu/cm^2. The samples were then sulfidized for 5.5 hours at 24 °C in a 65% RH environment containing 600 ppb H_2S.

negligible for these samples). The surface oxide was formed in an ECR O_2 plasma. In this figure, the strips of sample were irradiated with increasing fluence from right to left in (a) and from left to right in (b), and then this matrix was exposed to a sulfidizing environment. The quantity and uniformity of the Cu_2S layer formation was easily observed through optical imaging. The quantity of sulfide layer increased with increasing point defect levels but was independent of the oxide thickness. The air-formed oxide (not shown) exhibited the greatest amount of sulfidation and the unirradiated ECR-grown oxide (shown in b) exhibited no sulfidation.

This is a rather simple matrix experiment, but it demonstrates the power of performing twelve experiments simultaneously to determine that point defects are more important than oxide thickness in determining the kinetics of sulfidation. This type of experiment will be expanded below to incorporate the novel microscale diagnostics described above in order to measure the kinetics of the sulfidation reaction in real time. Further tests described below will compare increases and decreases in the vacancy concentration. To increase the vacancy concentration, Cu ions will be implanted in the oxide and Cu metal layers, and to decrease the vacancy concentration In and Al will be implanted. Ion beam analysis (IBA) from each of the different cells in the matrix of Fig. 4.1.4 helped to show how the sulfidation reaction proceeds. A detailed description of this analysis will be given in section 4.5 below.

Finally, note that for the air-formed Cu_2O and for the CuO layers irradiated to high fluences, the sulfidation does proceed in a more uniform fashion across the surface of the sample, but for low fluence irradiation the sulfidation process proceeds irregularly across the surface (or not at all for the unirradiated sample). The behavior of the samples irradiated to different fluence levels can be understood more fully by examining the XPS and Auger signals. The $Cu2p_{3/2}$ spectrum can show a shakeup peak which is characteristic [16,17] of Cu(II). In addition peak shifts from the other signals help identify the different forms of Cu present in the sample: Cu(II), Cu(I), and Cu^o. Analysis of the XPS data will be presented below in section 4.5. The analysis of the XPS shakeup peaks shows that even air-oxidized Cu contains some CuO in agreement with prior work on air-formed oxides. [18] Air-oxidized samples contain a greater proportion of Cu_2O than thick ECR-grown oxides, and a thin ECR oxide sample is a good intermediate mixture of Cu_2O and CuO. Ion irradiation creates point defects in the oxide and correspondingly the Cu(II) shakeup peak is reduced: suggesting that CuO is reduced to Cu_2O or Cu. The thermodynamics of possible reaction pathways suggests that by reducing CuO to Cu_2O (or Cu) permits the sulfidation reaction to proceed which is more thermodynamically favorable than sulfidation of CuO. Still, this tells us nothing about the kinetics of the reaction and the fact that a greater amount of sulfide formation occurs for the higher fluence irradiation may suggest that greater solid-state transport occurs for the higher fluence irradiation. It may be possible to systematically vary the quantity of CuO and Cu_2O in a combinatorial matrix by decreasing the fluence level, changing the ion species, or using electron irradiation.

Now consider the relative sulfidation rates for copper which contains excess point defects, or atomic species that trap vacancies. The sulfidation of both broad area samples and Cu meander-line samples was measured for ion-implantation doped samples and control samples. Resistance changes in Cu meander lines were used to determine absolute (and thereby relative) sulfidation rates of narrow lithographically patterned Cu lines as a function of exposure time to a sulfidizing atmosphere. The increase in the Cu_2S thickness is calculated from a decrease in Cu thickness which is deduced from a change in resistance. Two sets of samples were examined: one with a native oxide (Cu_2O) surface layer and one with a thin ECR oxide layer (mixed

Cu_2O/CuO layer). The samples were ion implanted with In, Al, O, and D to form a concentration of 0.5 at. % up to a depth of 150 nm, and implanted with Cu to produce the same atomic displacement damage profile as the In implantation. The sample resistivity was monitored continuously during the sulfidation exposure in order to determine changes in the sulfidation rate with time. In addition, two control samples (unirradiated) were monitored to examine possible effects of drawing current through the resistance lines while exposed to the sulfidizing environment: one drawing current continuously and the other tested at infrequent intervals to minimize the flow of current during the sulfidation. Finally, the total sulfide thickness after 290 min. of exposure was measured from IBA of the broad area samples and the meander lines (micro-focussed IBA). The results from these combinatorial experiments will be presented in later sections below, but first the experimental development for the electrical resistivity probes will be described in the next section.

4.1.1. Development of Electrical Characterization Microlabs

The atmospheric sulfidation of Cu at near-ambient temperatures and dilute H_2S concentrations produces monoclinic Cu_2S phase, low chalcocite, as the dominant reaction product. Similar to other mineral copper sulfide phases, this phase is a modest gap semiconductor with a band-gap of about 1.8 eV, as deduced from optical absorption on films chemically precipitated from solution.[19] In its native state, this phase is a p-type semiconductor with an electrical conductivity that depends to some extent on the nature of film formation. The p-type conductivity is believed to be due to the predominance of Cu vacancies over S vacancies in the material. This behavior is consistent with the observation that there exist a number of copper sulfide phases which are sub-stoichiometric in Cu, e.g. $Cu_{1.98}S$, $Cu_{1.8}S$, etc. The Cu_2S phases are characterized by a close-packed S sub-lattice combined with a low symmetry Cu sub-lattice. This Cu sub-lattice is distinguished by the presence of multiple nearly-equivalent sites that are not normally occupied by Cu but could contribute during Cu diffusion. The Cu is electropositive compared to the S, so, formally, a Cu vacancy would represent a site that could accept an electron, i.e. $V_{Cu}{}^0 + e^{'} \rightarrow V_{Cu}'$. Hence the concentration of Cu vacancies would be expected to be equal (at low vacancy concentrations) to the concentration of electronic acceptors in the Cu_2S. In this case, the electrical conductivity would be expected to follow the form

$\sigma = [V_{Cu}']e\mu_h$, where σ is the electrical conductivity, $[V_{Cu}']$ is the concentration of charged (occupied) Cu vacancies, and μ_h is the hole mobility.

Of course, incomplete occupancy of the acceptors, vacancy-vacancy interactions, vacancy-defect interactions, etc. would modify this form for the electrical conductivity. The important point, however, is that, to first approximation, the electrical conductivity would be expected to be proportional to the Cu vacancy concentration.

Electrical test structures can serve two purposes for understanding copper sulfidation: (1) they can be used as a simple corrosion monitor that provides a real-time signal of the amount of copper sulfidation that has occurred, or (2) they can be used to evaluate the electrical characteristics of the copper sulfide layer and, hence, provide clues as to how the concentration of electrically active defects changes with sulfidation conditions.

4.1.1.1. The electrical corrosion monitor.

The resistivity of pure bulk Cu is 1.7 x 10^{-6} Ωcm, while the resistivity of Cu_2S films is in the range of 5 x 10^{-3} to 3 x 10^{-2} Ωcm, depending on preparation and processing conditions of the films.[19] Due to the approximate 10^4 difference in resistivity, it is possible to construct simple resistance monitors to detect the degree of sulfidation of a Cu film. The construction is simple, a long, thin line of Cu is lithographically patterned atop an insulating layer. The resistance of this Cu line is monitored as this line is sulfidized in an atmospheric environment. The increase in line resistance due to sulfidation of the Cu is then directly proportional to the amount of copper remaining in the line or, by simple mass balance, the amount of copper sulfide that has formed.

$R_{meas} = L_{line}*\rho_{Cu}*\rho_{Cu2S}/(\rho_{Cu2S}*A_{Cu} + \rho_{Cu}*A_{Cu2S})$ where R_{meas} is the measured resistance of the sulfidized line of length, L, and the ρ's and A's are the resistivities and cross-sectional areas of the Cu and Cu_2S films.

If $\rho_{Cu2S} >> \rho_{Cu}$ (as expected) then, $R_{meas} \approx L_{line}*\rho_{Cu}/A_{Cu}$ or $A_{Cu}(\text{time} = t) \approx A_{Cu}(\text{time} = 0)*R_{meas}(\text{time} = 0) / R_{meas}(\text{time} = t)$. The area of copper sulfide that forms would then be expected to be $A_{Cu2S}(\text{time} = t) \approx [A_{Cu}(\text{time} = 0) - A_{Cu}(\text{time} = t)]*(\text{Cu atom density in Cu / Cu atom density in } Cu_2S)^{\dagger}$ If the width of the lithographically prepared Cu line is much greater than the thickness of the line, then to good approximation, the following expression would hold:

$H_{Cu2S}(\text{time} = t) = H * (\text{Cu atom density in Cu / Cu atom density in } Cu_2S) * \Delta R_{meas}(\text{time} = t) / R_{meas}(\text{time} = t)$ where H_{Cu2S} is the Cu_2S thickness, H is the original thickness of the Cu line, and $\Delta R_{meas}(\text{time} = t)$ is $R_{meas}(\text{time} = t) - R_{meas}(\text{time} = 0)$.

Hence the change in line resistance is directly proportional to the thickness of Cu_2S that has formed on the sample, and this can be used as a simple *in situ* monitor for copper sulfidation. It should be noted that the above analysis assumes that the sulfidation rate is spatially uniform along the line so that the cross-sectional area of Cu_2S that forms is equal at all points along the line. If the density of the Cu_2S that forms is significantly different than the theoretical density due to, for example porosity within the layer or at the Cu/Cu_2S interface, then the Cu_2S thickness needs to be scaled accordingly.

(†Assuming the bulk density of Cu_2S and Cu, Cu atom density in Cu / Cu atom density in $Cu_2S \approx 1.93$.)

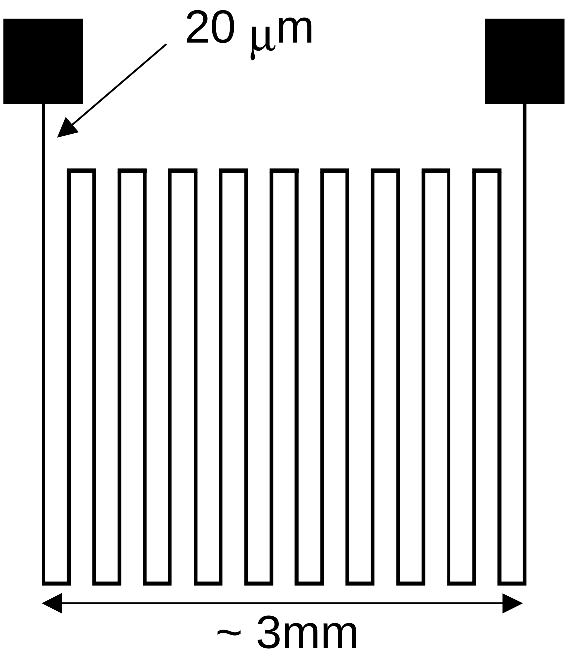

Fig. 4.1.1.2.1a. Single resistance line Cu meander line.

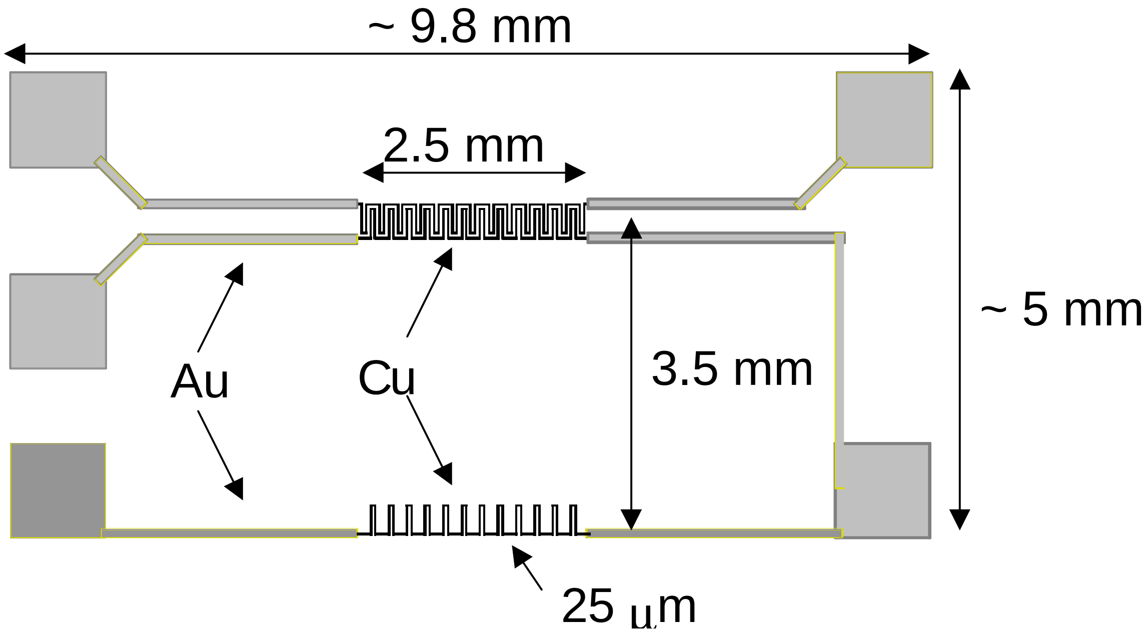

Fig. 4.1.1.2.1b. Triple resistance line Cu meander lines with Au contacts.

4.1.1.2. Fabrication of electrical test structures for quantifying sulfidation.

The simplest electrical resistance structure is a thin line of Cu patterned atop an SiO_2-coated Si wafer. In order to increase length, a meander pattern is used. Several electrical test structures have been used in this study as shown in Fig. 4.1.1.2.1. Fig. 4.1.1.2.1(a) is a single resistance line Cu meander line contact with two-point electrical connections. Fig. 4.1.1.2.1(b) is a triple resistance line Cu meander line contact with separate Au contacts. Fig. 4.1.1.2.1(c) is a high density single resistance line Cu meander line with separate Au leads for 4-point contacts.

The pattern shown in Fig. 4.1.1.2.1(a) was used for initial Cu resistance studies. The fabrication process of these structures consists of (1) blanket electron-beam evaporation of Cu directly on to ~ 0.5 μm thick SiO_2-coated Si(001) wafers, (2) photolithographic patterning of photoresist to leave a pattern of photoresist in the pattern shown in Fig. 4.1.1.2.1(a), (3) chemical etching of the Cu using a solution of H_3PO_4:CH_3COOH:HNO_3:H_2O (4:4:1:1) for about 50 sec., and (4) photoresist removal by immersion in acetone, followed by methanol, and drying in dry $CO_{2(g)}$ or $N_{2(g)}$. This etchant removes the Cu, leaving the photoresist intact. A disadvantage of this process is that there is some etching of the Cu beneath the photoresist at the edges of the Cu line. As a result, the resulting true linewidth of the Cu line is not precisely 20 μm (the target width), and there can be some variability of line widths from sample to sample. Other potential problems with this structure or fabrication process are that photoresist covers the Cu at one point in the processing and there could be a potential problem with residue left on the Cu surface following photoresist removal; also, the sidewall of the Cu lines are not completely vertical. There is a gradual slope in sidewall over one or more microns due to the chemical etching of the Cu. Lastly, the contacts for the meander pattern are also made out of Cu, and this can create uncertainty in the contact resistance during sulfidation. To make electrical contacts to the structure, Au wires were soldered to the Cu contact pads. The use of two wires per pad can

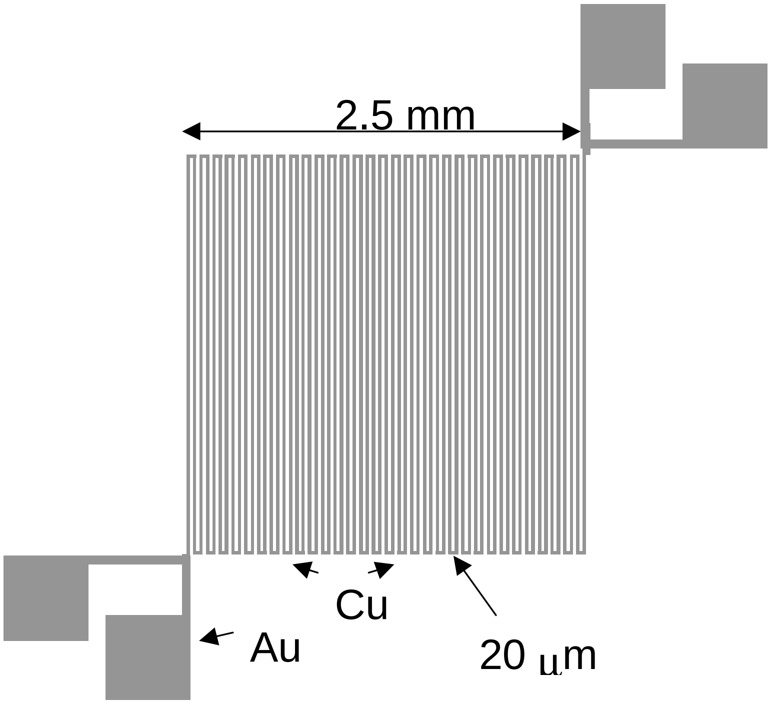

Fig. 4.1.1.2.1c. High density Cu meander line with Au contacts.

allow elimination of the lead resistance, but the contact resistance contribution is not eliminated. If there is no change in contact resistance with sulfidation, then the contact resistance will not play a role in the analysis of the electrical test structure as this series resistance contribution is subtracted (the measurement relies only on a change in resistance, not the magnitude of the resistance). In practice, these potential problems do not appear to be an issue for the measurement of the atmospheric sulfidation of Cu using this structure. As one demonstration, Fig. 4.1.1.2.2 shows the measured current-voltage characteristics for a Cu meander line prepared using this process prior to and following sulfidation (1 hour, 600 ppb H_2S, 80% RH).

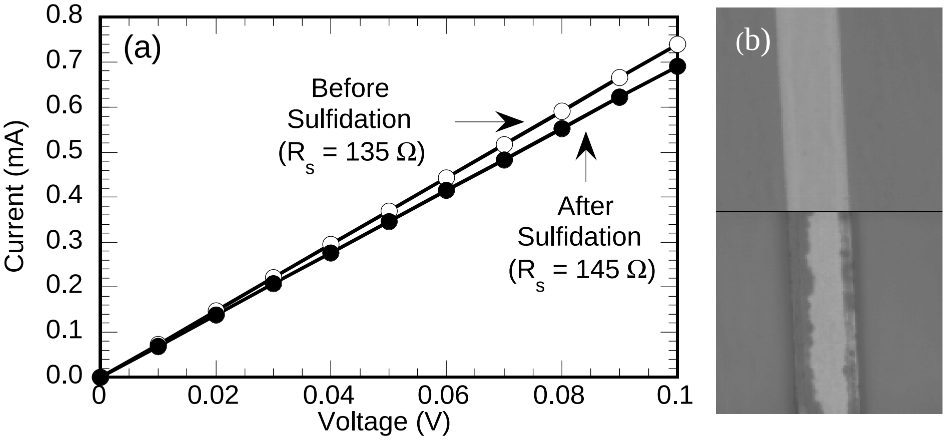

Fig. 4.1.1.2.2. (a) Current-voltage characteristics of a Cu meander line before and after sulfidation. The increase in resistance following sulfidation indicates a reduction in Cu^0. (b) Image of one of the Cu lines before (top panel) and after (bottom panel) sulfidation. The Cu line is ~ 16 μm in width.

In an effort to eliminate some of the potential problems with the structure of Fig. 4.1.1.2.1a, a new meander line test structure was developed (Fig. 4.1.1.2.1b). This structure contains three meander lines, two of which are interdigitated and the third separated from the other two. In addition, the meander lines have Au contacts to enable wire bonding to the structures. The intent of this structure is that the two interdigitated meander lines allow two experiments to be conducted under nominally identical conditions. The third line is used as an on-chip control. For example, the two interdigitated lines can be implanted with a species designed to affect the solid state diffusion rate of Cu, and the third line may be left unaltered in order to compare the effect of the implantation with the unaltered Cu.

In order to eliminate the problems associated with the chemical etching of Cu, the structure of Fig. 4.1.1.2.1b was fabricated using a Cu lift-off process. In this process, photoresist is patterned on to an SiO_2-coated Si wafer leaving photoresist everywhere on the sample, except in the region where the Cu meander line is supposed to be. Then Cu is uniformly deposited over the photoresist-patterned surface. Following Cu deposition, the sample is immersed in acetone to lift-off all of the Cu that lies atop the photoresist. After the Cu pattern has been formed, photoresist is again patterned on the surface to define the regions for the Au deposition. This requires one alignment step. Au is then deposited and then lifted-off in the photoresist-covered regions. This generates three Cu meander lines having Au contacts which can be electrically connected with Au wires using a wirebonder tool. The advantage of this process is that the linewidths of the Cu is precisely controlled and, therefore, the reproducibility from sample to sample is far greater. In practice, there are some unexpected difficulties with this processing. First, Cu adhesion to bare SiO_2 is poor, unless an adhesion promoter is used. It was found that about 20 nm of Ti is adequate for adhesion promotion. The second issue is that adhesion between the Cu and Au is surprisingly poor even when a Ti adhesion layer is used. This is true also for Cu films deposited atop the Au (i.e. reversing the deposition sequence to form the Au contacts first followed by the Cu meander line formation). At present, it is believed that this poor adhesion is due to photoresist or organic residue covering the metal surface (either Cu or Au, depending on the deposition sequence) that is not removed during the photoresist developer step. Intermittent success has been achieved by using an ozone clean following photoresist developing and prior to metal deposition.

The structure of Fig. 4.1.1.2.1c is also a Cu lift-off structure, but it is designed for a different purpose. The structure consists of a single large meander line with 20 μm linewidth and 20 μm spacing between lines. Again, the structure has Au contacts and there are two contacts per lead to eliminate the Au line and wire resistance (but not the contact resistance between Au and Cu). The purpose of this structure is to evaluate the lateral overgrowth of copper sulfide during sulfidation. The change in line resistance is again used to monitor the amount of sulfidation that has occurred, but simultaneous with this measurement, optical light scattering is also performed on this structure. Prior to sulfidation, the diffraction pattern reveals the a single periodicity of 20 μm associated with the width of the Cu lines and spacing between lines. During sulfidation, however, any lateral overgrowth of the sulfide leads to an apparent increase in width of the now-sulfidized Cu lines. Diffraction from this structure should clearly show this thickening, as the diffraction spots will split to show the two new periodicities: W_{line} and 40 μm – W_{line}, where W_{line} is the sulfidized line width. The processing of this structure is exactly like that of the structure shown in Fig. 4.1.1.2.1b, including the use of Ti adhesion layers for both the Cu adhesion to SiO_2 and the Au adhesion to SiO_2 and Cu.

4.1.1.3. The copper sulfide electrical conductivity test structure.

The electrical test structures discussed in section 4.1.1.2 are suitable for quantifying the degree of sulfidation of copper sulfide, but they are not suitable for determining the electrical conductivity of the sulfide. This is due to the fact that the sulfide and Cu resistances are in parallel, and the net resistance is dominated by the very low resistance of the Cu line. To accurately measure the sulfide electrical conductivity, a structure is needed in which the sulfide and Cu resistances are in series such that the total resistance is dominated by the much higher sulfide resistance. The necessary structure is one in which the conductivity of the sulfide is measured in the direction normal to the Cu film. This electrical test structure is shown in Fig. 4.1.1.3.1.

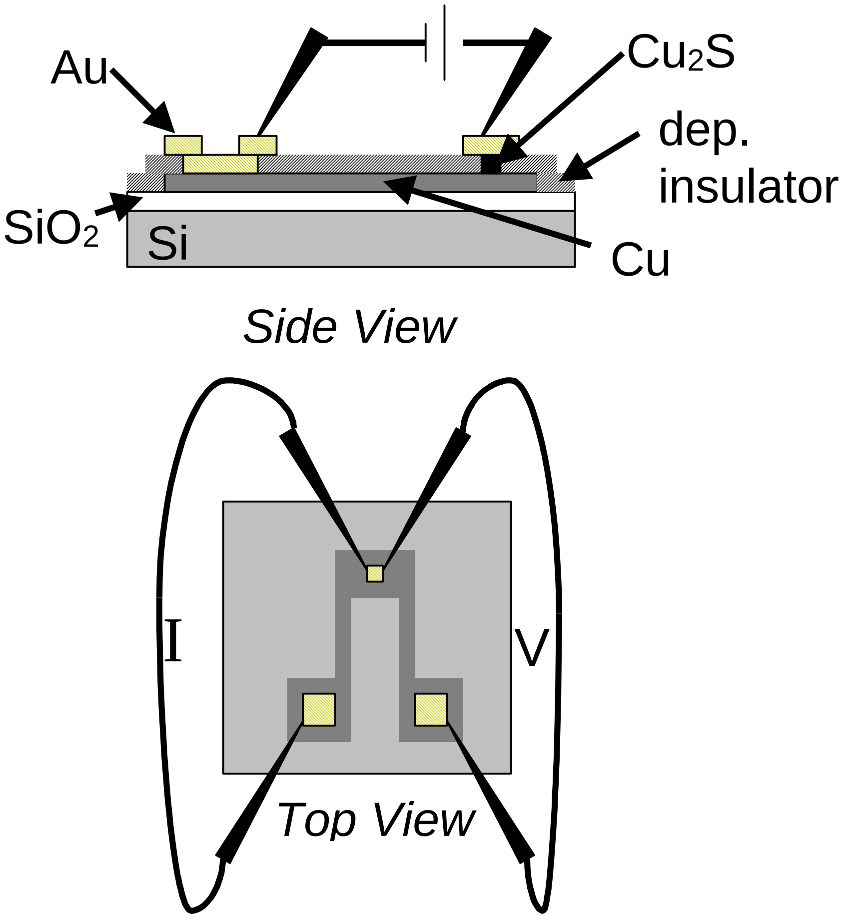

Fig. 4.1.1.3.1. The copper sulfide electrical conductivity test structure.

The structure shown in Fig. 4.1.1.3.1. is a three mask layer structure. The first layer of the structure is created through the use of photolithography and Cu lift-off to define the bottom metal layer and electrical contacts. This layer is on top of a layer of SiO_2 on a Si wafer. Following the creation of the bottom metal layer, an insulator is blanket deposited over the wafer. Due to variations in the coefficient of thermal expansion between Cu and SiO_2, it is preferred to use an insulating layer that is able to accommodate the thermally-induced stresses without cracking. Presently, parylene-N is the chosen insulating layer. This insulating layer is then patterned using the second mask level to define square openings or vias through the insulating layer to the bottom metal contact layer. In the case of parylene, dry etching using a photoresist mask in an Ar/O_2 plasma is the suggested method of etching. A range of openings was chosen, from 5 μm width up to 100 μm in width in order to confirm that the measured electrical conductance scales proportionately with the area of the opening. Following the creation of the openings in the insulating layer, the Cu bottom metal layer is sulfidized to a thickness less than half of the thickness of the original Cu film. Then the third mask level is used to pattern contacts over the sulfidized regions of the Cu film and a Au lift-off process is used. The resulting structure consists of a $Cu/Cu_2S/Au$ stack. Electrical contact is made to the bottom Cu layer and the top Au contact. As long as the copper sulfide is significantly more resistive than the Cu film and the contact resistance of the Au/Cu_2S interface, then the measured resistance of this structure can be used to quantify the resistivity of the Cu_2S layer. One caution with this structure that should be noted is that this structure is sensitive to voiding that occurs at the Cu/Cu_2S interface. Therefore, relatively thin Cu_2S layers should be measured where the voiding is not expected to be very severe.

4.1.2. In-situ Chemistry Sensors

We set out to establish methods for integrating potentiometric sensors into planar experimental platforms that could provide corrosion chemistry information. Method development included basic sensor design, demonstration of use, and experimental interrogation to yield useful and new chemical information relevant to atmospheric Cu sulfidation. We chose to address the detection of O_2 absorption into thin H_2O layers on a hydrated oxide surface.

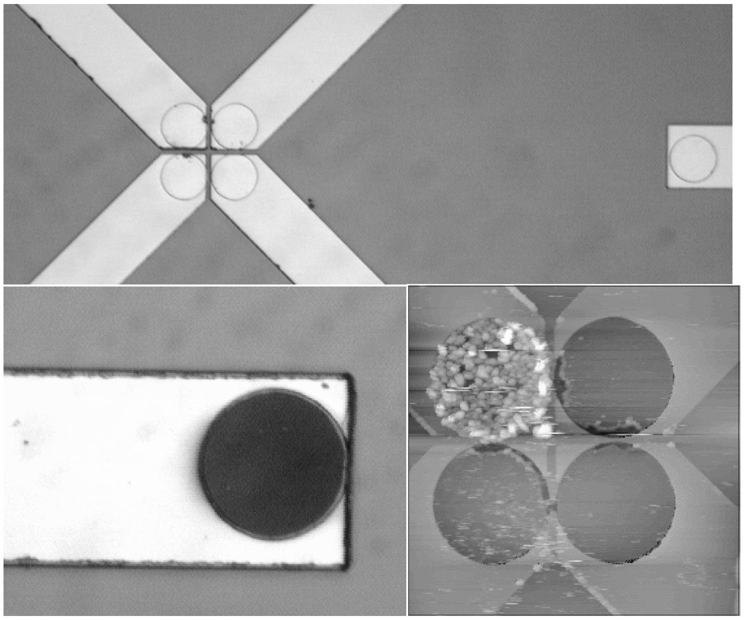

Fig. 4.1.2.1. Potentiometric sensor platform comprised of 5, 20 μm diameter Pt electrodes (a), a 20 μm diameter electrode after IrO_x electrodeposition (b), and atomic force microscopic image of a microcrystalline Ag deposit on a 20 μm diameter Pt electrode.

The intent was to detect O_2 in thin water films using cathodic reduction and pH detection. This indirect method of detection was chosen because direct amperometric or coulometric (current or charge measurement) requires the reduction of such excessive concentrations of O_2 at small length scales so as to significantly change the nature of an adsorbed H_2O layer. This approach is based on the fact that O_2 undergoes facile reduction at Pt and Au surfaces to form the hydroxide ion, as shown below:

$$O_2 + 2H_2O + 4\,e^- = 4\,OH^-$$

$$O_2 + H_2O + 2e^- = HO_2^- + OH^-$$

The ability to quantify O_2 is based on making a local pH measurement, appropriately accounting for diffusion (understanding the H_2O layer parameters), and distinguishing between two and four electron reduction mechanisms. In this report we demonstrate the ability to detect O_2. Accounting for diffusion requires either knowledge or control of the water layer geometry and we describe methods for attaining and confirming control. The issue of mechanism can be addressed experimentally by determining peroxide/hydroxide generation efficiencies in this specific system.

4.1.2.1 Approach

Detection of O_2 in an adsorbed H_2O layer depends primarily on local pH measurement. A suitable sensor platform was developed for conducting these experiments as shown in figure 4.1.2.1a and b. The sensor platform is based on a set of four closely spaced Au or Pt electrodes arranged on a square grid and separated by 2 μm. A fifth electrode is located 180 μm away from the center electrode cluster and serves as a counter electrode for potential control. These five electrodes are the ends of Au traces deposited onto SiO_2, covered with a silicon oxynitride film, and exposed through a patterned reactive ion etch. The inset trace surface is then filled with either additional Au or Pt through patterned physical vapor deposition or with a specific electrochemically active film through electrodeposition. Tailored design allows for the fabrication of a reasonably planar set of electrodes imbedded in a hydrophilic surface. Various electrode diameters were investigated from 20 to 1 μm, the latter being the size limit of conventional photolithography.

The concept of O_2 detection is also diagrammatically depicted in figure 4.1.2.1.1. A water film is allowed to form through adsorption from a high humidity N_2 gas stream. A central Pt electrode is polarized to a cathodic potential using an adjacent Ag/AgCl modified center electrode and the more distant counter electrode. A potential is selected to favor a full four electron transfer to OH^-. The third and fourth center electrodes are used to measure the resulting pH transient as OH^- is generated and then laterally diffuses away from the generation site. The potential difference between the pH sensing electrode and its reference electrode partner is made along an iso-potential dictated by the field between the generator and counter electrode. So, any potential change measured is independent of applied field.

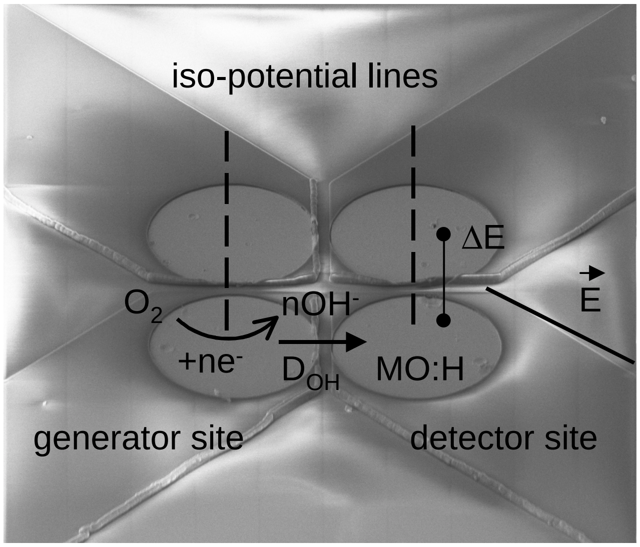

Fig. 4.1.2.1.1. Diagrammatic view of O_2 detection through pulsed reduction and local pH measurement: ne^- represents the number of electrons, D_{OH} is the diffusion coefficient, MO:H represents the pH sensing medium and E signifies direction of applied field.

A stable H^+ ion selective electrode that can be integrated into a microelectrode array is required for these types of measurements. This electrode should possess a stable absolute potential (potential at fixed pH of 0) and a stable, known pH sensitivity that are not susceptible to change with cyclic hydration and dehydration. IrO_x films were selected as the best candidate based on their known nearly-ideal Nernstian behavior and an ability to electrodeposit this material [20]. Experiments were conducted to determine the film response stability by using electrodeposits on wires, wire end cross-sections (50 to 100 μm diameter) encapsulated in epoxy, and on our sensor platforms. The most stable films resulted from cyclic electrodeposition from a basic iridium oxalate solution as described by Yaminaka [20] followed by a vacuum anneal at 100ºC for 1 hour. The results of periodic calibration of IrO_x/Pt electrodes using a standard H_3PO_4/NaOH titration are shown in figure 4.1.2.1.2. A pH sensitivity of 62 $mV{\cdot}pH^{-1}$ is obtained independent of Au or Pt as a substrate. The absolute potential for Pt is shifted by +60 mV with respect to Au, consistent with the higher mean work function for polycrystalline Pt that results in a larger contact potential difference between the IrO_x and substrate metal phases [21]. Also, the pH sensitivity does not change significantly with periodic drying of the film over a $CaSO_4$ desiccant for a 4 month period. Vacuum annealing of these films, presumably resulting in a porosity decrease, appears to be critical in providing this stability. The absolute potential does change with hydration/de-hydration cycles. However, this change may not represent a significant problem based the desire to conduct pH transient or relative measurements and an ability to re-calibrate the pH response.

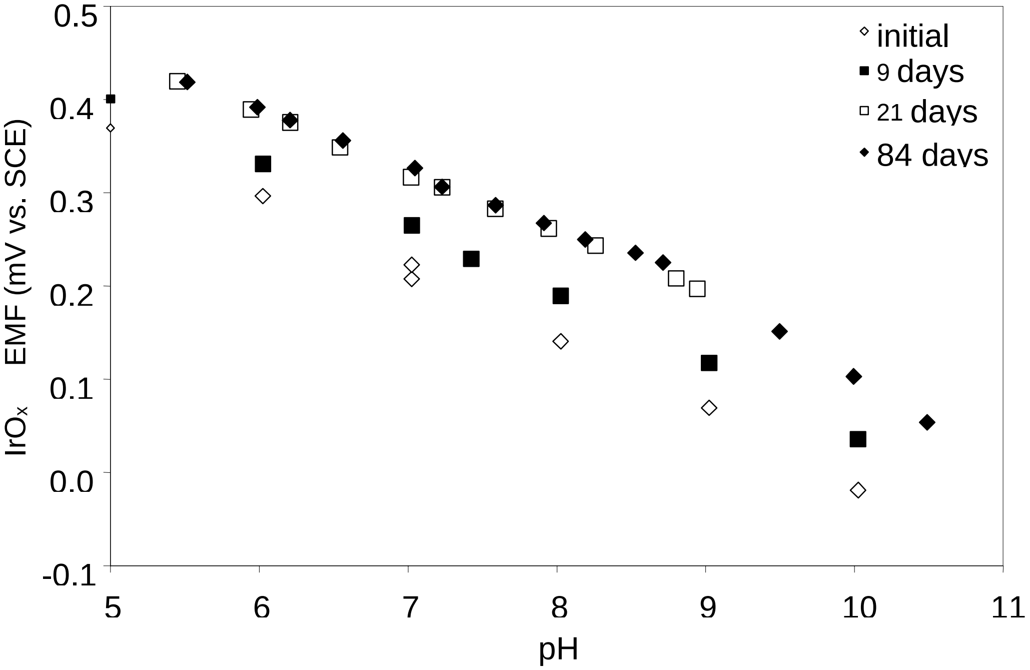

Fig. 4.1.2.1.2. Variation in the pH response of a IrO_x/Pt microelectrode as a function of time after deposition.

A suitable pH electrode must also respond rapidly to changes in pH. The response time of an electrode to a sudden change in pH can be measured and used to determine suitability. Alternately, the maximum deviation (or error) in the potential measured can be determined for a pH change over a given time period and can be related to a maximum error in pH. Figure 4.1.2.1.3 shows the maximum deviation for a set of electrodes measured over the first 100 seconds after removing from de-ionized H_2O and immersing the electrodes in known pH H_3PO_4/NaOH buffer solutions. Data for both dry films momentarily placed in de-ionized H_2O and fully hydrated films allowed to equilibrate in de-ionized H_2O for 12 hours are shown in this plot. The maximum deviation in potential is less than 2 mV indicating a maximum error of 0.03 pH units. Also, a nominally two-fold larger deviation is seen on subjecting the film to a basic pH change. The similarity in the responses of wet and dry films indicates that film hydration is quite fast making these thin IrO_x films good candidates for atmospheric corrosion studies.

The issue of water film continuity and hydrophilic control of the sensor surface was also addressed. A $SiON_x$ film was chosen specifically to ensure isolation of electrodes from one another electrically as well as isolation from the environment except for at the designated sensing or control region. Hydrophilicity was further ensured by periodic cleaning of the sensor in O_3 (UV generated). Little impact was found on the stability of either Ag reference or IrO_x pH films using this method. The fact that a continuous H_2O film can be formed on the sensor is shown in the impedance plot of figure 4.1.2.1.4. This data was generated by measuring the frequency-dependence of the impedance between the generator electrode and either an adjacent sensing or counter electrodes in dry and an 80% relative humidity flowing stream of N_2. The observed decrease in impedance modulus with increased humidity is due to ionic conduction in the adsorbed surface H_2O layer. Using the limiting low frequency impedance to estimate the water layer thickness, a value of approximately 200 nm was found assuming a CO_2-saturated H_2O conductivity of 5×10^{-7} S·cm^{-1} (measured in our lab), a 2 μm electrode spacing and a πr electrode perimeter interaction length (r = 20 μm). This value is surprisingly large and may reflect a lack of water layer geometry control (condensation at high aspect ratio features like the right angle at

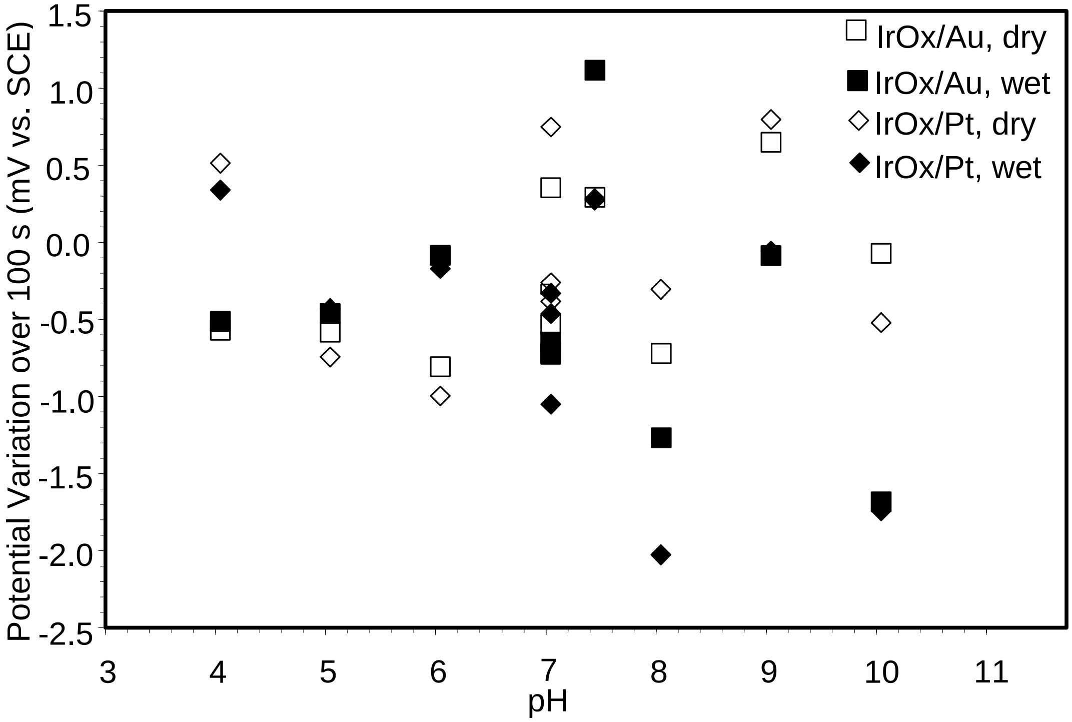

Fig. 4.1.2.1.3. Maximum deviation in potential measured for IrO_x electrodes equilibrated in CO_2-saturated de-ionized water (pH 6.2) or air-dried as a function of pH using H_3PO_4/NaOH buffer solutions.

the recessed microelectrode surface) increasing the cross-sectional area or H^+ dissociation from the $SiON_x$ surface yielding a conductivity increase. The similar response seen for the greater electrode spacing appears to be a result of a larger cross-sectional area resulting from pin-holes in the oxynitride distributed along the insulated electrical trace edges.

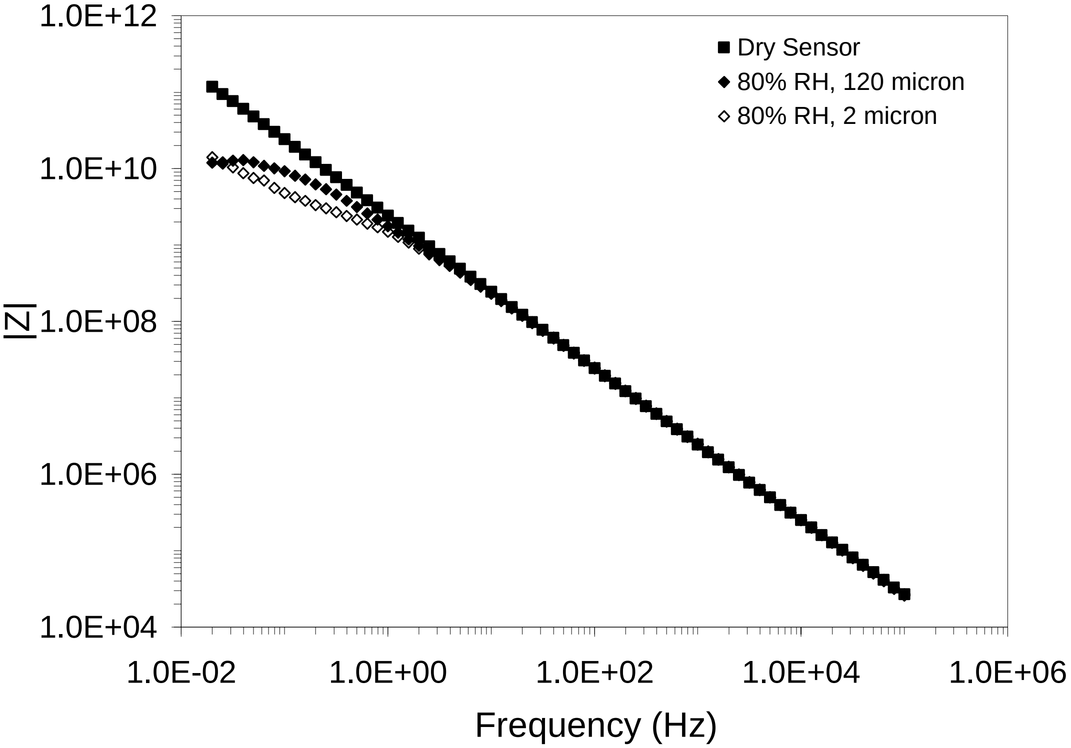

Figure 4.1.2.1.4. Impedance response between two 20 μm diameter Pt microelectrodes in a dry state and exposed to 80% relative humidity at spacings of 2 and 120 μm.

Water layer geometry could be controlled on a planar electrode array structure. Control could be exerted by generating hydrophilic paths between electrodes by locally modifying the surface of the insulator layer between the electrodes. Deposition of silane coupling agents, self assembled monolayers (SAMS), field perforation of a hydrophobic layer using a proximal tip are some examples of how local control of wetting could be established. Water layer geometry could be confirmed using electrostatic force microscopy [22] taking advantage of the ability of thin water layers to effective screen the image dipole in a metal surface and the higher dielectric constant of water in thicker films (beyond 3 - 5 monolayers) to dominate the force response relative to a low dielectric constant material like $SiON_x$.

Local, real time detection of O_2 has been accomplished using the microelectrode arrays. Figure 4.1.2.1.5 shows the resulting pH transients observed using fully oxygenated and N_2 de-aerated H_2O in a thin film produced by allowing a water droplet to spread across the array surface. Measurable differences in the magnitude of the potential transient was found to be indicative of increased net OH^- generation. A potential of –300 mV (1 second, versus PtO_x) was chosen based on cyclic voltammetric data that showed a maximum in cathodic current at this potential. Measurements of similar transients at lower potential indicated a limiting value in the maximum potential change indicating a reasonable maximum efficiency of O_2 reduction had been achieved. The pH pulse maxima occur at 5 seconds after the potential is pulsed (for 1 second) and the pulse half width occurs at 60 seconds. These time values are considerably greater than the 2 and 240 milliseconds required for the OH^- plume to first reach and then fully overlap the pH-sensing electrode (where $t = d^2/(2 \cdot D_{OH})$ and $D_{OH} = 10^{-5}$ $cm^2 \cdot s^{-1}$ for bulk H_2O). This discrepancy in time values reflects the response time of the IrO_x film, which is dominated by the kinetics of H^+ exchange. The pulse observed for the de-aerated case indicates that O_2 removal from the water was either not very efficient or enough time and a maximum surface-to-volume ratio of the resulting H_2O film where sufficient for partial re-equilibration.

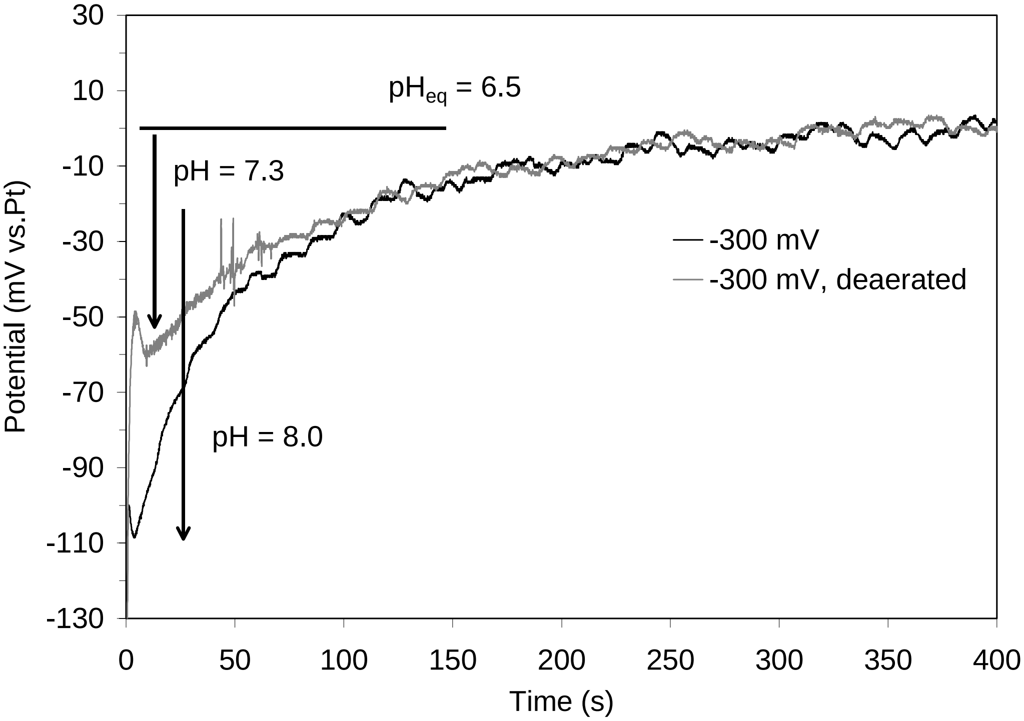

Figure 4.1.2.1.5. Potential response of a 20 μm diameter IrO_x/Pt to a 1 second –300 mV potential pulse at an adjacent 20 μm Pt electrode separated by 2 μm.

It appears that the transient pH measurements being made in this experiment are not fully accurate given the properties of bulk water. A pH change of 6.5 to 8.0 represents an OH^- concentration increase of 1.0×10^{-6} M ($[OH^-] = K_W / [H^+]$, $K_W = 10^{-14}$ M). An estimate of the expected pH change can be made by first calculating an expected O_2 concentration based on Henry's Law. At 630 torr (typical local atmospheric pressure), an O_2 saturation concentration in H_2O of 2.1×10^{-4} M should be established. In one second, a layer 45 μm thick should be depleted over the 20 μm diameter Pt cathode or a volume of 1.4×10^{-11} L. One hundred percent O_2 reduction efficiency in the electron transfer mechanism would yield a total of 3.0×10^{-15} moles of O_2 consumed and 1.2×10^{-7} moles of OH^- produced. Diffusion of this quantity of OH^- into a volume that fully overlaps the pH-sensing electrode (3.4×10^{-11} L) produces a transient $[OH^-]$ of 8.8×10^{-5} M. This value is 10^2 greater than the measured value and this difference may reflect a combination of the buffer capacity of CO_2 in H_2O and on the $SiON_x$ surface that surrounds the Pt electrode generator and detection sites. These results do demonstrate that pH transients can be measured and that they are expected to be quite large given the constrained distances and layer thicknesses (i.e. volumes) in question.

4.1.2.2. Accomplishments

A planar microelectrode sensor platform was designed and demonstrated for making corrosion chemistry measurements. Further, the use of a stable pH sensing film for atmospheric environments was developed and demonstrated. A qualitative detection scheme for O_2 partitioning into adsorbed, low dimensional H_2O films responsible for driving atmospheric corrosion was also demonstrated.

4.2 Controlled-Flow Reactor Design and Gas-Phase Mass Transport

4.2.1 Reactor Design, Experimental Configuration, Sample Preparation and General Data Analyses

As noted in section 3, Graedel and co-workers earlier proposed that Stage-I could be controlled by a surface reaction or by gas-phase mass transport. Possible control by a gas-phase transport process was supported in this study by two early observations documented in figures 4.2.1.1: (1) foil coupons that were sulfidized in a well-stirred jar chamber showed an

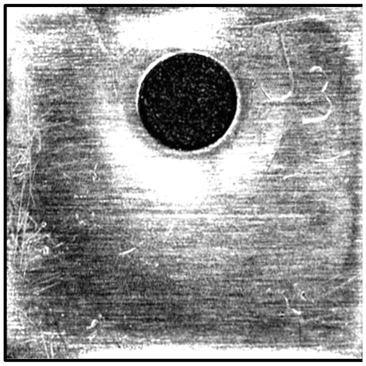

(a)

Fig. 4.2.1.1. Observations of microloading on Cu foils produced during sulfidation in a stirred jar suggested that gas-phase mass transport could control Stage-I sulfidation rate.

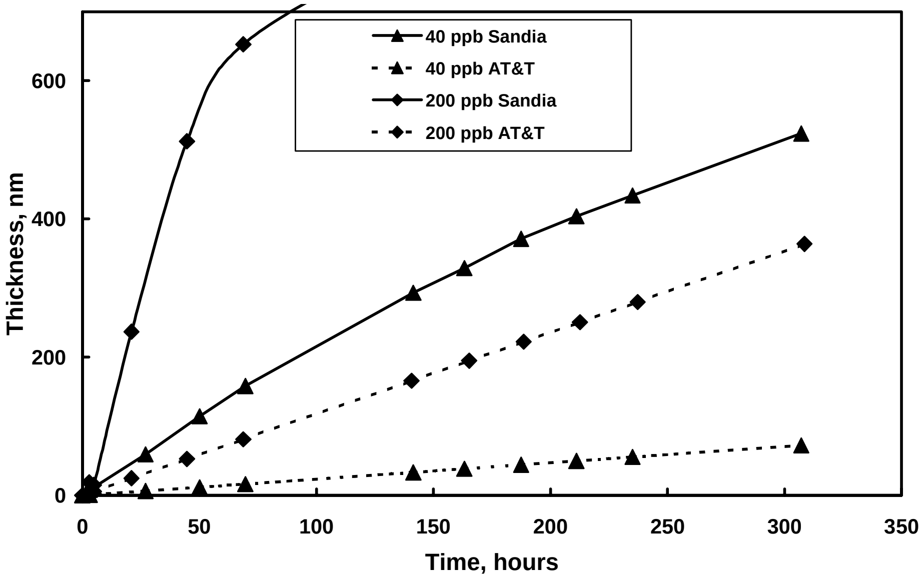

(b)

Fig. 4.2.1.1. Difference in film growth observed at Sandia and AT&T under similar conditions also suggest that gas-phase mass transport could control Stage-I sulfidation rate. (AT&T results calculated from model presented in reference [8]).

increased amount of copper-sulfide near the edges of the exposed faces (microloading), and (2) our sulfidation rates were an order of magnitude higher than those measured by Graedel under nominally similar conditions.

This evidence that the growth might be mass-transport limited under at least some conditions motivated an effort to design and use a reactor configuration that provides well-defined flow conditions that are uniform, easy to model, and that minimize the potential for gas-phase transport control. In this way, the mass-transport resistance effect can theoretically be understood and subtracted out to allow the more interesting interfacial reaction phenomena to be revealed. The reactor system shown schematically in figure 4.2.1.2 resulted. The dimensions associated with this design are all very critical. More information on the design of this reactor and a related analysis of its performance are given in Sections 4.2.2 and in Appendix A. A very important finding from the design analysis concerns the effective H_2S concentration in this reactor. With this configuration and flow conditions, one can legitimately treat the reactor as a continuous-stirred tank reactor (CSTR). That is, the exit H_2S concentration is more representative of the concentration to which the copper is exposed than that in the inlet. Finally, this reactor is sometimes referred to in this report as (1) a "stagnation-flow" or a "stagnation-point" reactor because a point exists on the exposed surface of the sample where the flow is actually stagnant, and also as (2) a "direct impingement" reactor because the flow is jetted directly onto the surface at relatively high rates.

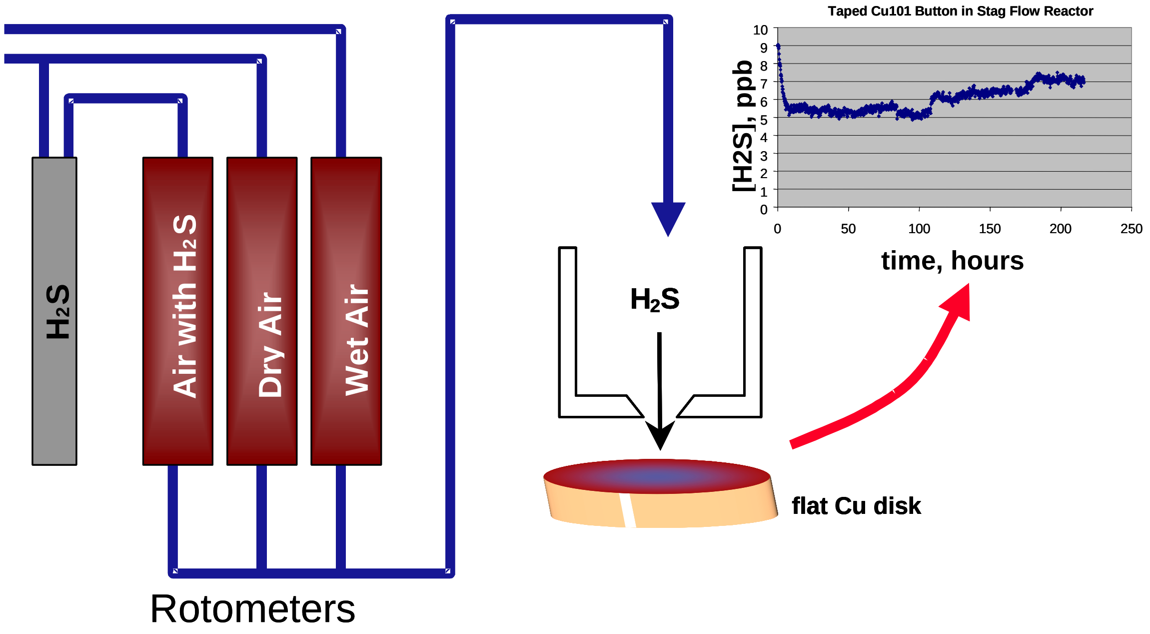

Fig. 4.2.1.2. Schematic diagram of gas exposure system, "stagnation" flow reactor (direct impingement), and typical outlet [H_2S] response.

Many of the experiments performed in this study used 16-mm diameter wrought Cu-101 disks sectioned from rod. Prior to exposure in the sulfidation reactor, one face of the disk was mechanically polished to a mirror finish and then pickled in a 10% HCl solution. The back and sides of the disk were masked with electroplater's tape to block any sulfidation. Several other experiments were performed on thin-film copper samples that were e-beam evaporated onto oxidized silicon surfaces. A comprehensive listing of all the sulfidation experiments that were performed is presented in Appendix B.

Importantly, many of the thickness values for the Cu_2S product layer that are presented in this report were calculated using a simple mass balance that was based on the consumption of H_2S as it flowed through the reactor. During these experiments, the inlet H_2S concentration was held constant and the outlet level continuously monitored. Using the flow rate, the mass loss was calculated and converted to an equivalent thickness of copper sulfide, assuming that the product layer was composed of Cu_2S, was uniform in thickness across the surface, and was fully dense. As will be discussed in Sections 4.5-4.6, ion-beam cross sectioning followed by examination with an electron microscope and Rutherford backscattering spectrometry (RBS) were used to confirm that these assumptions and this technique were indeed quite reasonable (error < 20%).

Finally, a note is needed about the relevance of the $[H_2S]$ levels that were used in this study (~ 5 to 300 ppb). In general, although these levels are quite small, they actually are much higher than concentrations experienced in typical indoor or even polluted outdoor environments where part-per-trillion or lower levels exist. As such, the experiments conducted in this study represent accelerated exposures. As an example, a commonly used accelerated aging environment for Au-plated copper is termed Class-II that consists of 30^oC, 70% RH, with 10 ppb H_2S, 200 ppb NO_2, and 10 ppb Cl_2. An exposure of 2 weeks in this environment simulates about 10 years of actual indoor industrial exposure (acceleration factor $\cong$ 250).

4.2.2 Analysis of Gas-Phase Mass Transport

An initial set of sulfidation experiments that was performed involved exposures at three different gas flow rates. The resulting outlet $[H_2S]$ is shown in figure 4.2.2.1a. The general shape of these concentration profiles is similar: the initial decrease in concentration that occurs over a finite time period coincides with the induction period previously described. The subsequent relatively flat response is indicative of a constant rate of H_2S consumption (Stage-I). Any increasing concentration after this is indicative of a slowing reaction rate and Stage-II. As noted in the previous subsection, these data form the basis for calculating the thickness of the growing Cu_2S product layer.

The results shown in the remaining portions of figure 4.2.2.1 quantitatively confirm that gas-phase mass transfer of H_2S does have at least some control over Stage-I kinetics. First, from figure 4.2.2.1b, the rate of sulfidation observed in the direct-impingement reactor is significantly greater than that which occurred in a "jar" reactor that was mildly stirred. In addition the residence time in the jar reactor is longer and the outlet concentration greater (experiments had similar exposed surface area and inlet concentration). However, the definitive evidence is the flow-rate dependence shown in figure 4.2.2.1c. Here, the higher the flow rate and therefore the lower the "mass-transfer boundary layer," the faster the reaction. Figure 4.2.2.1d is a plot of thickness vs. dose (outlet $[H_2S]$ times the time), results that demonstrate the flow-rate effect in (c) is not just simply due to a lower residence time / higher $[H_2S]$. In addition, to be shown in Section 5, is the observation that the rate of reaction is first order with respect to $[H_2S]$, a requirement for Fickian diffusion. Finally, confirmation of this conclusion is provided by the very sensitive, in-situ thin-film optical interference measurements described in Section 4.2.3 in which there were no measured Stage-I rate data that was independent of flow rate.

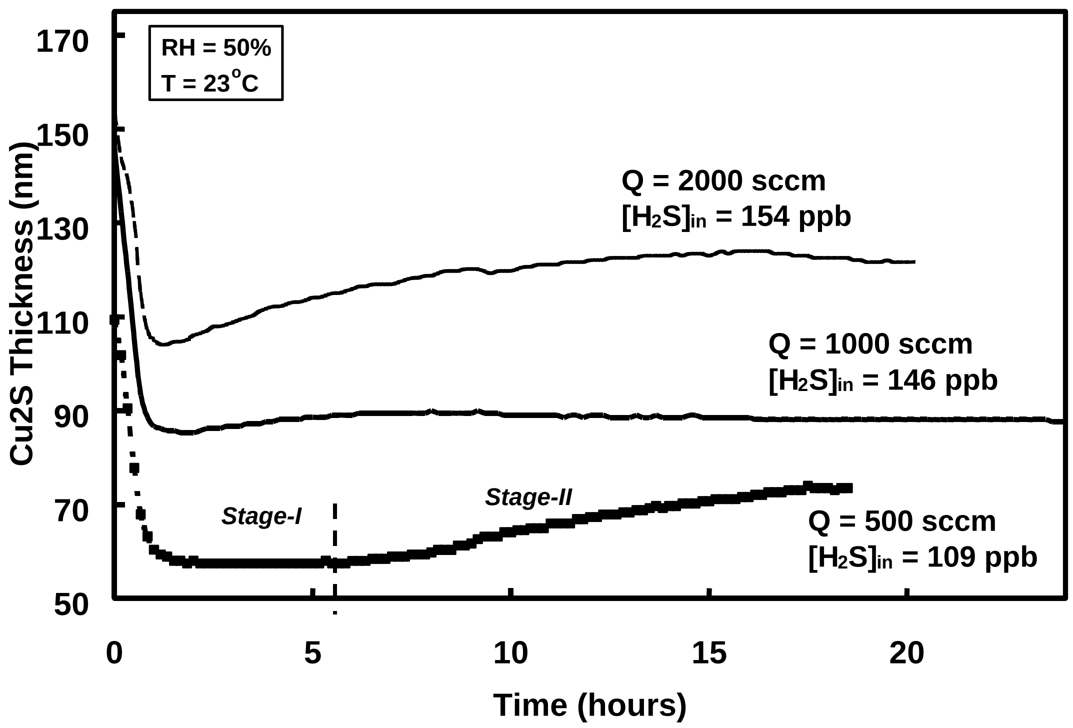
RH = 50%
T = 23°C
Q = 2000 sccm
[H2S]in = 154 ppb
Q = 1000 sccm
[H2S]in = 146 ppb
Q = 500 sccm
[H2S]in = 109 ppb
Stage-I
Stage-II
Cu2S Thickness (nm)
170
150
130
110
90
70
50
0
5
10
15
20
Time (hours)

(a)

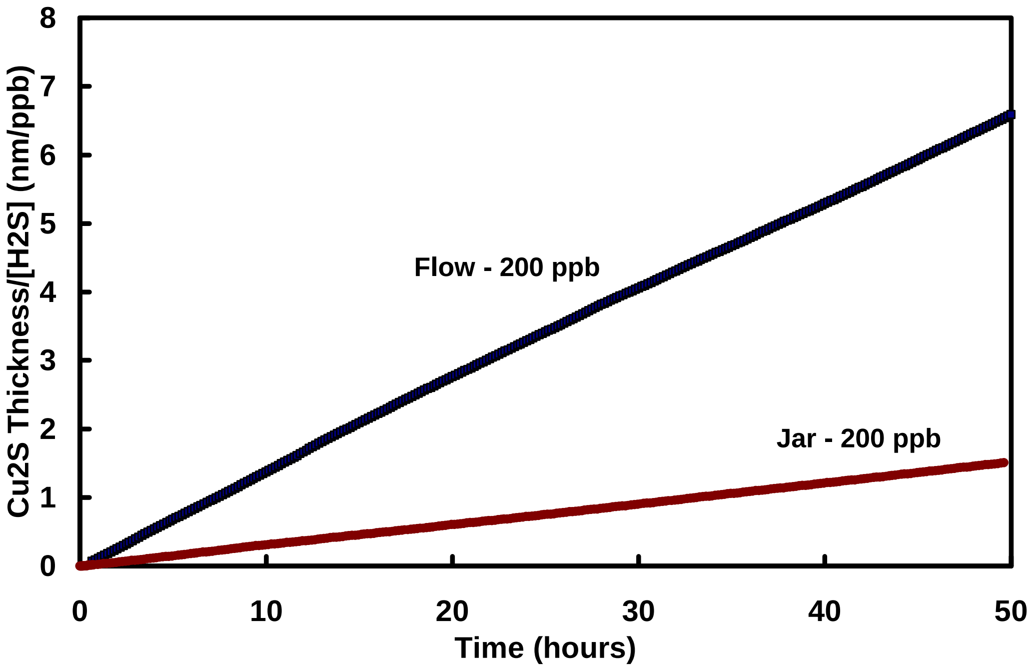
Flow - 200 ppb
Jar - 200 ppb
Cu2S Thickness/[H2S] (nm/ppb)
8
7
6
5
4
3
2
1
0
0
10
20
30
40
50
Time (hours)

(b)

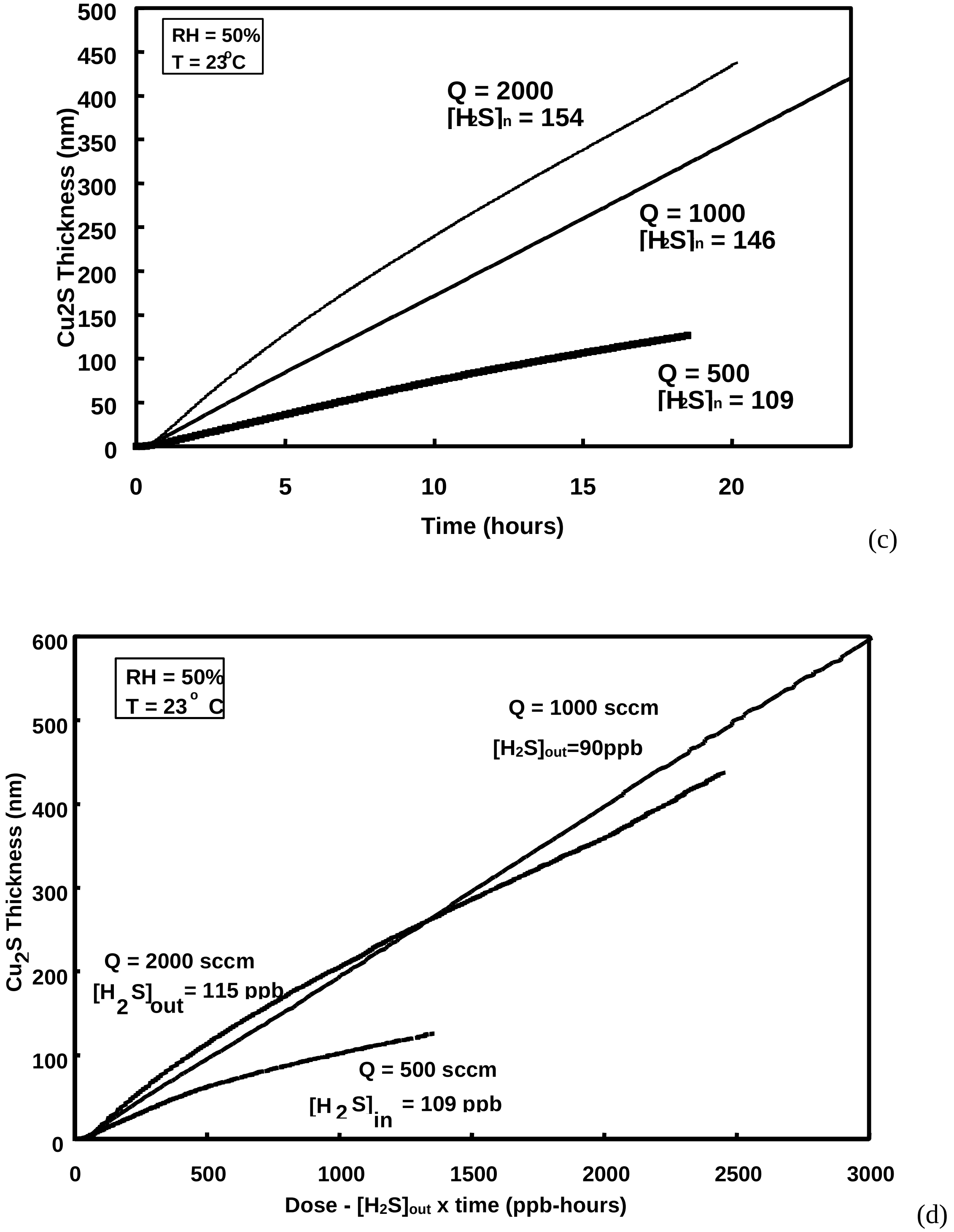

(c)

(d)

Fig. 4.2.2.1. Effect of gas-flow conditions on several sulfidation characteristics: (a) measured [H_2S] at impingement reactor outlet as a function of time for three flow rates, (b) calculated Cu_2S thickness produced in the direct impingement reactor vs. a stirred-jar reactor with the same inlet concentration, (c) Cu_2S thickness calculated from the concentration drop results shown in frame (a), and (d) thickness values in frame (c) plotted against total exposure dose.

Although there is this evidence that gas-phase mass transport has a significant role in controlling the sulfidation kinetics, this process does not totally control Stage-I kinetics. The primary support for this statement was shown previously in figure 3.4b where a positive correlation between relative humidity and Stage-I kinetics was noted. The presence of water in the atmosphere is not believed to have much influence on the diffusivity of H_2S in air. Therefore, some contribution of a surface reaction must be present. At higher RH levels, the corresponding thicker adsorbed water layers probably enable faster electrochemical oxidation and reduction to occur, thus allowing a higher degree of gas-phase mass transport control. Support for this mixed-kinetic control finding is also provided by a theoretical calculation of the fastest possible growth rate that would occur at the center of the sample. This calculation used a finite-element fluid mechanics model of the reactor configuration and the result was also shown in figure 3.4b. As can be seen, the measured rate is approaching pure gas-phase mass transport as the humidity increases.

4.2.3 In-situ Optical Measurements of Reactions

Even when the concentration of sulfur-containing gases is increased many-fold over that typically found in terrestrial atmospheric environments, the sulfidation rate of copper is very slow. It is thus difficult to measure sulfidation kinetics at its earliest stages with traditional methods. In this sub-section, a novel optical method for measuring copper sulfidation is described that is sensitive to as little as ten angstroms of Cu_2S on copper. The method was used to confirm that the earliest stages of copper sulfidation involves a surface chemical reaction with a very large rate constant. It was also confirmed that sulfidation is often preceded under some conditions by an “incubation period” before the first stages of sulfidation commences. A reactor cell with well-defined fluid mechanics is described that allows one to quantify the gas-phase concentrations and measured thin-film Cu_2S growth to address the measurement of the H_2S – Cu surface reaction rate constant. Evidence collected by this apparatus, combined with other experiments strongly indicate that any attack by atmospheric H_2S contaminants on copper will at first be transport-limited.

The results of these measurements have two implications. First, the very high Stage-I surface chemistry rate constant makes it extremely difficult to perform combinatorial chemistry measurements on macroscopic samples because it is difficult to ensure that all samples experience the same gas-phase environment. Second, one may calculate Stage-I sulfidation rates by assuming a zero surface-concentration of H_2S and using the diffusion-limited flux of H_2S to the surface to determine the growth of a Cu_2S corrosion layer.

4.2.3.1 Development of the Optical Technique

At the beginning of this project, we proposed to optically monitor copper meander patterns during sulfidation using the apparatus shown schematically in figure 4.2.3.1.1. The sample was patterned with a meander configuration that acts as a diffraction grating, scattering the laser light into many orders whose intensity pattern depends on the meander pattern line spacing, line width, thickness, and optical reflectance properties. Figure 4.2.3.1.2 shows diffraction intensity patterns expected from two meander patterns having the same 150-μm pitch, but two different line widths.

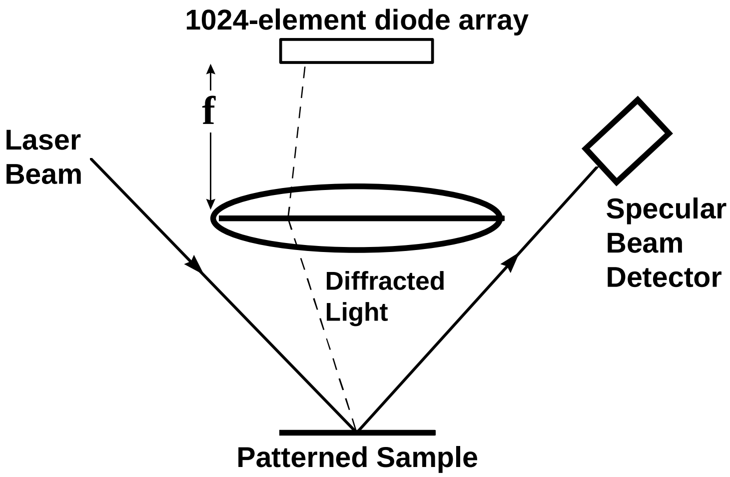

Fig. 4.2.3.1.1. Schematic diagram of the initial concept to optically measure the rate of copper sulfidation.

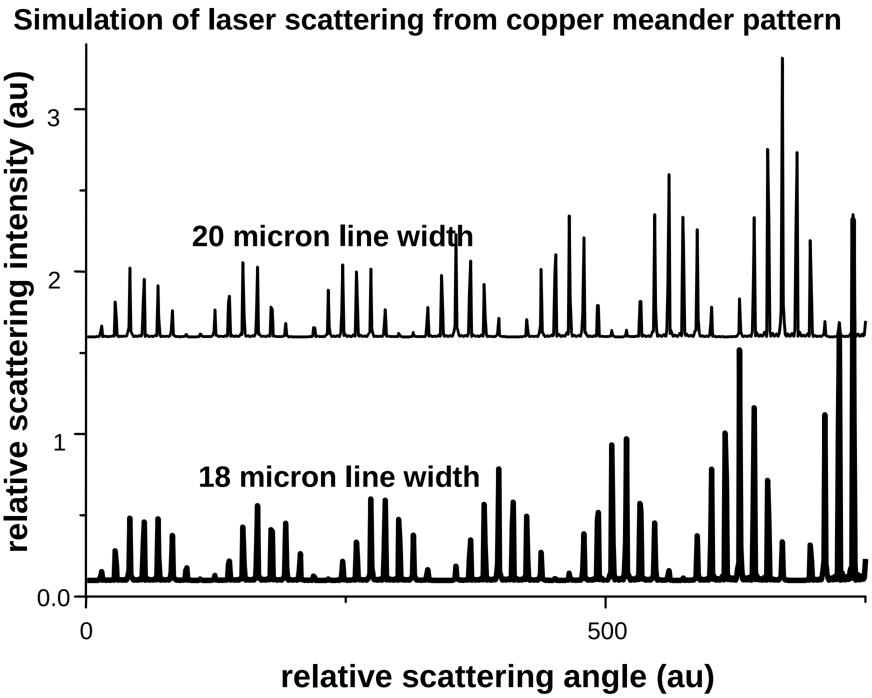

Fig. 4.2.3.1.2. Expected diffraction intensity patterns from two meander patterns with different line widths.

The 150-µm pitch gives rise to the closely-spaced sharp "spikes" in the diffraction pattern. The line widths of the copper features show up as modulations of the spike amplitudes. Notice that a ten-percent change in linewidth results in an easily seen shift in the modulation pattern. We planned to use quantitative fitting of the diffraction patterns to measure changes in linewidths of much less than one percent as the copper samples sufidized. The integrated diffraction pattern is proportional to $\exp[-(4\pi\sigma/\lambda)^2]$ where σ is the RMS height of the copper lines and λ is the wavelength of the laser. The light scattering is thus also sensitive to the vertical thickness of the copper films. The relative magnitudes of the modulation patterns contain information about the detailed shape of the copper line features. It was expected that we could extract a parameter from the diffraction pattern that measured the change in sharpness of the copper edges as sulfidation proceeded. This method would be amenable to a combinatorial array of meander patterns. Resistivity of the meander patterns would be simultaneously measured.

The apparatus was built, and several preliminary runs were made. During the course of these runs, strong thin-film interference oscillations were seen in the integrated diffraction pattern signal. It was clear that in the early stages of sulfidation, the Cu_2S overlayer was growing as a uniform thin film.

While these initial optical experiments were being performed, other sulfidation experiments were strongly suggesting that the Stage-I surface chemistry might be controlled by transport rather than by surface kinetics as was originally assumed (discussed previously). In addition to the copper foils immersed in a well-stirred reactor that exhibited more staining on the coupon edges, sulfidation on strips of copper placed in a channel flow showed that most of the sulfidation occurred at the front end of the channel. We therefore altered our optical measurement efforts to directly address the Stage-I sulfidation chemistry and to determine the surface sulfidation reaction rate constant.

4.2.3.2 Normal Incidence Reflectance Experiment

Given that Stage-I sulfidation produces semi-transparent thin films of Cu_2S, the growth rate of the thin film can be measured with a simple normal incidence reflectance apparatus shown in figure 4.2.3.2.1.

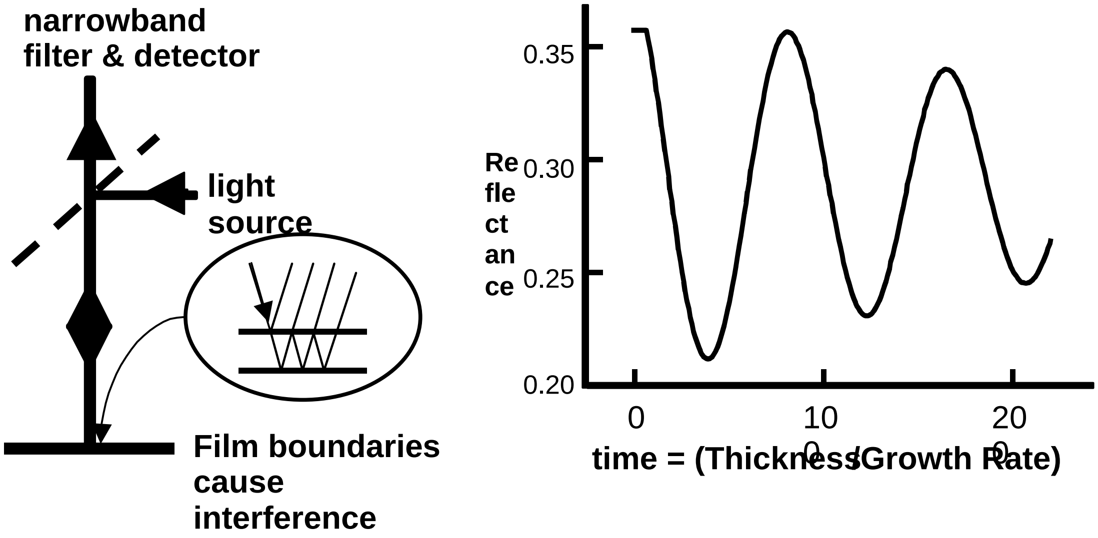

Fig. 4.2.3.2.1. Schematic diagram of the concept behind the optical measurement of copper sulfidation using normal incidence.

Light that reflects from the top and bottom interfaces of the Cu_2S film exhibits the interference effect in intensity shown in the graph on the right. When the round-trip distance through the thin film is a multiple of a half-wavelength, destructive interference is strongest and the reflectance signal goes through a minimum. For a multiple of one wavelength in the round-trip path, constructive interference is strongest and reflectance reaches a maximum. Absorption of light within the film causes the oscillations to decay as the film gets thicker.

Sandia has used this well-known thin-film interferometry method for many years in applications to compound semiconductor growth. A method called ADVISOR (for Analysis of Deposition using Virtual Interfaces and Spectroscopic Optical Reflectance) has been developed to extract growth rates and optical constants from growing thin films.[23] The method does not require any prior knowledge of the optical properties of the thin film, so it is well-suited to the potentially unknown sulfidation films that grow on copper. The ADVISOR analysis is performed on reflectance data using a computer application that automatically determines growth rate and optical constants over an arbitrary reflectance data segment.

4.2.3.2.1 Reflectance Waveform Behavior

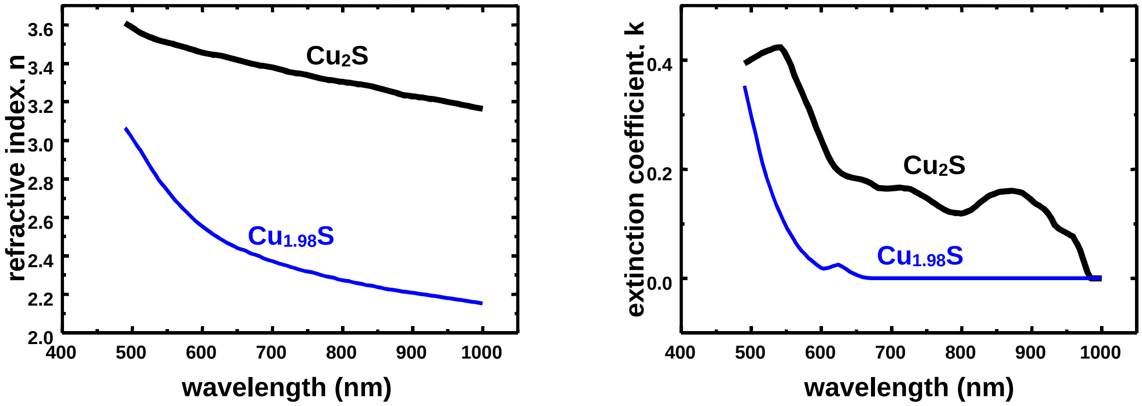

Figure 4.2.3.2.1.1. The complex reactive index for chalcocite (Cu_2S) and digenite ($Cu_{1.98}S$).

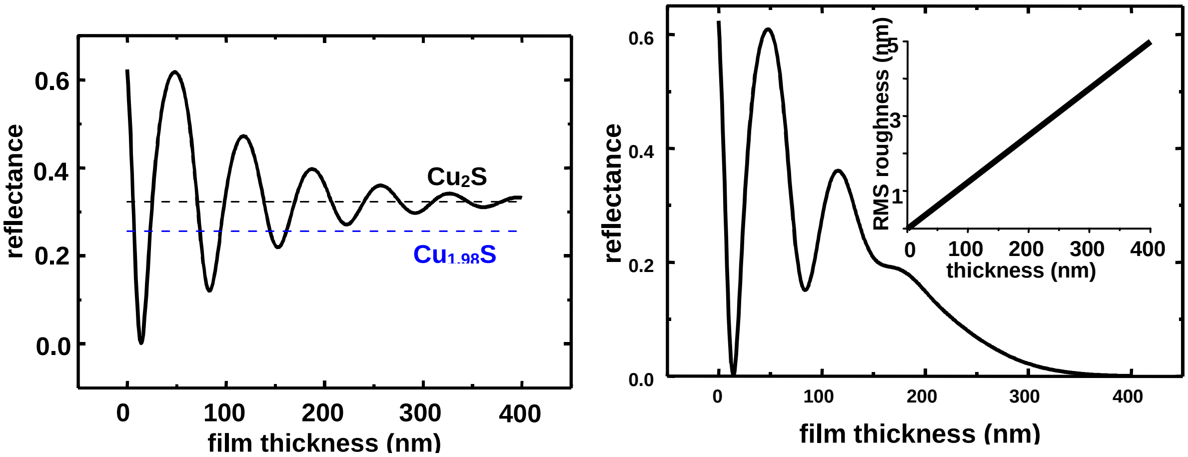

Fig. 4.2.3.2.1.2. Expected waveforms for a smooth copper sulfide film (left) and one whose roughness is linearly proportional to thickness (right).

This section describes the expected behavior of reflectance interferograms for copper sulfide films. The effects of the refractive index and film roughness are illustrated. Because the

ADVISOR method can extract optical constants as well as growth rates from reflectance data, it should serve as a chemical analysis tool to indicate the composition of the copper sulfide film. The plots contained in figure 4.2.3.2.1.1 show the real and imaginary parts of the complex refractive index for the two common forms of copper sulfide that are relevant to this study: Cu_2S and $Cu_{1.98}S$. As can be seen, despite the very small difference in copper content, there are substantial differences in the refractive index values. The responses shown in figure 4.2.3.2.1.2 are the expected waveforms for a smooth Cu_2S film and a Cu_2S film whose roughness is linearly proportional to its thickness. Stage-II growth develops rough films, so the reflectance is expected to vanish for thick sulfide films.

4.2.3.3 ADVISOR Results

Figure 4.2.3.3.1 shows the graphical results from ADVISOR on a sulfidized copper button. The refractive index is consistent with literature values for Cu_2S. The left graph shows the entire reflectance profile. It is characterized by an incubation time in which the growth rate is slow, interference fringes characteristic of smooth, thin-film growth, and a decrease in reflectance intensity characteristic of thin film roughening. The graph on the right shows the ADVISOR fit for growth rate. These fits are not exact. After examining many runs, it appears that the growth rate is not constant for very long segments of time. Figure 4.2.3.3.2. shows the obvious effects of a changing growth rate as the film becomes thicker. The curve on the right shows a fit to the reflectance waveform that is good up to about 4200 seconds. After this time, the measured interference oscillations slow considerably and are not consistent with the initially high growth rate of the film. Finally, figure 4.2.3.3.3 is another example of non-uniform growth rate. In this sample, essentially no sulfidation occurred for the first 5000 seconds of exposure, dramatically illustrating the initiation (incubation) time that was indicated by other measurement techniques. Because the reflectance technique is sensitive to thin-film thicknesses as small as 10 Å, it can be used to obtain a very accurate measure of this sulfidation incubation time.

4.2.3.3.1 Comparison with Mass Balance Measurements

ADVISOR analysis was performed on samples that were also simultaneously monitored by H_2S concentration measurements (technique described in Section 4.2.1-4.2.2). Experiments were made in both low humidity and high humidity air environments. The tables that follow compare the results obtained with ADVISOR and the mass-balance calculations. The growth rate values marked with an asterisk in these tables involve data in which it was clear that the growth rate was not constant. Direct comparisons between the optical and H_2S measurement method thus are not appropriate. In general, the agreement is good. The optical method is superior for measuring accurate incubation times and fast initial growth rates. The H_2S method is superior for monitoring the overall consumption of sulfur over long times even when the surface has become rough.

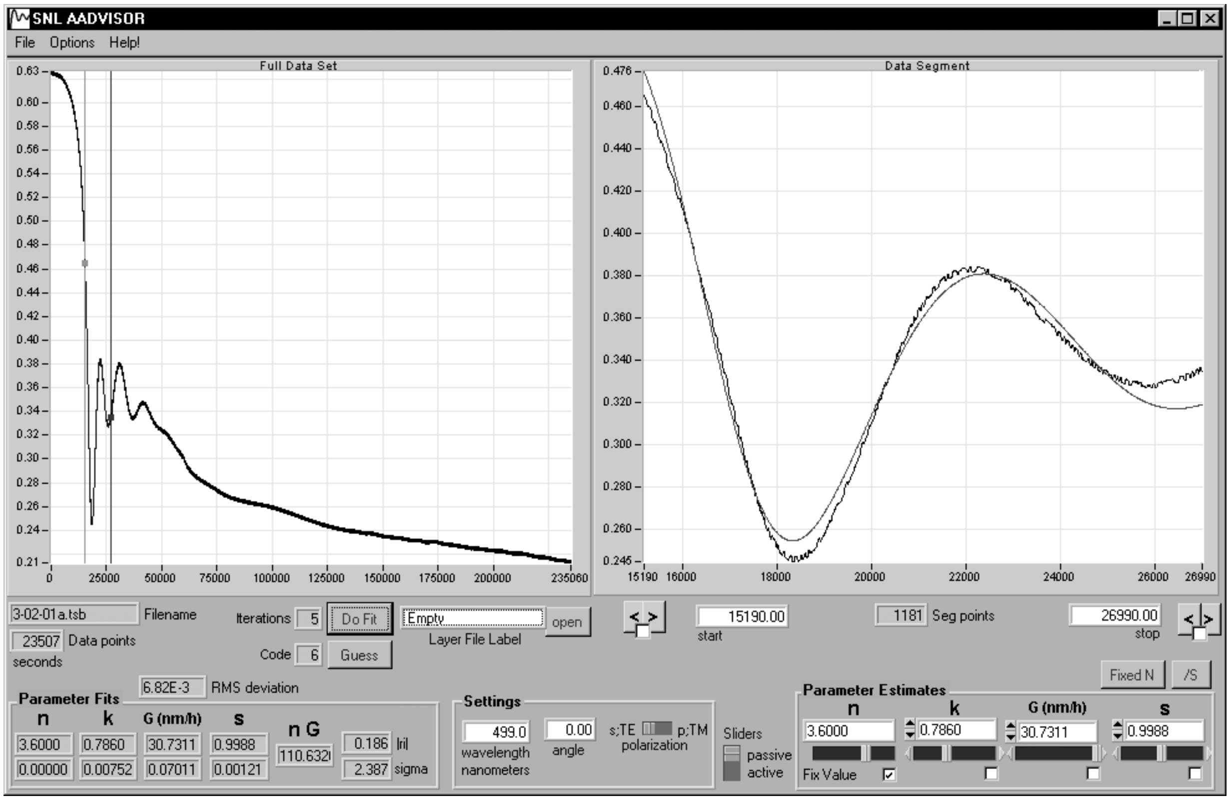

Filename: 3-02-01a.tsb
23507 Data points
seconds
Iterations: 5
Code: 6
Layer File Label: Empty
start: 15190.00
1181 Seg points
stop: 26990.00
RMS deviation: 6.82E-3

Parameter Fits

n	k	G (nm/h)	s	n G	
3.6000	0.7860	30.7311	0.9988	110.632	0.186 |ri|
0.00000	0.00752	0.07011	0.00121		2.387 sigma

Settings

wavelength nanometers: 499.0
angle: 0.00
polarization: s;TE p;TM

Parameter Estimates

	n	k	G (nm/h)	s
	3.6000	0.7860	30.7311	0.9988
Fix Value	☑	☐	☐	☐

Fig. 4.2.3.3.1. Typical results obtained by ADVISOR during copper sulfidation.

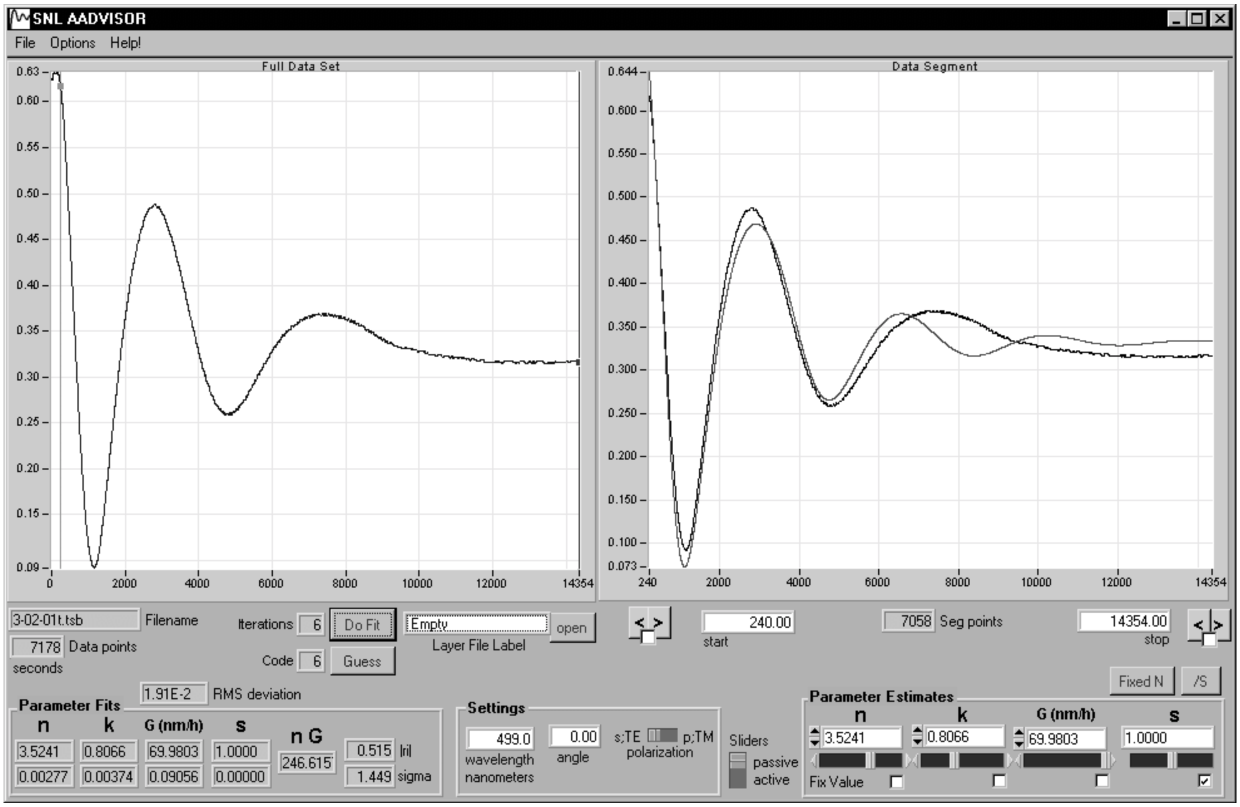

Filename: 3-02-01t.tsb
7178 Data points
seconds
Iterations: 6
Code: 6
Layer File Label: Empty
start: 240.00
7058 Seg points
stop: 14354.00
RMS deviation: 1.91E-2

Parameter Fits

n	k	G (nm/h)	s	n G	
3.5241	0.8066	69.9803	1.0000	246.615	0.515 |ri|
0.00277	0.00374	0.09056	0.00000		1.449 sigma

Settings

wavelength nanometers: 499.0
angle: 0.00
polarization: s;TE p;TM

Parameter Estimates

	n	k	G (nm/h)	s
	3.5241	0.8066	69.9803	1.0000
Fix Value	☐	☐	☐	☑

Fig. 4.2.3.3.2. Results from ADVISOR produced when the sulfidation rate is changing.

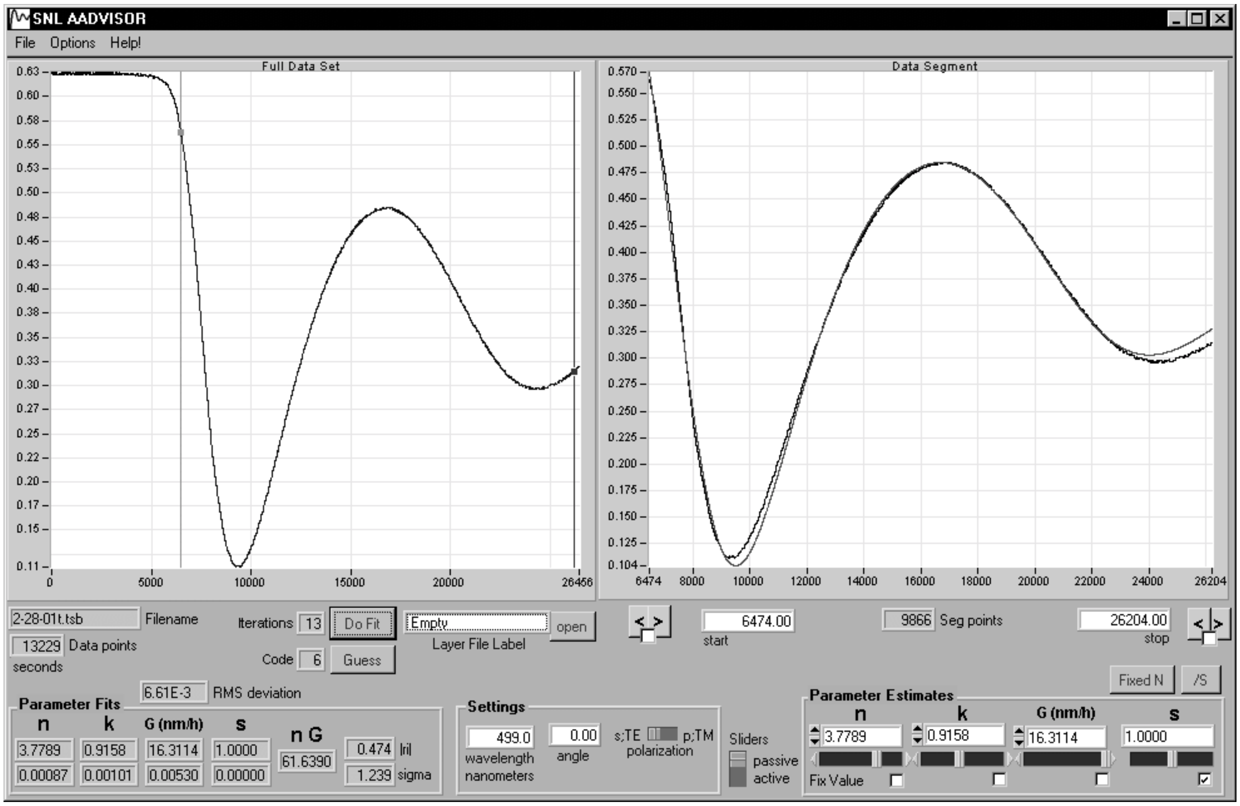

Filename: 2-28-01t.tsb

Data points: 13229

seconds

Iterations: 13

Code: 6

Layer File Label: Empty

start: 6474.00

Seg points: 9866

stop: 26204.00

RMS deviation: 6.61E-3

Parameter Fits

n	k	G (nm/h)	s
3.7789	0.9158	16.3114	1.0000
0.00087	0.00101	0.00530	0.00000

n G: 61.6390

|ri|: 0.474

sigma: 1.239

Settings

wavelength nanometers: 499.0

angle: 0.00

polarization: s;TE p;TM

Parameter Estimates

	n	k	G (nm/h)	s
	3.7789	0.9158	16.3114	1.0000
Fix Value	☐	☐	☐	☑

Fig. 4.2.3.3.3. Results from ADVISOR under conditions when a significant induction time exists.

0% Humidity:

Run ID	incubation, optical (h)	incubation, H_2S (h)	growth rate, optical (nm/h)	growth rate, H_2S (nm/h)
5C 3-08-01t	3.95	--	--	--
15C 2-28-01t	1.17	1.32	16.3	16.9
25C 3-07-01t	0.58	0.93	28.4	26.1
35C 3-06-01t	0.42	0.50	38.8	26.7

80% Humidity:

Run ID	incubation, optical (h)	incubation, H_2S (h)	growth rate, optical (nm/h)	growth rate, H_2S (nm/h)
15C 2-27-01t	0.14	0.13	23.1	28.9
15C 3-01-01t	0.20	0.22	35.7	21.7
25C 3-02-01t	0.05	0	70.0 *	23.5
35C 3-05-01t	0.02	0	69.7 *	19.0 *

4.2.3.3.2 Very Thin Film Measurements

It is important to examine the structure of the Cu_2S film in its very early stages of growth. However, it is difficult to grow such films. Processes that are still not well-understood lead to variable incubation times. This eliminates a simple timed-recipe approach to growing such films. The optical probe is ideal for growing these films because one can associate a change in reflectance with a film thickness. The graph in figure 4.2.3.3.2.1 illustrates this relationship:

4.2.3.4 The Stagnation Flow Reactor

Early measurements of copper sulfidation using the reflectance optical probe gave mixed results. At first, the copper samples were placed inside a small plexiglass enclosure with a volume of approximately 25 cm^3. Sulfidation of these samples occurred preferentially at the edges, again indicating a transport-limited signature. A new cell was constructed that was designed to flow the H_2S-containing air in a narrow channel over the copper. A 1 × 3 mm cross-sectional channel was made with the idea that the optical probe could measure sulfidation as a function of distance downstream. From these data, a surface reaction rate constant could be extracted. The results of the experiment were disappointing. Most of the sulfidation occurred in the first few millimeters of the channel, indicating a very high rate constant that depleted the system of H_2S as the gas passed downstream. Even flowrates of 1 l/m producing an average flow velocity in the channel of 500 cm/s, were not sufficient to spread the sulfidation reaction over more than a few millimeters.

Because the channel reactor was inadequate, it was decided to build the stagnation-flow reactor previously described in Section 4.2.1. This reactor would presumably grow a uniform film in the center and the kinetics could also be easily modeled. Figure 4.2.3.4.1 is a schematic of the stagnation reactor. Gas entering the chamber is

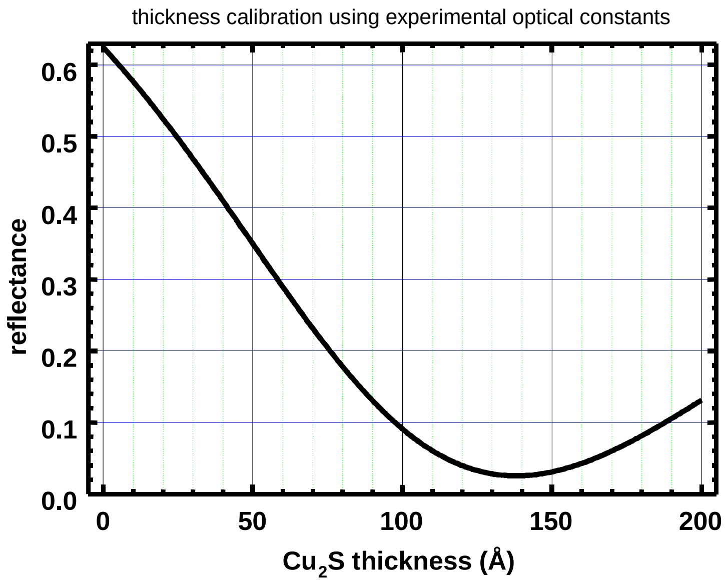

Fig. 4.2.3.3.2.1 Effect of sulfide-layer thickness on the total reflectance, indicating the ability to resolve very thin layers.

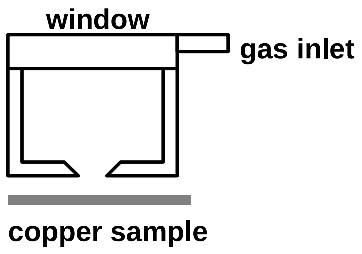

Fig. 4.2.3.4.1. Another schematic diagram of the stagnation-flow reactor, highlighting the optical window.

forced out the small (3 mm) aperture that is placed close to the copper sample. Uniform chemical reaction is expected over roughly the diameter of the aperture. The window on the cell allows one to perform normal-incidence reflectance measurements during sulfidation.

Predicted flow characteristics are shown in figure 4.2.3.4.2. A donut deposition pattern can be produced that is caused by the high-velocity stream of gas that passes the knife edge and impinges on the substrate. This thins the boundary layer and allows the highest deposition at radial points below the knife edge.

Finally, figure 4.2.3.4.3 is a graph of the expected Cu_2S growth rate as a function of radial position from the center of the stagnation aperture for a series of aperture-substrate separation values. The original spacing was 0.8 mm. The model predicts the observed donut pattern. The thickness profile can be flattened considerably simply by pulling the sample further away from the aperture. The experiments reported in this document were made with a 5 mm aperture-substrate spacing.

Fig. 4.2.3.4.2. Flow velocity fields (left) and sulfide concentration fields (right) predicted for the stagnation flow reactor with dark indicating maximum, light indicating minimum..

4.2.3.5 The Copper Sulfidation Rate Constant

ADVISOR optical analysis of growing Cu_2S films confirmed suspicions that the rate constant for sulfidation must be very fast. Measurements in the stagnation flow reactor resulted in growth rates that depended on gas flow rate, up to the highest practical flow rates that could be used. If the surface chemistry is slow compared to transport limitations, the sulfidation rate becomes independent of gas flow past the copper sample. Given that this was not the case in the samples measured with the optical probe, one may conclude only that there is a very high reactive sticking probability for H_2S on copper. The highest growth rate measured, 70 nm/s, implies that the rate constant can be no slower than 19 cm/s, corresponding to a reactive sticking coefficient of 5×10^{-4}. This high rate constant has important consequences for combinatorial experiments that attempt to dose an array of differently-treated samples with the same flow of air containing H_2S. Flow directed across the array will inevitably be depleted by samples at the leading edge, and samples may encounter non-uniform sulfidation from local concentration gradients that depend on detailed flow patterns.

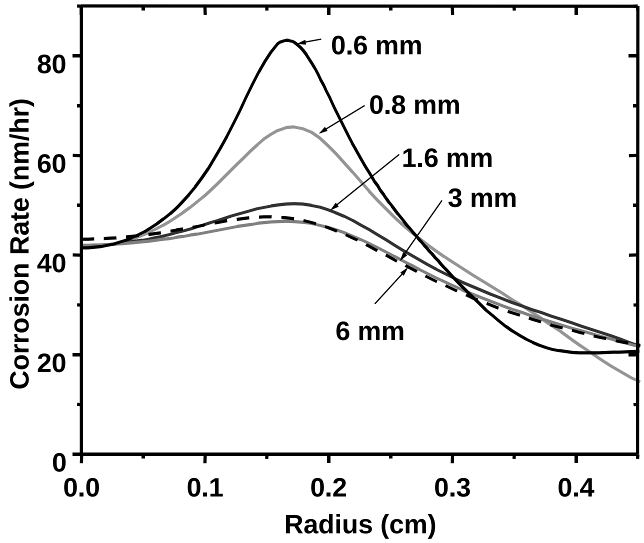

Fig. 4.2.3.4.3. Predicted copper sulfide growth rate as a function of position.

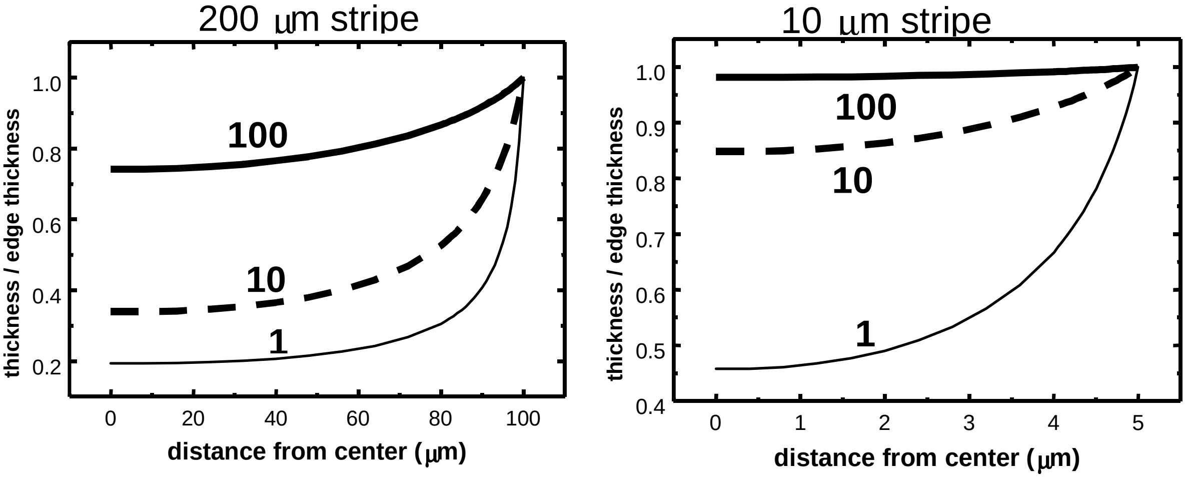

Fig. 4.2.3.5.1.1. Relative copper sulfide thickness profiles expected from the sulfidation of a thin copper stripe.

4.2.3.5.1 Micro-loading Experiment

An experiment to measure the sulfidation rate constant was devised by taking advantage of the local micro-loading effects alluded to above. A metric of the extent that H_2S could diffuse before it reacts is given by the ratio of the diffusion coefficient, D, to the surface reaction rate constant, k. For the smallest possible rate constant, 19 cm/s, a ratio $D/k = 88\,\mu\text{m}$ is obtained for the conditions of our corrosion measurements. To verify the value of *k*, one needs to sulfidize copper features that are compatible with the size of the *D/k* ratio. The predicted relative Cu_2S thickness profiles from sulfidizing a long, thin copper stripe are shown in figure 4.2.3.5.1.1. Each curve is labeled with its *D/k* ratio. These profiles were predicted from a two-dimensional model of the gas phase diffusion and chemical reaction. By choosing different stripe widths, the model predicts that the *D/k* ratio may be extracted from a measurement of the Cu_2S thickness across the copper stripe. The confirmatory experiments have yet to be performed.

4.3 Adsorbed Water-Layer Distribution

The morphology (thickness and spatial distribution) of the adsorbed water layer on the oxide surface will probably have a profound effect on the chemistry and transport of reactants and the subsequent precipitation and growth of the Cu_2S sulfidation product layer. At moderate to high relative humidity levels (> 50-70%), the water layer should be continuous, with a thickness of several monolayers. At the lower RH levels encountered in typical atmospheric corrosion environments, we expect isolated droplets or puddles, where the aerial coverage and droplet size will be a sensitive function of both RH and the heterogeneous nature of the oxide surface. An accurate understanding of the reactions taking place at the gas/liquid/oxide interfaces will require knowledge of the spatial distribution of these heterogeneities. We have attempted to quantify these heterogeneities using two approaches that take advantage of local chemical reactions: the first being dependent on the presence of water droplets and the second on the local hydration of the oxide.

It is well known that Cu-acetate crystals are readily grown by exposing Cu to acetic acid. Local droplets of acetic acid were formed on the copper surface by first subjecting samples to a controlled RH exposure and then allowing the resulting water droplets to react with acetone vapor in the presence of ambient light.[24] The underlying Cu was expected to react and form local crystals of Cu acetate. We found that crystal formation did not occur unless the native Cu oxide layer at the surface was first removed by abrasion. In this case, local Cu acetate crystals were observed along certain abrasion lines, with a random density in different regions of the sample. It is likely that the crystals grew as a result of successful oxide removal, rather than due to the presence of water droplets alone. We also attempted to remove the surface oxide with a dilute HCl etch and repeated the water and acetone exposure. Cu acetate crystals did not grow under these conditions, likely due to the re-oxidation of the Cu surface as a result of exposure to water during the etch rinse.

We expect that the water droplets will interact with the oxide surface to form hydrated Cu oxide. Our approach to observe the heterogeneous nature of the hydroxide formation is to use the difference in affinity of dyes for hydrous and anhydrous oxide surfaces.[25] The mechanism of dye adsorption (from nonaqueous solvents) appears to be through hydrogen bonding. This technique has been used successfully on Al oxides to observe heterogeneities by optical microscopy down to micron length scales. We investigated the possibility of preferential adsorption of fluoroscein and rhodamine B dyes on hydrated Cu oxide surfaces relative to non-hydrated surfaces. A comparison between the fluorescence of hydrated and non-hydrated samples after immersion in the dye was made using the confocal scanning laser microscope (CSLM), where filters were used to distinguish between reflected and fluorescent light. A slight difference in intensity was observed between hydrated and non-hydrated samples. However, no spatial modulation in the fluorescent intensity was detected for length scales down to one

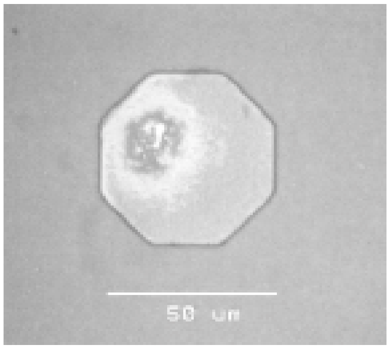

Fig. 4.3.1. Cu film covered by photoresist with a 50 µm opening to allow sulfide exposure.

micron. This result shows that either the water layer is continuous on length scales greater than 1 micron or that the preference for fluoroscein or rhodamine B dye adsorption on Cu-oxide relative to Cu-hydroxide is not great enough to detect with the CSLM.

Further experiments to elucidate the nature of the water layer were performed by using photolithography to pattern exposed Cu areas with diameters of 2 - 50 µm. Here we expected the smaller exposed areas could provide capillary wetting for the water layer to cover the entire opening, while the 50-µm exposed area would only allow droplet coverage. After exposure to an 80% RH environment containing H_2S, we observed that the 2-µm openings allowed uniform sulfide growth, while the 50 µm openings showed a “bulls-eye” pattern as shown in figure 4.3.1. This latter pattern again indicated gas-phase mass-transport limitations (microloading) in the sulfide gas supply, instead of having sulfide growth governed by restricted water adsorption.

4.4 Application of the Combinatorial Microlab Approach with Electrical Resistivity Sensors

In solid-state science, parallel experiments with rapid screening of the results are often referred to as combinatorial experiments (8). In this study, a matrix of experiments was performed in which the copper-oxide layer (oxide type and thickness), surface impurity concentrations, and point defect levels were varied systematically to assess the mechanism of solid-state transport by vacancy-mediated diffusion. Solid-state diffusion of vacancies and di-vacancies in Cu, Cu_2O, CuO, and Cu_2S may be key processes determining the kinetics of Cu sulfidation. This section addresses the role point defects and vacancy traps have on the relative rate of copper sulfidation. The effect of varying oxide type and thickness will be described in a later section.

4.4.1. Experiment

Copper films (770-875 nm thick) were electron beam evaporated at 35-42°C and at a rate of 0.15-0.3 nm/s onto SiO_2 coated Si wafers. The evaporation source material was 99.9999 at.% Cu. The base pressure of the sample preparation system was 2×10^{-8} Torr. These samples were then exposed to either a backfill of O_2 gas at 1 Torr pressure and 25ºC, or an electron cyclotron resonance (ECR) O_2 plasma at temperatures varying from 35ºC to 150ºC. The O_2 backfill formed Cu_2O at the surface, ≈1.5 nm thick, (simulating a native oxide) and the ECR O_2 plasma formed CuO at the surface, ≈3.0 nm thick, which can be reduced to Cu_2O through ion irradiation. Portions of the sample were then lithographically patterned into micron-scale meander-pattern resistance lines (R=80-100 Ω).

In order to photolithographically form the meander lines, the samples were spun dry in a spray of isopropanol to rinse possible contaminant particles from the Cu surface. They were pre-baked in air at 90°C for 2-5 min, and Hoechst Celanese AZ5214 photoresist was applied while the samples spun at 4000 rpm for 30 s. This procedure produces a 1.5-2 µm thick layer of photoresist that was cured in air at 90°C for 90 s. The samples were exposed for 10 s to UV light through a contact mask that exposed all areas of photoresist except those areas where the meander line would form. The samples were immersed for 20 s in Hoechst Celanese AZ400K developer diluted 1 part to 4 parts in deionized water. After developing, the samples were rinsed in deionized water and blown dry with N_2. In order to form the meander line, the sample was immersed for 10-20 s in a Cu etchant of H_3PO_4:CH_3COOH:HNO_3:H_2O in a ratio of 4:4:1:1. This etchant time is sufficient to etch through ~1 µm of Cu with a lateral undercut of the photoresist of about 3 µm. That is, a patterned photoresist meander line of 20 µm width will be transferred into the Cu with a resulting linewidth of 14 µm. After etching, the samples were rinsed in deionized water and blown dry with CO_2. The photoresist was removed by immersing the sample in acetone, then rinsing with methanol, and blowing dry with CO_2.

Figure 4.4.1.1 shows a schematic representation of the combinatorial defect experimental matrix, at left. Each element of the matrix contains a patterned resistance line made from the Cu film. The change in resistance was monitored simultaneously for all meander lines to provide an instantaneous, in-situ metric of the amount of sulfide formation (described below in more detail). These resistance lines were ion implanted with different species to either form additional point defects in the copper (Cu), impurities (D and O), or serve as Cu vacancy traps (Al and In). Two sets of samples were examined: one with the native oxide (Cu_2O) surface layer and one with the thin ECR oxide layer (CuO layer).

The sulfidation of both broad areas and meander lines was evaluated for implanted samples and control samples (unimplanted). Samples were ion implanted with either In, Al, or O to form a uniform concentration profile of 0.5 at.% up to a depth of 150 nm. Another set of samples was implanted with 13 keV D to form an implantation profile centered at a depth of 107 nm with a FWHM of 120 nm. Other samples were implanted with Cu to produce the same

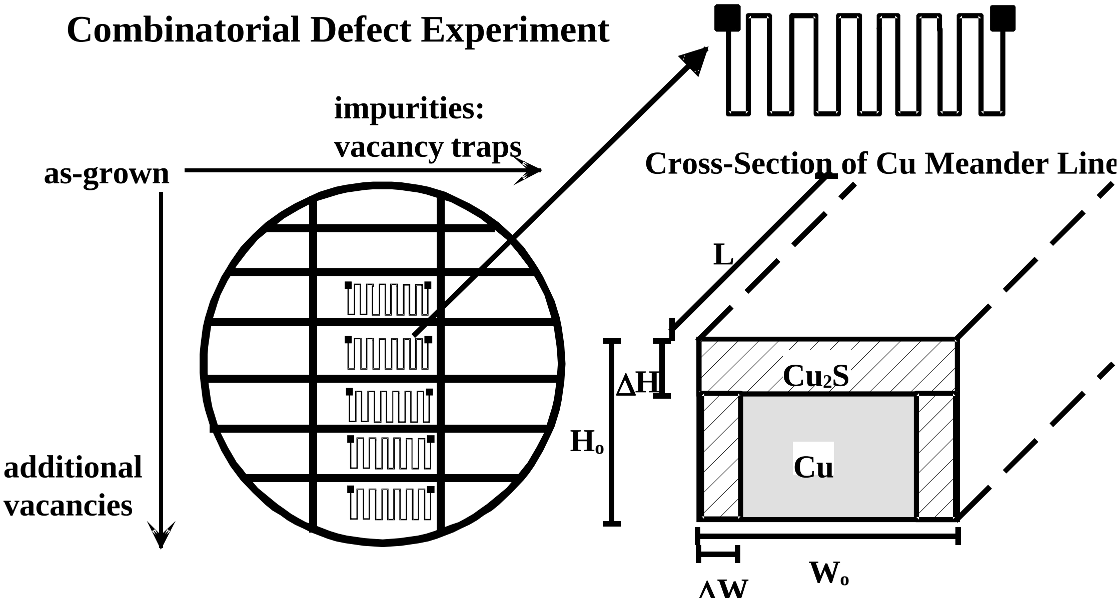

Figure 4.4.1.1. Schematic representation of the combinatorial defect experimental matrix (left). An expanded plan view of a Cu resistance meander line is shown in the upper right. The schematic cross-sectional view of one leg of the resistance line (lower right) also indicates the physical length parameters used to determine a correlation between resistance and the quantity of Cu_2S formed.

atomic displacement damage profile as the In implantation. The ion implantation energies and fluences are given in Table I. The In and Al are thought to form vacancy traps that could slow the sulfidation reaction by limiting the Cu permeability and thus influence the supply of Cu (9). Resistance changes in the meander lines were monitored, in-situ, as a function of exposure time to a 50 ppb H_2S, 80% RH, air environment at 35ºC. Control samples were tested to examine possible effects of current flowing through the resistance lines during sulfidation: one drawing current continuously and the other tested at infrequent intervals to minimize current flow.

Table 4.4.1.1. Ion Implantation Conditions

Species ⇨ Implant # ⇩	D	O	Al	Cu	In
1	13 keV, $5.5\text{x}10^{15}$ cm^{-2}	95 keV, $5\text{x}10^{15}$ cm^{-2}	140 keV, $5.2\text{x}10^{15}$ cm^{-2}	345 keV, $8\text{x}10^{15}$ cm^{-2}	600 keV, $4\text{x}10^{15}$ cm^{-2}
2		45 keV, $1\text{x}10^{15}$ cm^{-2}	75 keV, $7\text{x}10^{14}$ cm^{-2}	175 keV, $8\text{x}10^{14}$ cm^{-2}	300 keV, $8\text{x}10^{14}$ cm^{-2}
3		20 keV, $8\text{x}10^{14}$ cm^{-2}	30 keV, $8\text{x}10^{14}$ cm^{-2}	80 keV, $1\text{x}10^{15}$ cm^{-2}	125 keV, $8\text{x}10^{14}$ cm^{-2}
4				30 keV, $6\text{x}10^{14}$ cm^{-2}	30 keV, $2.5\text{x}10^{14}$ cm^{-2}

Electrical contact to the meander lines was made by soldering 1 mil diameter Au wires to contact pads connected to the meander lines. Pure In was used as the solder and a solder flux was applied to facilitate adhesion of the solder. The other end of the Au wire was soldered to a circuit board that had pre-patterned solder connection points. The assembly of Cu meander lines attached to a circuit board was loaded into the sulfidation chamber and initial measurements of the resistance were made to ensure the samples had reached stable values before the introduction of H_2S.

Following exposure, the morphology and composition of the sulfide layer grown on the meander lines were examined using scanning electron microscopy (SEM) with an attached capability for energy dispersive x-ray spectroscopy (EDS), and using micro-area Rutherford backscattering spectrometry (RBS). Total Cu_2S thickness after 290 min. H_2S exposure was measured using ion beam analysis of the broad area samples and the meander lines (micro-focused RBS).

4.4.2. Results and discussion

The increase in quantity of Cu_2S formed on the meander lines was determined from an increase in resistance (R) which is given by: $R=\rho L/A$; where ρ is the resistivity of Cu ($\approx$ 1.6 µΩ-cm), L is the length of the Cu line, and A is the cross-sectional area of the Cu line (A=HW, from Fig. 4.4.1.1.). The Cu_2S is assumed to have a negligible contribution to conductance of the meander lines based on the semiconductor properties of Cu_2S and the discontinuous, porous structure formed by the Cu_2S layer (10). Therefore, the loss of Cu to form Cu_2S increases the resistance by reducing the thickness of the Cu by ΔH, and possibly the width of the line by ΔW, as shown in Fig. 4.4.1.1. (Note that in this figure, the decrease in Cu height is ΔH which would actually produce a Cu_2S layer which is $2\Delta H$ high as a result of difference in atomic density between Cu and Cu_2S). The change in cross-sectional area of Cu is then given by:

$$\Delta A_t = \left(\frac{1}{R_o} - \frac{1}{R_t}\right) R_o H_o W_o$$

where R_o and R_t are the initial resistance and resistance at time t. An optical microscopy survey of the lines before sulfidation yielded an average linewidth of 14 µm ± 1 µm. The sulfidation was expected to affect predominantly the thickness, because the lines are ~1 µm thick and 14 µm wide. Thus, if ΔW is negligible, then

$$\Delta H_t = \left(\frac{1}{R_o} - \frac{1}{R_t}\right) R_o H_o \, .$$

The results of the Cu meander line experiments for the ECR-oxidized samples are shown in figure 4.4.2.1a and b. The results for the simulated air-oxidized samples were the same as the ECR-oxidized samples, and therefore only the ECR-oxidized samples will be presented for clarity in the figures. Figure 4.4.2.1a shows the change in area, measured from the change in resistance, falls nicely into three distinctive groupings: (I) rapid change in area for D and Cu implanted samples (upper two curves), (II) moderate change in area for the two control samples (with and without continuous current flow) and the O-implanted sample, and (III) slow change in area for Al and In implanted samples (bottom two curves). TRIM-92 ion implantation simulations show that the implantation conditions used in these experiments produce a plateau of damage to a depth of ~80 nm and then have a damage tail which extends 200 nm into the samples (11). The primary difference in comparing defect production from the different implantations is the level of damage. The plateau levels of damage (measured in displacements per atom, dpa) for the implantations are as follows: In - 85 dpa, Cu - 85 dpa, Al - 20 dpa, O - 9 dpa, and D - 0.14 dpa. Point defects created by ion implantation are known to anneal-out to some extent at room temperature (12). However, assuming equivalent driving force for defect annihilation occurs for the different samples, then the relative amount of residual point defects remaining in the Cu lines would be as indicated. That is, the In implanted sample contains 600 times the residual damage that the D implanted sample contains. Therefore, figure 4.4.2.1a shows that the In and Al are effective at slowing the sulfidation reaction, presumably by trapping vacancies that could slow the Cu permeability. For an equivalent amount of damage as created by the In implant, the Cu implantation causes the reaction rate to increase, and notably more quickly than the unimplanted control samples. The flow of current through the lines did not measurably affect the rate of sulfidation nor did the O implantation. However, the D implantation, which produced the least amount of damage, had a sulfidation rate as high as the most damaged Cu-implanted sample. This latter result suggests that the presence of hydrogen species in the Cu can either increase the Cu permeability or enhance the reaction rate by a lowering of the activation barrier for the reaction. The hydrogenation and the behavior of trapped hydrogen on the Cu corrosion rate must be explored more fully.

As explained above, if the amount of sulfidation on the sides of the meander lines is small, then the initial width of the line is unchanged and the resultant change in thickness can be used to calculate the sulfidation rate as shown in Fig. 4.4.2.1b. The three groupings of rates are

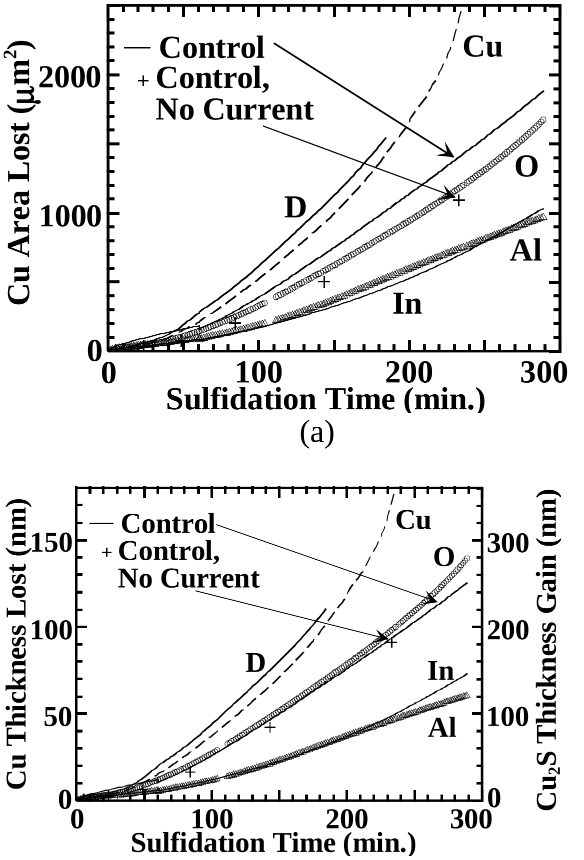

(a)

(b)

Figure 4.4.2.1. Quantity of Cu lost to sulfidation as determined from change in resistance of ECR-oxidized and implanted meander lines: (a) cross-sectional area, and (b) thickness reduction assuming negligible reduction in line width.

then: (I) enhanced sulfidation rate for D and Cu implanted samples yielding 85 nm Cu_2S/hr; (II) "control rate" for the two control samples and the O-implanted sample yielding 62 nm Cu_2S/hr; and (III) decreased rate for Al and In implanted samples yielding 31 nm Cu_2S/hr. Again, the relative rates determined in these experiments suggest that the sulfidation rate correlates to vacancy permeability (vacancy concentration times vacancy diffusion). However, micron-area RBS analysis showed that all three groups of sulfidation rates for the Cu meander lines were found to be 2-3 times greater than that of the broad-area samples made from the same films, but un-patterned. Nevertheless, the RBS analysis of the broad area implanted samples showed the thickness of the Cu_2S layer increased sequentially from the In-implanted sample to the O-implanted sample to the D-implanted sample. Some, as yet unidentified, effects produce a greater loss of Cu from the meander lines than from the broad area samples. This result cannot be simply explained by a loss of Cu due to sulfidation along the sides. (Note that localized narrowing of Cu lines as a result of enhanced sulfidation was not observed in the SEM analysis.) Some possible mechanisms that may yield a different sulfidation rate for the narrow lines include an increase in rate from prior chemical attack from the patterning process, a difference in gas-phase transport (a possible rate limiting process), stress induced in the lines from patterning, or the presence of a chloride contaminant (discussed at the end of this section).

Scanning electron microscopy was used to examine the morphology of the sulfidized layer, and EDS analysis was used to measure the relative amount of sulfur in the samples. Figure 4.4.2.2 shows typical line segments comparing the ECR-oxidized In-implanted line to the O-implanted and D implanted lines after 290 minutes of exposure to the H_2S environment. The EDS scans taken from the center of these meander lines give the following relative atomic percentages (assuming %Cu+%S = 100 at.%): the In sample yields 0.7 %S, O yields 5 %S, and D yields 7 %S. Thus, the relative amounts of sulfidation determined from the change in resistance were corroborated by EDS analysis. However, the line widths were found to vary considerably between the samples. The In sample (Fig. 4.4.2.2a) shows negligible broadening whereas the O-implanted and D- implanted samples exhibited successively greater broadening of the lines. EDS analysis of the broadened edge region of the D-implanted sample yielded a composition of 27 at.% S, suggesting that this region was fully sulfidized to Cu_2S that grew

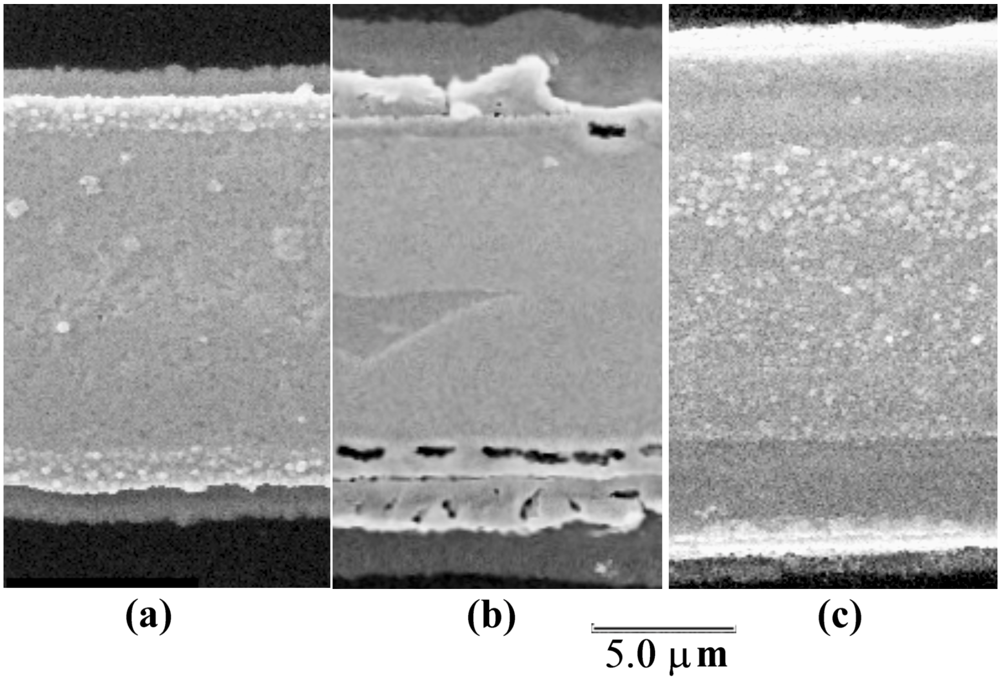

Figure 4.4.2.2. SEM micrographs of typical segments of Cu meander lines after 290 minutes of exposure to the H_2S environment for the: (a) In-implanted ECR-oxidized sample, (b) O-implanted ECR-oxidized sample, and (c) D-implanted ECR-oxidized sample. The line width is measured in the vertical direction.

laterally away from the line. The other two samples did not show such a large concentration of S in the edge regions. The deuterium apparently enhances the release of Cu to permit lateral growth of Cu_2S at an enhanced rate in comparison to the In-implanted sample. Further, the O-implanted sample (Fig. 4.4.2.2b) shows void formation at the edges of the meander line that would occur if the predominant moving species was Cu diffusing laterally away from the line by a vacancy-mediated process.

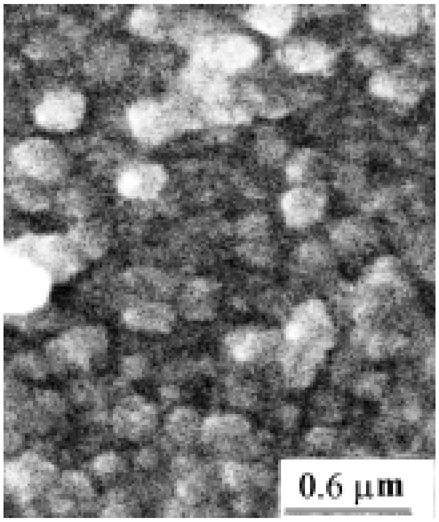

Figure 4.4.2.3. SEM image showing the surface of a sulfidized In-implanted sample.

Figure 4.4.2.3 shows an SEM image that is typical of the Cu_2S morphology formed on the surface of the meander lines. The Cu_2S forms grains which are 200-250 nm in size and poorly connected, which produces a rather porous layer. This morphology supports the assumption stated earlier, that the discontinuous Cu_2S layer would not contribute to electrical conduction of the meander line.

The EDS analysis also showed that the meander lines contained a significant amount of Cl impurity. This result and the decreased amount of sulfidation for the In-implanted sample was confirmed using micro-area RBS analysis of selected meander lines using a 15 µm x 50 µm spot for analysis. The Cl impurity may cause enhanced sulfidation rates for the meander lines in comparison to the broad-area samples. The most likely route for incorporating the Cl impurity into the samples is through surface diffusion from halogenated solder-flux residue.

4.4.3. Conclusion

These experiments show that it is possible to use micro-combinatorial techniques to efficiently characterize mechanistic aspects of atmospheric copper sulfidation. In this study, the electrical resistance change in micron-sized Cu meander lines that have been ion-implanted was measured during exposure to a humid H_2S environment. The resulting data showed that In and Al impurities in Cu lead to a reduction in the sulfidation rate, whereas deuterium and excess point defects increased the sulfidation rate, both relative to unimplanted control samples. These findings suggest that the sulfidation rate was influenced by the permeability of Cu; i.e., the trapping of Cu vacancies by In (or Al), or the enhanced mobility or concentration of vacancies in the presence of hydrogen. The use of the small-size lines proved beneficial because all of the experiments could be performed in-situ, simultaneously, and thereby eliminated questions concerning reproducibility of the corrosion environment. Thus, the micro-combinatorial technique helps to create internal standardization for determining relative corrosion behavior.

4.5 Determination of Solid-State Diffusing Species

Many researchers have established that the primary mechanism of ionic transport through Cu_2S is by the charged copper vacancy [26,27]. However, many of the characterization studies of the actual copper-sulfide product layer described in this report have demonstrated that the Cu_2S growth rate is often different than that of previous researchers, that different sulfidation behaviors are found for different relative humidities, and that the Cu_2S formed in this report may not be fully dense. As such, a study was performed to determine just exactly what is the primary diffusing species for two vary different relative humidities: 0.4% RH and 80% RH.

4.5.1. Introduction

Ion implantation has been used in a number of previous corrosion studies but generally the focus has been to alloy the surface to vary the corrosion susceptibility for a given base metal (e.g. steels, Al, Ti see [28]). Less work has involved the application of ion beam modification to determine mechanisms of corrosion [29]. The study described in this section is the first to use ion beams specifically to determine the influence of solid-state transport processes on the characteristics of atmospheric copper sulfidation. Solid-state diffusion of vacancies in Cu, Cu_2O, CuO, and Cu_2S may be important processes in determining the kinetics of Cu sulfidation. The findings from this study have been achieved by combining solid-state measurements of sulfidation kinetics with density-functional theory (DFT) modeling. In this latter activity, the local density approximation is used to model the energetics of vacancy diffusion and trapping in the various materials of interest. Specific topics addressed in this study include the role point defects and vacancy traps have on Cu diffusivity through the oxide and sulfide layers and the resultant relative rate of copper sulfidation. The effect of varying oxide type through ion irradiation was also examined. In this work, ion beams introduce both vacancies and alloying elements to permit the effects of sulfidation to be examined and compared with predicted behavior from the DFT calculations.

4.5.2. Experiment

Copper films were electron beam evaporated at a rate of 0.15-0.3 nm/s onto SiO_2 coated Si wafers at 35-42°C. The evaporation source material was 99.9999 at.% Cu. The base pressure of the sample preparation system was 2×10^{-8} Torr. These samples were then oxidized by either using energetic O_2^+ ions from an electron cyclotron resonance (ECR) oxygen plasma at temperatures varying from 35ºC to 60ºC or by exposure to air at room temperature. The copper films exposed to an ECR plasma formed a thin, dense surface-oxide layer that could be ion irradiated with different ion species and fluences. The O_2^+ ions in the ECR plasma, with a mean energy of approximately 30 eV, were generated using 100 Watts of 2.45 GHz microwave power and a magnetic field of 875 Gauss, forming the ECR resonance condition upstream from the deposition chamber. The plasma offered a method to controllably form CuO at the surface, ≈4.0 nm thick, in a clean UHV environment. The effects of ion irradiation on the ECR-oxidized layer were examined as a function of 200 keV Cu^+ fluence. After ECR plasma oxidation, the sample surface was examined in-situ using X-ray Photoelectron Spectroscopy (XPS), stimulated with Al Kα X Rays, in order to identify the type of oxide(s) present. The Cu $2p_{3/2}$ and O 1s core level spectra were measured as well as the Cu LMM Auger spectrum.

Table 4.5.2.1. I. Ion Implantation Conditions for Examining Surface Alloying Effects on Sulfidation

Species ⇨ Implant # ⇩	D	O	In
1	13 keV, 5.5×10^{15} cm^{-2}	95 keV, 5×10^{15} cm^{-2}	600 keV, 4×10^{15} cm^{-2}
2		45 keV, 1×10^{15} cm^{-2}	300 keV, 8×10^{14} cm^{-2}
3		20 keV, 8×10^{14} cm^{-2}	125 keV, 8×10^{14} cm^{-2}
4			30 keV, 2.5×10^{14} cm^{-2}

The copper films were also implanted with different ion species to examine the effects of surface alloying on the sulfidation rate and specifically to look for changes in the rate due to vacancy trapping. Implanted species included D, O, and In. Samples were ion implanted with either In or O to form a uniform concentration profile of 0.5 at.% up to a depth of 150 nm. Another set of samples was implanted with 13 keV D to form an implantation profile centered at a depth of 107 nm with a FWHM of 120 nm. The ion implantation energies and fluences are given in Table I. The treated copper samples were sulfidized for various times in an ambient temperature atmosphere (~23-25°C) containing 50-600 ppb H_2S, 0.4-80% relative humidity (RH), and air. Following exposure, the morphology and composition of the sulfide layer were examined using scanning electron microscopy and Rutherford backscattering spectrometry (RBS). The total thickness of the Cu_2S layer after H_2S exposure was measured using ion beam analysis of broad area samples.

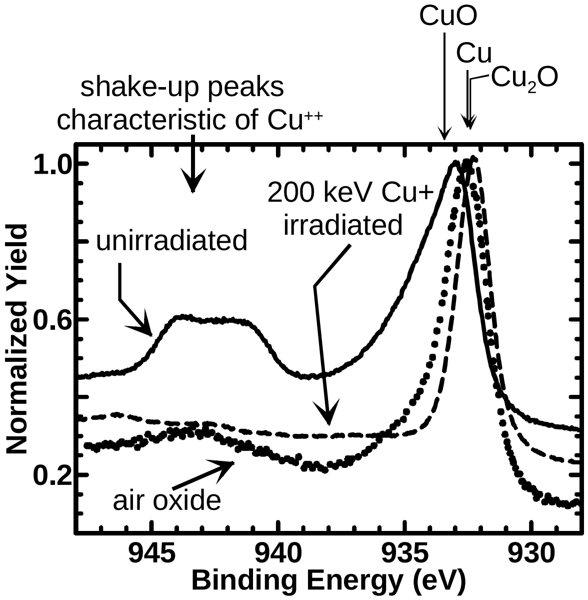

Fig. 4.5.3.1. Cu $2p_{3/2}$ XPS spectrum taken using Al Kα X-Rays for different Cu-oxides: air-formed, ECR oxidized, and ECR-oxidized and irradiated with 200 keV Cu ions. Ion irradiation increases the number of vacancies and causes a reduction in the Cu oxidation state.

4.5.3. Results and Discussion

Figure 4.5.3.1 is the XPS spectrum for the Cu $2p_{3/2}$ region from a Cu film that was exposed to an ECR O_2 plasma for 10 minutes at 50-60°C (solid line) and for the same sample after irradiation with 200 keV Cu^+ ions to a fluence of $1.6x10^{15}$ Cu/cm^2. The spectrum for a similar sample that was oxidized in air for 4 days is also shown in this figure. The Cu $2p_{3/2}$ peak positions for CuO, Cu and Cu_2O are marked with arrows at the top of the figure. In addition, the broad shake-up peak (at 940 to 945 eV) is also indicated, which is a characteristic peak of Cu in the +2 oxidation state. Analysis of these spectra combined with the O 1s and Cu LMM Auger transitions (not shown) demonstrated that the surface of the ECR oxidized sample is primarily composed of CuO [with possibly a small amount of $Cu(OH)_2$] whereas the native air-oxide is Cu_2O with a minor amount of Cu in a +2 oxidation state. Strikingly, the irradiated CuO surface was completely converted from a +2 oxidation state to a +1 state (no visible sign of a shake-up peak and a significant shift in the primary peak at 932.5 eV).

The structure of Cu_2O is a fairly open, simple cubic structure with 2 formula units per cell. It has a density of 6.1 g/cm^3 and a molecular weight of 143.09 g/mole. In comparison, the structure of CuO is a more compact monoclinic crystal with 4 formula units per cell and a density of 6.51 g/cm^3, while having a molecular weight of only 79.55 g/mole. Thus, it is expected that the barrier for diffusion through the more compact CuO structure would be considerably higher.

A TRIM [30] calculation showed that the Cu ion average range (R_p) is 58 nm (with a ΔR_p of 25 nm) which is much greater than the thickness of the oxide (≈ 4 nm). Therefore, the compositional changes in the oxide layer from the tail of the Cu implant are expected to be minimal. However, the level of point defects for this fluence is high, increasing with depth in the oxide layer up to about 3 displacements per atom (dpa). Such a high level of defects causes a complete reduction in the oxidation state of Cu in the oxide from Cu^{++} to Cu^+. It is reasonable to assume that Cu would need to migrate in from the substrate to accommodate this complete change in the oxidation state. The existence of such a process would then require a high mobility of Cu into and through the highly defected oxide.

By comparing the sulfidation behavior of the CuO/Cu to the Cu_2O/Cu formed from the matrix experiment shown in figure 4.1.4, a better understanding was obtained of the solid-state diffusion processes involved in the sulfidation of copper. Samples with oxidized surfaces that were completely Cu_2O were compared to those with surfaces that were completely CuO. After exposure for 5.5 hours at 24°C to a 65% relative humidity air atmosphere containing 600 ppb

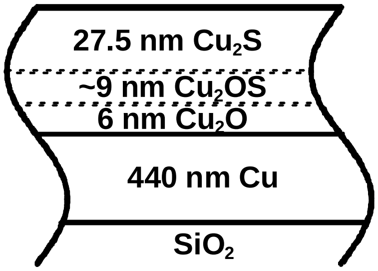

Fig. 4.5.3.2a. Ion beam analysis of each cell from the matrix represented in Fig. 4.1.4 reveals how the sulfidation reaction proceeds.

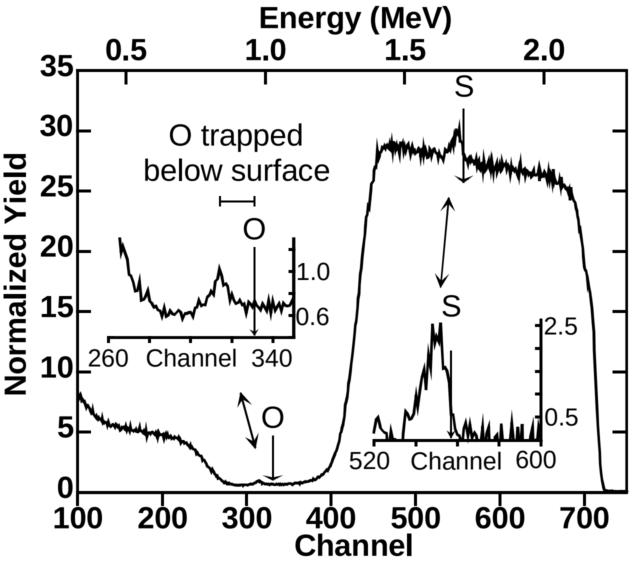

Fig. 4.5.3.2. RBS spectrum from an ECR-oxidized sample implanted with 200 keV Cu to a fluence of $1x10^{15}$ Cu/cm^2 and then sulfidized for 5.5 hours in a 65% RH air environment containing 600 ppb H_2S. The RBS spectrum was collected using 2.8 MeV He ions incident at 45° from the surface normal and a scattering angle of 164°.

H_2S, the CuO-covered sample showed no visible (or measurable by ion beam analysis) sign of sulfidation whereas the sample with a Cu_2O layer formed a Cu_2S layer ≈32 nm thick. Fig. 4.5.3.2b shows the RBS spectrum for the portion of a sample with an initial CuO/Cu_2O thickness of 5-6 nm. A representation of the composition depth profile determined for the sample is shown at left (Fig. 4.5.3.2a.). Approximately the same thickness of sulfide layer, 27-28 nm Cu_2S, was formed for different initial-thickness oxide layers. The Cu_2S grew on top of a layer with mixed oxygen and sulfur content (possibly representative of the porous structure in the top sulfide layer, a ternary compound, or a layer of mixed oxide and sulfide phases). These sulfur containing layers were present on top of a Cu_2O layer (thicker than the initial CuO layer). The existence of this buried oxide layer suggests that either Cu diffuses through the oxide to react and form the sulfide layer causing the oxide layer to become buried, or the oxide layer is sulfided in such a fashion that oxygen is released and caused to diffuse deeper into the substrate where it reacts at the Cu/oxide interface. While the latter reaction mechanism seems less plausible, marker experiments are required to determine the predominant diffusing species and the interface boundary motion. Further, the fact that the amount of oxygen in the sample is increasing during the sulfidation process suggests that more complicated coupled reactions are occurring in these initial stages of corrosion than simply explained by the model of Graedel given above [6,7]. It also suggests that further work was required to understand hydration and oxide growth in the H_2S or other complex air environments.

Modeling calculations were performed to determine the single-site Cu-vacancy formation energy and the split-vacancy formation energy in Cu_2O. These calculations employed the Vienna Ab Initio Simulation Package (VASP) [31] and utilized ultrasoft pseudo-potentials [32] within the framework of the Kohn-Sham formulation of density-functional theory [33]. The split vacancy is one formed when a Cu atom is removed from the Cu sub-lattice and the crystal is allowed to relax to an equilibrium state (at T=0 K) such that a neighboring Cu atom relaxes into an interstitial site (approximately half way toward the vacant site). The net result of this

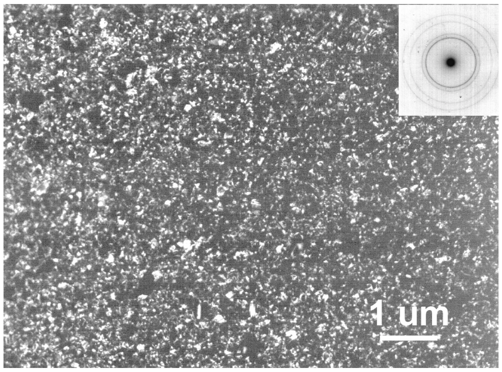

Fig. 4.5.3.3. Plan view TEM analysis of ECR-oxidized copper (CuO). Comparison to TEM of Cu_2O shows both Cu_2O and CuO have 10-100 nm grain size.

relaxation is to split the single vacancy between the two sites adjacent to the relaxed Cu in the interstitial site. The split-vacancy formation energy is approximately 0.10 eV lower than the single-vacancy formation energy (depending slightly on the charge state of the vacancy). The barrier for Cu-vacancy diffusion through the split-vacancy site is ≈0.3 eV whereas the barrier for diffusion through the single-vacancy site (no relaxation allowed) is ≈0.75 eV. In either case, the barrier for Cu-vacancy diffusion through Cu_2O is small suggesting that Cu should be relatively mobile in and through Cu_2O (especially through the split-vacancy site). Transmission electron microscopy of ECR-oxidized copper shown in figure 4.5.3.3 revealed that the grain sizes for both CuO and Cu_2O ranged from 10 to 100 nm. Therefore, with such small but equivalent grain sizes for the two oxides, if copper sulfidation were primarily dependent upon grain boundary diffusion through the oxide, then similar sulfidation rates should have been found for the CuO and Cu_2O samples.

Combining the results from the DFT calculations, the TEM analysis, and the experimental results suggest that the sulfidation rate is slowed or completely suppressed by increasing the barrier to Cu-vacancy diffusion. Another possible finding based on the experimental results is that if the sulfidation process depends on supplying copper to the surface, then lattice diffusion is as important if not more important than grain-boundary diffusion.

Further examination of the oxygen and sulfur signals in the RBS spectrum of figure 4.5.3.2 indicates only two possible reaction processes for the formation of the Cu_2S layer on the surface. This spectrum was collected from a sample that was ECR-oxidized for 19 min. at 75°C, forming a 9.4 nm thick CuO layer. The sample was implanted with 200 keV Cu and sulfidized for 5.5 hours. Further experimental details are given in the figure caption. An enlarged view of the S signal (with background subtracted) and the O signal are shown as insets in Figure 4.5.3.2. Arrows in these insets indicate the positions for the surface peaks of the S and O, respectively. The sulfur clearly resides at the surface and extends in depth whereas the O signal is below the surface peak position, demonstrating that the O is trapped below the surface Cu_2S layer. Either Cu vacancies have diffused through the oxide to form a surface sulfide layer, thereby burying the oxide layer, or the surface oxide layer reacted directly to form the sulfide, releasing the O and "snowplowing" it below the sulfidized layer. The latter possibility requires the diffusion of sulfur (or S vacancies) through the sulfide layer to supply the sulfidation reaction at the Cu_2O/Cu_2S interface.

A series of inert-marker experiments were performed to confirm which of the two candidate species actually diffuses through the combined oxide/sulfide layer for both high and low relative humidity environments. These experiments were performed using bulk polycrystalline Cu substrates possessing a native Cu_2O surface. The samples were exposed for 4 hours at room temperature to a either 0.4% RH or 80% RH air environment containing 150 ppb H_2S that formed an initial Cu_2S layer 80 or 135 nm thick, respectively. A gold marker layer was then deposited to a thickness equivalent to 2 nm. However, for such a thin layer, the Au forms a low density of small patches (depicted schematically in Figure 4.5.3.5), each with a thickness

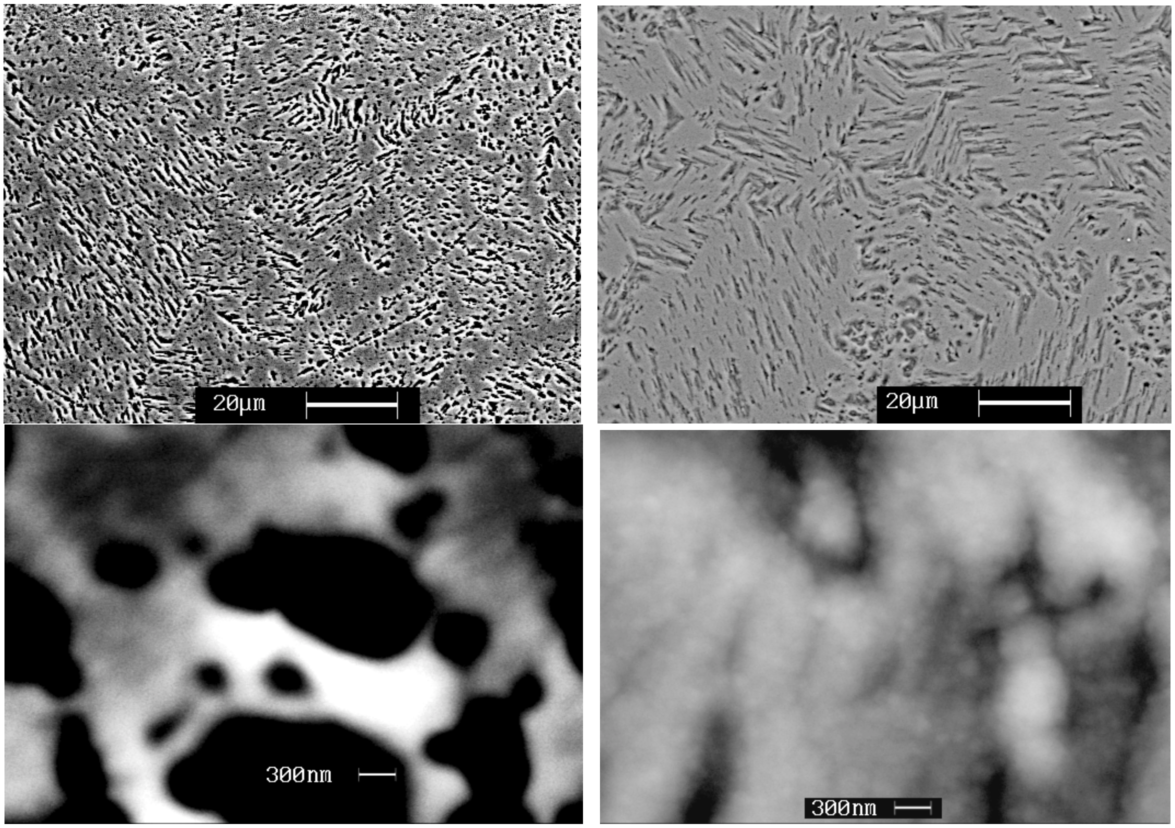

Au Markers on Cu_2S surface   Au Markers after continued sulfidation

Fig. 4.5.3.4. SEM analysis of sample with Au markers before and after markers are buried beneath Cu_2S. The lower images are simply higher magnification images from the same areas as in the upper images. All micrographs were collected using backscattered electron imaging to highlight the Z contrast between the Au and the Cu.

greater than 2 nm. The presence of this patchy Au layer was confirmed using a scanning electron microscope with backscattered electron imaging to highlight the elemental contrast between the Au and the Cu (Fig. 4.5.3.4). Many RBS spectra were collected as a function of sulfidation time, but for clarity, only 4 spectra are shown in figure 4.5.3.5 and 4.5.3.6. In figure 4.5.3.5, the spectra are from the sample sulfidized at 0.4% RH for the following times: (a) initial 4 hr. sulfidation with Au markers on top, (b) sample (a) + additional 4 hr. sulfidation, (c) sample (a) + additional 11 hr. sulfidation, and (d) sample (a) + additional 37.25 hr. sulfidation. In figure 4.5.3.6, the spectra are from the sample sulfidized at 80% RH for the following conditions: (a) initial 4 hr. sulfidation with Au markers on top, (b) sample (a) + additional 2.5 hr. sulfidation, (c) sample (a) + additional 16 hr. sulfidation, and (d) sample (a) + additional 107 hr. sulfidation. The "motion" of the Au marker to continually greater depths below the growing Cu_2S layer clearly identifies Cu vacancies are the fastest moving species through the oxide and sulfide layers for both high and low RH sulfidation. A schematic diagram depicting the composition depth profile determined from spectrum (c) in figure 4.5.3.5 is shown inset in that figure, and a schematic for the composition depth profile of spectrum (d) in figure 4.5.3.6 is shown inset in that figure. For each of the other spectra analyzed, the thickness of the layer X_o at 0.4% RH was 80 nm, and at 80% RH X_o was 135 nm; both equaled the initial sulfide thickness before depositing the Au markers. Only for the final sulfidation did the layer X_o begin to thicken slightly for the high relative humidity case. This thickening corresponds to evidence in the gas flow analysis during the final sulfidation, suggesting that the sulfide layer formed microcracks which permitted the sulfidizing species to reach the Cu substrate, without diffusing through the solid state. The fact that the thickness of layer X_o remained constant and all sulfide growth occurred above the markers for the other analyses proves that the sulfidizing species are not diffusing through the solid to react at the oxide/sulfide interface, but rather the Cu vacancies are the primary moving species at both high and low RH.

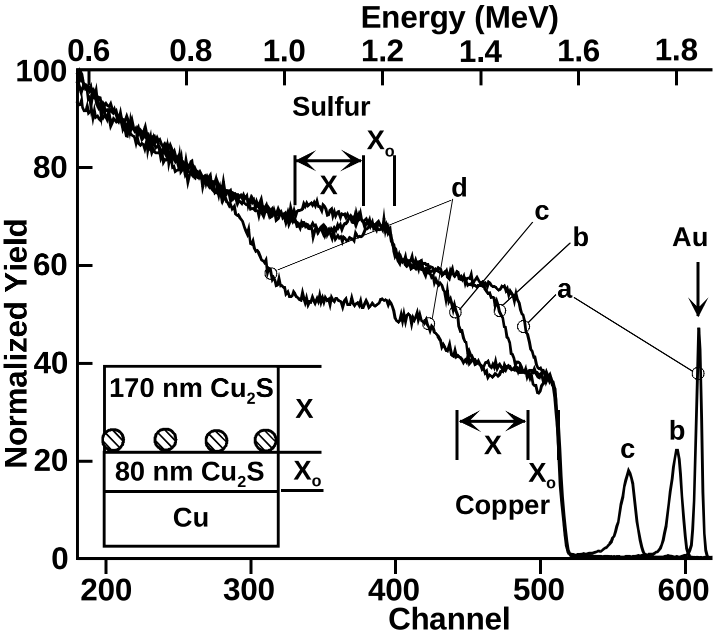

Fig. 4.5.3.5. RBS spectra collected from the 0.4% RH marker-experiment samples using 2 MeV He^+ ions incident along the sample normal and a scattering angle of 164°. The Au patches, indicated schematically in the inset, were used as markers to determine the dominant moving species.

This data can now be plotted in a way to determine the interdiffusion coefficient (***D***) for this system. Figure 4.5.3.7 is a plot of the increase in Cu_2S thickness as a function of the square root of time exposed to the 80% RH sulfidizing environment. The thickness measurements are nearly linear with the square root of

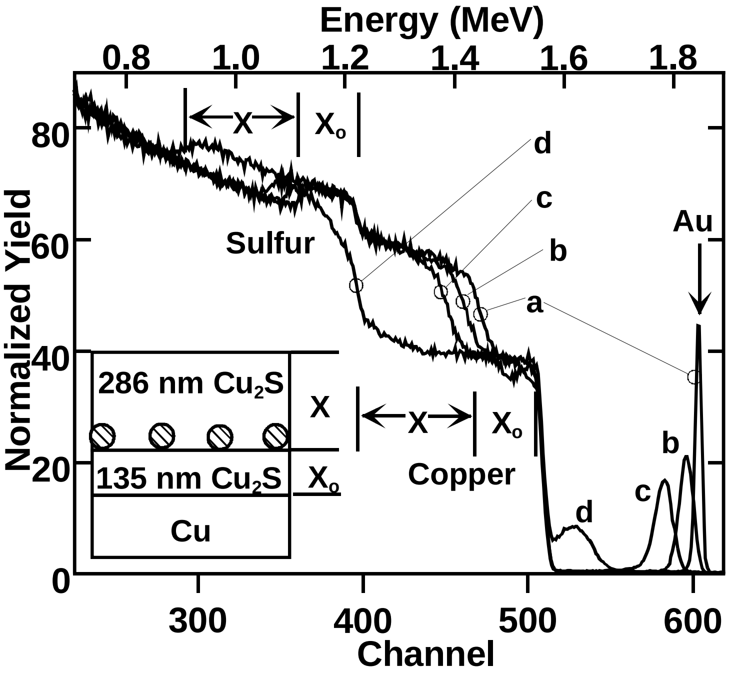

Fig. 4.5.3.6 RBS spectra collected from the 80% RH marker-experiment samples using 2 MeV He^+ ions incident along the sample normal and a scattering angle of 164°. The Au patches, indicated schematically in the inset, were used as markers to determine the dominant moving species.

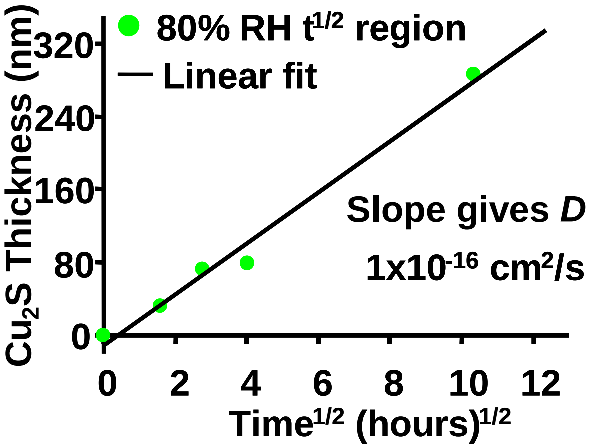

Fig. 4.5.3.7. A plot of the increase in Cu_2S thickness as a function of square root of exposure time in a 80% RH sulfidizing

time. A least squares fit to the data is shown as a solid line in this figure with a slope of 28 nm/hr$^{1/2}$. If the thickness increase corresponds to the velocity of the markers below the surface, as shown by the marker experiments, then the interdiffusion coefficient is related to X by: $X \approx 4(\boldsymbol{D}t)^{1/2}$. This gives $\boldsymbol{D} \approx (7\ \text{nm/hr}^{1/2})^2$ or ~ $1\text{x}10^{-16}$ cm^2/s. This marker treatment is independent of the diffusion mechanism and simply examines the net measurable flux of Cu and S past the markers. In the traditional treatment [34] of a marker experiment, the interdiffusion coefficient is given in terms of the chemical diffusion coefficients (D_{Cu} & D_S) for each species and their mole fractions (N_{Cu} & N_S) as: $\boldsymbol{D} = N_S D_{Cu} + N_{Cu} D_S$. The marker experiments show that the mobility of sulfur is negligible, and thus $D_{Cu} = \boldsymbol{D}/N_S \approx 4\text{x}10^{-16}$ cm^2/s. This value of a chemical diffusion for Cu in Cu_2S is several orders of magnitude faster than that reported in the literature. If the diffusion mechanism is Cu vacancy diffusion in the sulfide, then one would expect to see an accumulation of Cu vacancies in the form of voids (often referred to as Kirkendall voids) in the Cu. Images of these voids are presented in the next section 4.6.

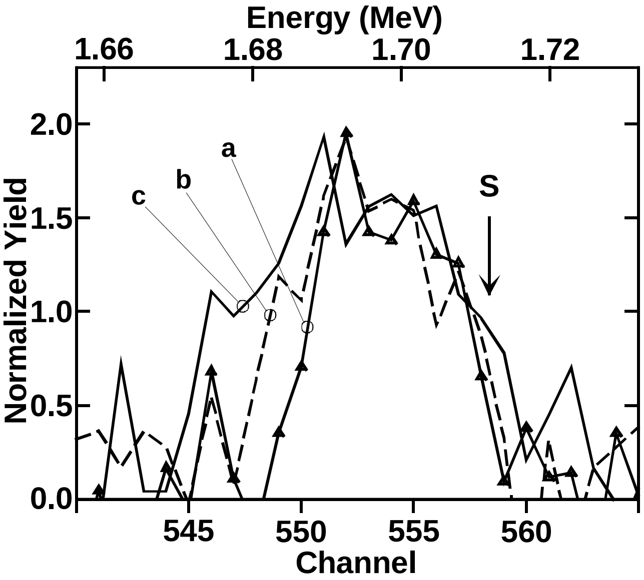

Fig. 4.5.3.8. Sulfur signals determined from RBS analysis with a 2.8 MeV He+ beam incident normal to the sample surface and with a scattering angle of 164°: (a) In implanted, (b) O implanted, and (c) D implanted. The large Cu background signal was subtracted from below the S peak for each of these spectra.

A preliminary finding of this study described earlier and based on a comparison of the relative sulfidation behavior of CuO/Cu and Cu_2O/Cu samples was that the sulfidation rate can be slowed by increasing the barrier to Cu-vacancy diffusion. This concept was further tested using ion implantation to form surface alloys that could serve as Cu-vacancy traps and thereby slow the sulfidation rate. Again, DFT was employed to calculate the binding energy of a Cu divacancy to either an Al or In substitutional atom sitting on a Cu lattice site in Cu_2O. A divacancy trap was considered in order to maintain charge neutrality for the substitutional-divacancy complex. The results of these calculations show strong trapping (binding) energies for both the Al and In substitutional atoms: $(Al_{Cu}+2V_{Cu})^o$ = 3.19 eV with respect to unbound Al_{Cu}^{2+} and $2V_{Cu}^{1-}$, and $(In_{Cu}+2V_{Cu})^o$ = 1.53 eV with respect to unbound In_{Cu}^{2+} and $2V_{Cu}^{1-}$. Thin film, ECR-oxidized Cu samples were implanted with In, O, and D according to the details shown in Table I. These samples were all sulfidized in a 50 ppb H_2S, 80% RH, air environment at 35ºC for 5 hours. The amount of sulfur uptake was measured using RBS with a 2.8 MeV He+ beam incident normal to the sample surface and with a scattering angle of 164°. The sulfur signal for these samples is given figure 4.5.3.8 with the background stripped-off: (a) In-implanted sample, (b) O-implanted sample, and (c) D-implanted sample. A control sample with only a native Cu_2O on the surface gave a spectrum equivalent to the O-implanted sample and is not shown to maintain clarity in the figure. The surface peak position for sulfur is indicated in the figure with an arrow. These peaks are barely resolved and somewhat noisy as a result of the large Cu background signal subtracted from below them. Therefore, each signal was simply integrated to give the areal density of sulfur: (a) 3.6×10^{16} S/cm^2 ± 0.6×10^{16} S/cm^2, (b) 4.8×10^{16} S/cm^2 ± 0.7×10^{16} S/cm^2, and (c) 5.9×10^{16} S/cm^2 ± 0.8×10^{16} S/cm^2. These results validate the ab initio calculation that the In is effective at slowing the sulfidation reaction, presumably by trapping vacancies, in comparison to the O-implanted sample and control sample. Further, the D implantation, which produced far less damage in the oxide layer than did the In implant, had a 65% greater sulfidation rate than did the In-implanted sample. This latter result suggests that the presence of hydrogen species in the Cu can either increase the Cu-vacancy permeability or enhance the surface reaction rate.

4.5.4. Summary

Ion implantation and ion-beam irradiation has been used in this study for the first time to determine the influence of solid-state transport processes on the behavior of copper in atmospheric-sulfidizing environments. Processes involving diffusion in Cu, Cu_2O, CuO, and Cu_2S were considered. In combination with solid-state measurements of sulfidation kinetics and density-functional theory (DFT) calculations, several findings resulted including: (1) the role point defects and vacancy traps have on Cu diffusivity through the oxide and sulfide layers and the resultant effect on sulfidation kinetics, (2) the effect of the type of surface oxide, and (3) the identification of the dominant species that diffuses through the sulfide product layer. For the native copper oxide (Cu_2O), the importance of vacancy trapping on slowing the rate of sulfidation was predicted and experimentally verified. The type of oxide proved to be important in that a CuO layer essentially prevents sulfidation whereas a Cu_2O layer permits sulfidation. Finally, solid-state transport of Cu from the substrate through the Cu_2S product layer is the primary mass transport process.

4.6 Characterization of Product Layer Microstructure

Direct observation of product-layer structure and morphology was performed to gain mechanistic insight into the sulfidation process. Several techniques were applied: transmission electron microscopy (TEM), scanning electron microscopy (SEM), and X-ray diffraction.

4.6.1. Transmission Electron Microscopy and X-Ray Diffraction

In this study, focused ion beam (FIB) cross-sectioning, transmission electron microscopy (TEM), high-resolution TEM (HRTEM), x-ray diffraction (XRD), and ion beam analysis was used to characterize the product formed when Cu is exposed to a dilute (50-200 ppb) H_2S atmosphere at low (0.5%) to high (80%) relative humidity (RH). In our investigation, two types of samples were analyzed to determine their microstructure: 1. copper films that were electron-beam evaporated onto SiO_2 coated Si wafers, and 2. bulk copper 101 disks. The electron-beam evaporated copper had a much smaller grain size (~ 10-100 nm) than the bulk Cu. Once samples was created, Rutherford backscattering spectrometry (RBS) was performed using a 2.8 MeV He+ beam with a backscattering angle of 164°. The composition depth profile was then obtained by fitting a numerical simulation to the RBS data using a program which simulates the scattering of a He+ ion of a given energy by a target whose parameters are known. Finally, transmission electron microscopy (TEM) in both planar and cross-sectional views was used to determine the phase and microstructure. TEM images were obtained from a Hitachi H-7000, 100KeV microscope using Kodak film, and from a JEOL 1210, 120KeV microscopy using a Gatan CCD camera.

This section will examine possible structural differences in the sulfides grown at high and low humidity and correlate these differences to changes in sulfidation behavior as a function of thickness. For both low and high RH exposure during sulfidation, Cu and S react and form the low chalcocite phase (Cu_2S) as identified by x-ray and electron diffraction. The results of X-ray diffraction are shown in figure 4.6.1.1. Texturing (grain orientation) was different between the sample sulfidized at 0.5% RH and the sample sulfidized at 80% RH. TEM analysis was then done to look in detail for microstructural differences between low RH and high RH samples.

Transmission electron microscopy of cross-sectioned samples demonstrated the primary difference in microstructure between the low and high RH sulfide layers. At high RH, the initial

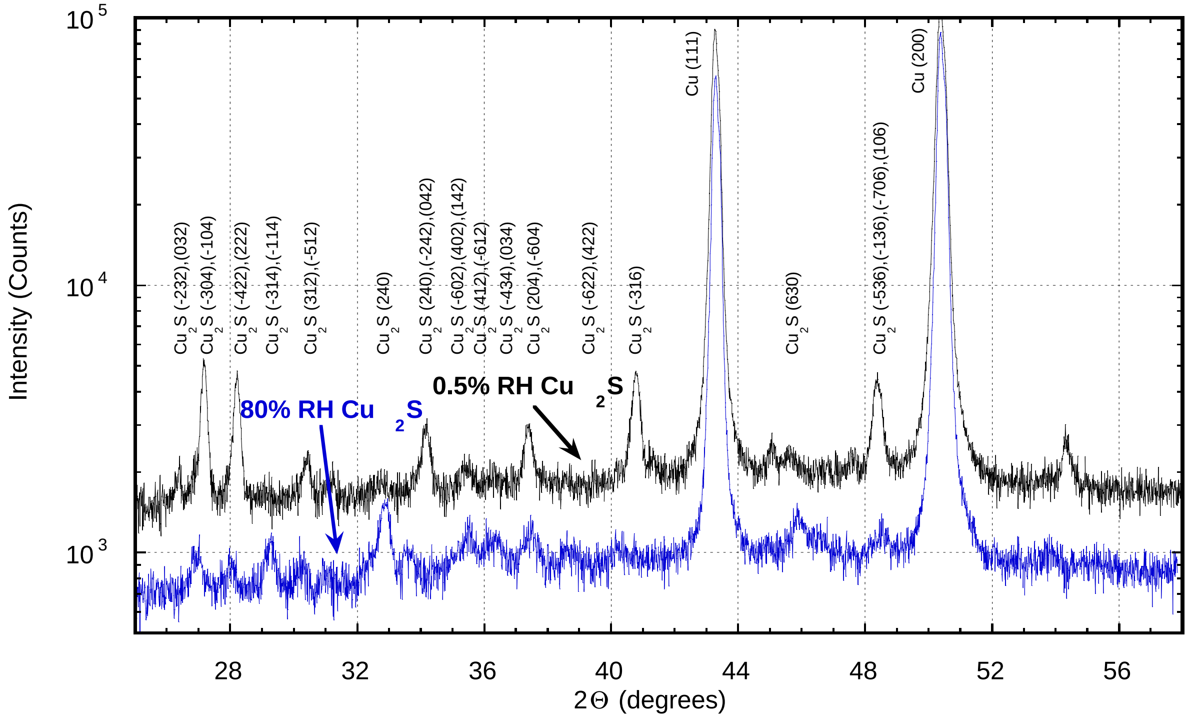

Fig. 4.6.1.1. X-ray diffraction shows that the dominant phase is monoclinic low chalcocite (Cu_2S). Texturing is different between sulfide grown at low and high relative humidities.

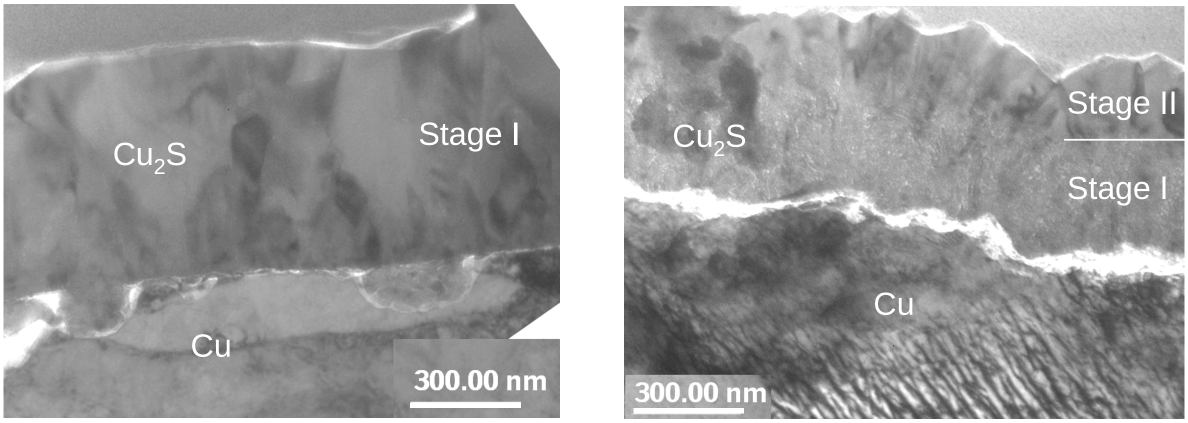

0.5% RH Sulfidation
(a)

70% RH Sulfidation
(b)

Fig. 4.6.1.2. Cross-section TEM and electron diffraction shows that the same Cu_2S phase is formed from high and low RH sulfidation at room temperature, and the product layers have similar morphology. The initial ~150nm has different grain sizes for low and high RH samples, but a beyond this 150nm the grain size and structure appears very similar.

grains formed were small (~2-5 nm in diameter) and then larger grains grew (~100 nm wide) when the sample transitioned from the linear growth regime to the square-root of time growth regime (at a Cu_2S thickness ~150 nm). At low RH, the initial grains were typically large and remained so throughout the sulfidation. Figure 4.6.1.2 is a set of cross-section TEM micrographs showing this microstructure for samples sulfidized in 0.5% RH (fig. 4.6.1.2a) and 70% RH (fig. 4.6.1.2b). The Cu_2S product layers have the same composition (as determined from RBS analysis) and phase (XRD and electron diffraction patterns). These cross-sectional views and plan-views (not shown) reveal that in the first 150 nm of Cu_2S growth, grains formed at low RH range in size between 30 nm and 50 nm whereas the grains formed at high RH range in size between 2 nm and 5 nm. Beyond the initial 150 nm of growth, similar grain size (~100 nm) exists for sulfidation at both humidities. TEM analysis reveals that in general high RH samples exhibit many bar or plate-like structures (25 x 75 nm), some of which span the entire Cu_2S layer and which tend to be more numerous at higher temperature. Finally, these micrographs demonstrate that Cu is the primary moving species through the Cu_2S layer leaving Kirkendall voids at the Cu/Cu_2S interface.

4.6.2 Scanning Electron Microscopy / Focused Ion Beam Milling

Scanning electron microscopy (SEM), energy dispersive spectroscopy (EDS), and atomic force microscopy (AFM) were used to investigate local surface morphology and surface heterogeneities in Cu_2S product layers that were grown at two humidity levels and three temperatures. A portion of this characterization work focused on the initiation stage -- after relatively short exposures (< 1 hour) of copper thin-film samples to the H_2S environment. Figure 4.6.2.1 contains three SEM images that show non-uniform surface coverage after ~ 100 nm of Cu_2S film had been grown at 80% RH and 0.5% RH with temperatures of 25°C and 35°C. Corresponding AFM images shown in figure 4.6.2.2 indicate that the regions of lower secondary electron emission seen in figure 4.6.2.1 define trenches or pits, where the surface is recessed relative to that of the surrounding matrix. The compositional profile provided with an EDS linescan (shown in figure 4.6.2.3) indicate that the Cu signal is reduced in those regions as would be expected in a pit or trench. The sulfur signal is higher than the matrix in that region, suggesting that a relatively thick particle of Cu_2S has formed within the pit. These results first suggested that both humidity and temperature may have a profound influence the local uniformity of film growth.

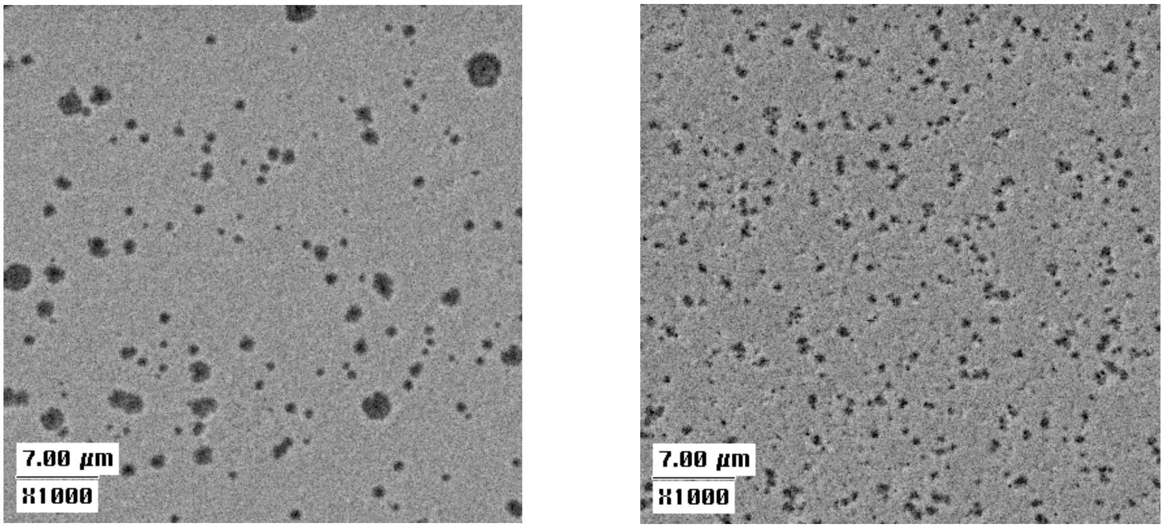

(a) 80% RH, 25^{o}C (a) 0.5% RH, 25^{o}C

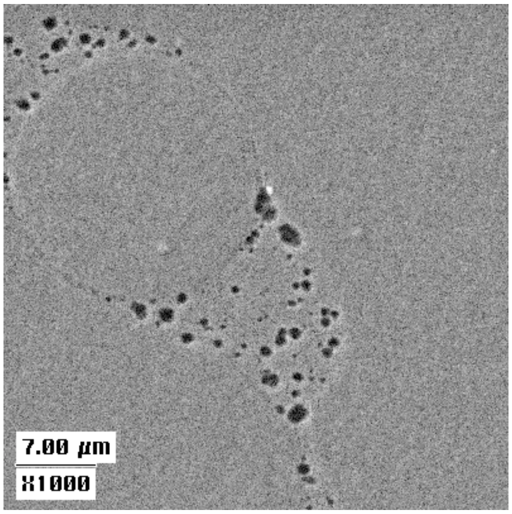

(a) 80% RH, 35^{o}C

Fig. 4.6.2.1. SEM images showing surface heterogeneities as a function of RH and temperature.

To better characterize the morphology of the product layer as a function of RH, more in-depth SEM imaging was performed on thicker layers. However, in this activity, focused-ion beam (FIB) milling or sectioning of the surface was employed to eliminate the prime disadvantage of plan-view observation – lack of definitive depth-related information. The FIB milling provides a way to avoid mechanical polishing and still produce cross sections that contain the microstructural details of interest. The dual-beam FIB/SEM instrument that was used employs a beam of 30 kV Ga^+ ions. The ions are focused into a small spot that is then rastered over the sample. This procedure produces a tightly controlled removal (milling) of material from the sample. Using an appropriate scanning pattern, deep trenches are milled into the surface of the sample (Figure 4.6.2.4a). The resulting trench can then be imaged at a high tilt in using the electron beam and the cross section examined. The ion beam can also be used to produce images in a similar manner to the typical electron beam. However, due to microstructurally induced channeling, the ion beam produces images in which the contrast is a function of the crystallographic orientation of the surface being imaged. In the samples sectioned in this study, a thin-film of Pt was first deposited to enable a smoother surface to be produced and to retain the original surface of the sample.

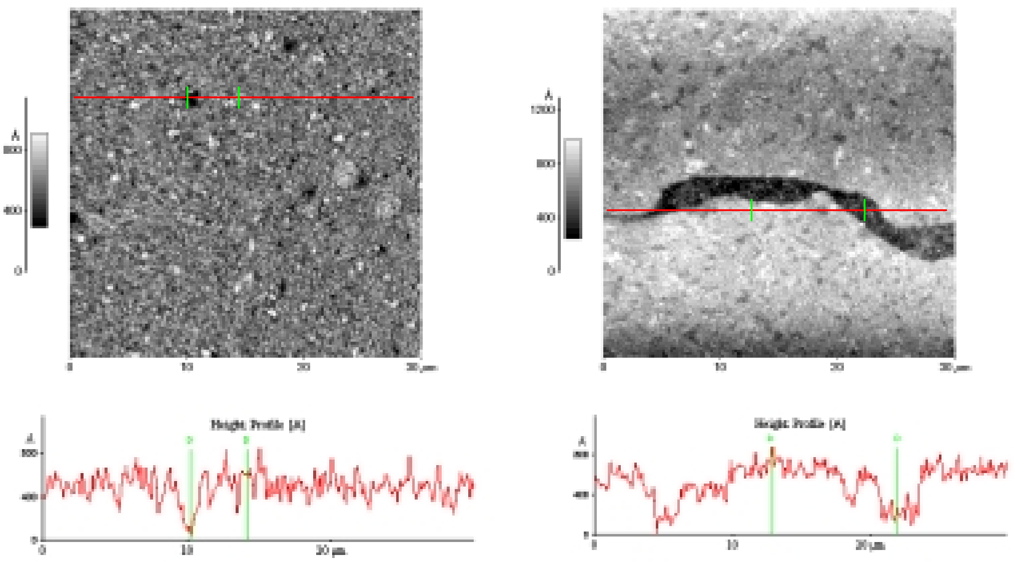
T = 25°C RH = 80%

T = 35°C RH = 80%

Figure 4.6.2.2. AFM images showing pits (left) and trenches (right) in Cu2S film growth.

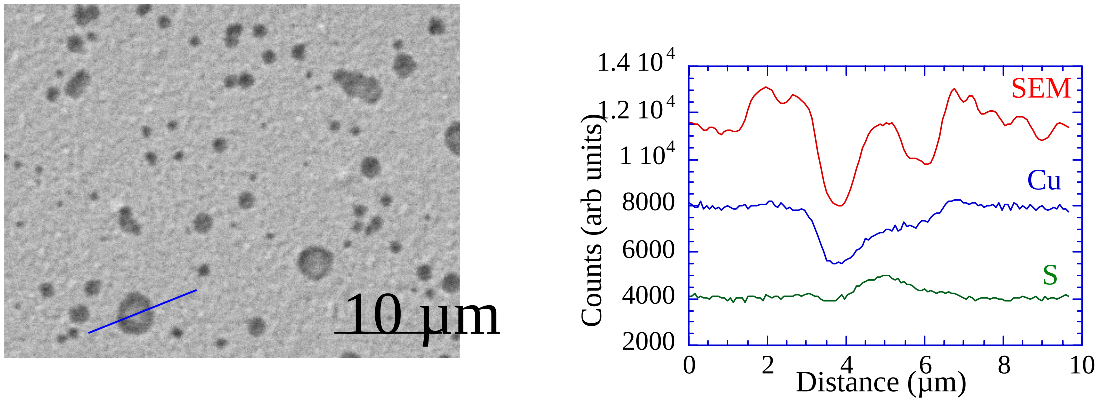

(a) SEM of linescan region

(b) EDS linescan across pit

Figure 4.6.2.3. EDS linescan across pit shows reduced Cu and elevated S relative to matrix.

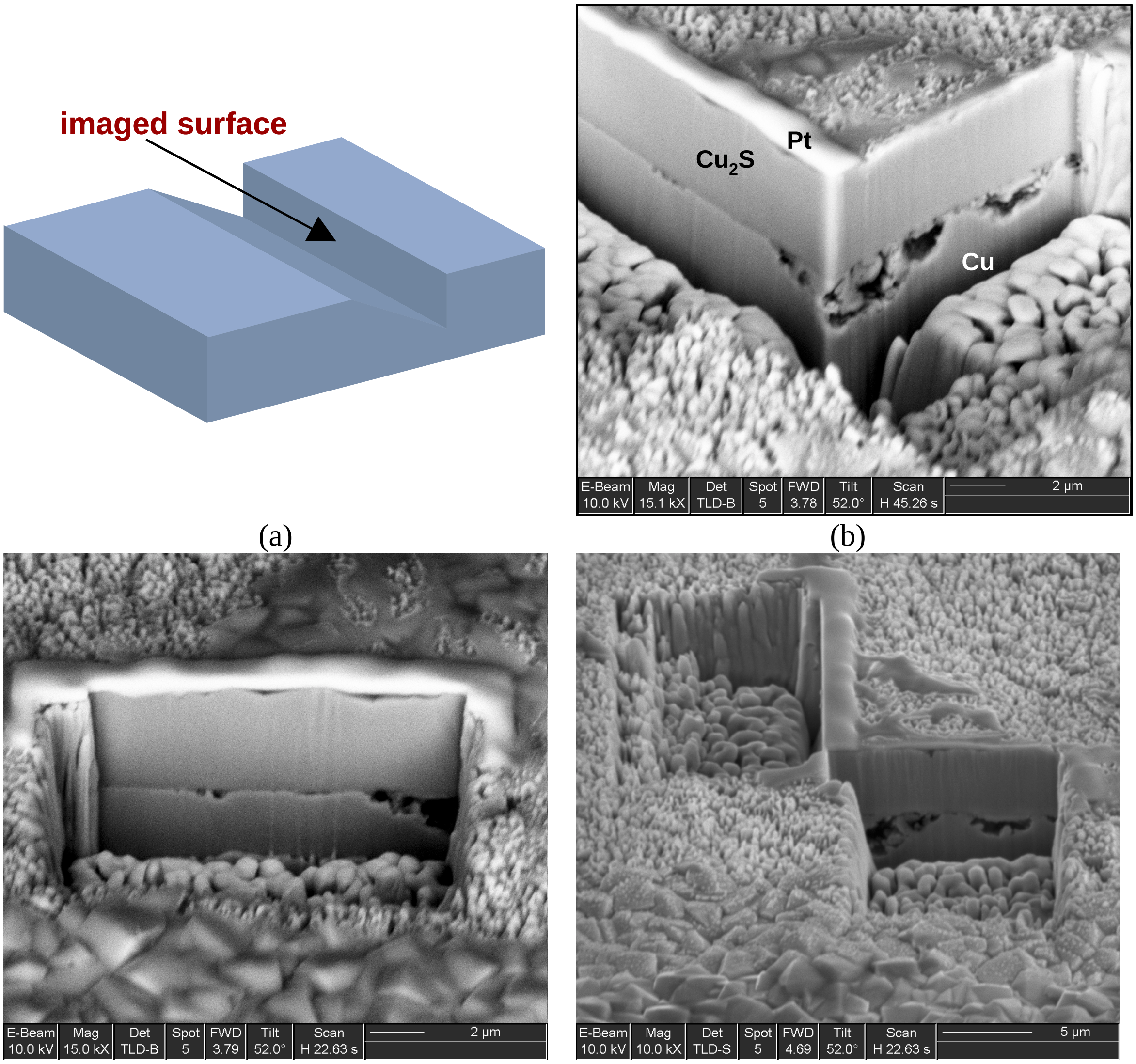

(a) (b)

(c) (d)

Fig. 4.6.2.4. SEM images of cross-sectioned copper-sulfide product layer formed at very low humidity (0.5%): (a) schematic of how the focused-ion beam is used to mill the surface, (b-d) different views of the morphology of the layer. These photographs show that the sulfidation process at low humidity is relatively uniform.

SEM images of two FIB cross-sections on a sample sulfidized at low relatively humidity (0.5%) to thickness levels > 1 µm are shown in figure 4.6.2.4b-d. The morphology of the upper (top) surface itself is relatively consistent with a granular consistency (observe the lower parts of frames (c) and (d) where the Pt layer is not present). The thickness of the Cu_2S layer is quite uniform and without any physical features of note. Porosity in the copper at the Cu-Cu_2S interface is the result of Cu vacancy coalescence. As discussed in Section 4.5, mass transport through the product layer is controlled by Cu vacancy migration and the vacancies simply coalesce near the metal surface to form voids. Figure 4.6.2.5a-c contains SEM images supporting the marker experiments that constituted the critical component of Section 4.5. Here, one can easily see the Au marker layer. Of importance, agreement between the thickness of the Cu_2S layer observed in these images, determined by RBS, and calculated using the [H_2S] mass balance was very good. An ion-beam stimulated image is included as frame (c) to show how the growth of the product layer does not appear to correlate with the underlying Cu grain structure. Frame (d) is an image taken from a sample grown at 80% RH (see next paragraph).

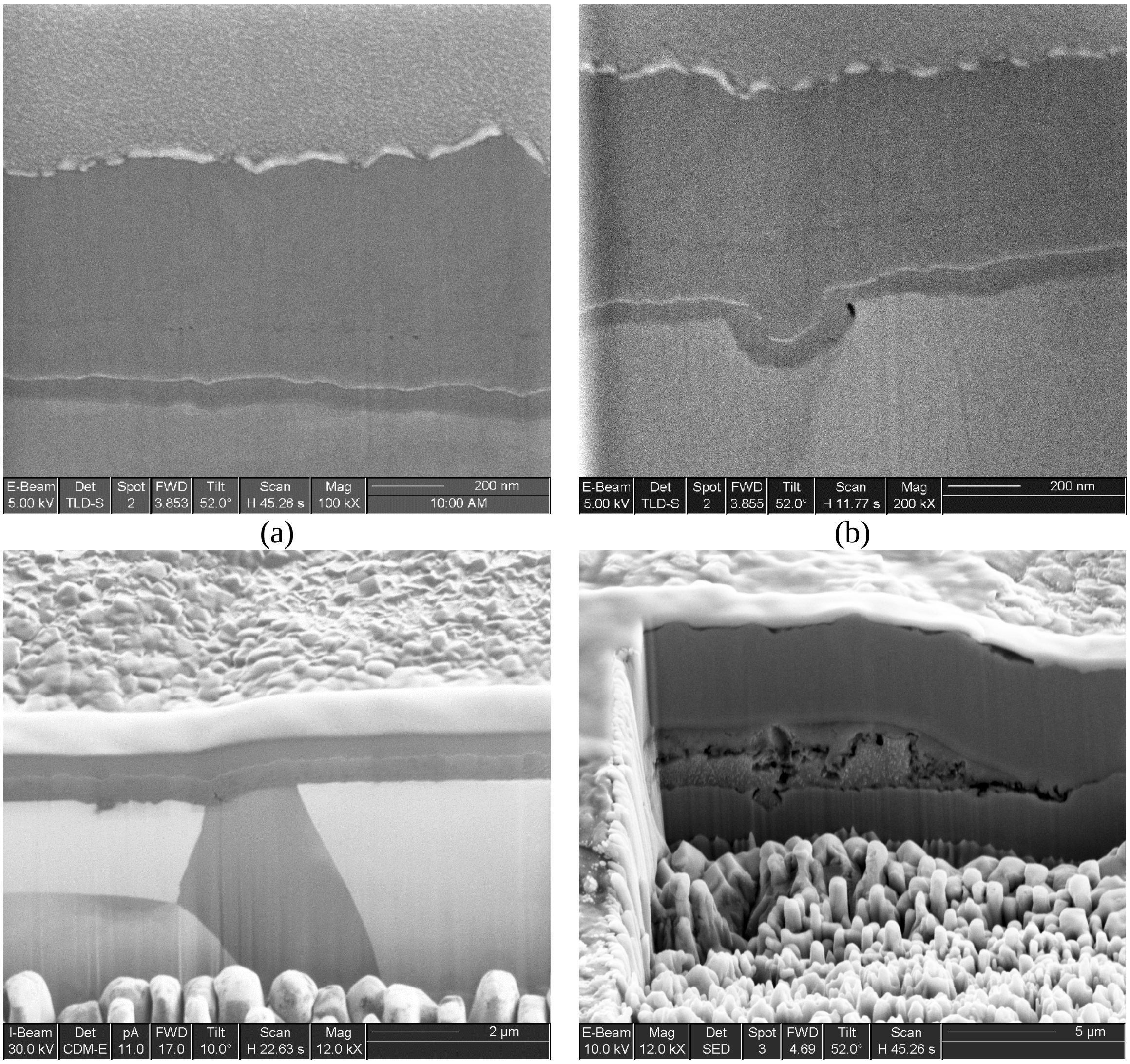

(a) (b)

(c) (d)

Fig. 4.6.2.5. Cross-section SEM images of the Cu_2S product layer grown in the low-humidity (0.5% RH) marker (a-c) experiment discussed in Section 4.5. The very thin bright band in the lower part is the Au marker layer and the top is covered by a thin layer of Pt. Figure (c) was taken using the ion-beam to highlight the grains in the Cu substrate. Figure (d) is an image from a sample sulfidized at 80% RH.

In SEM images, the uniformity of the sulfide layers produced at low humidity contrasts considerably with that for the layers formed under high humidity conditions (see Figures 4.6.2.6-4.6.2.8). Figure 4.6.2.6 is an image of the surface that contains a variety of topological features not seen at low RH levels that include patchiness and many types of defects that appear to be quite deep. Figures 4.6.2.7 and 4.6.2.8 are images of FIB cuts that dramatically show that this inconsistency extends below the surface. These and similar features clearly demonstrate the complex nature of the sulfidation process at high humidity. At present, an explanation for this apparent complex behavior has not been formulated (e.g., due to nucleation/copper oxide reaction phenomena, water distribution gradients, solid-state transport differences).

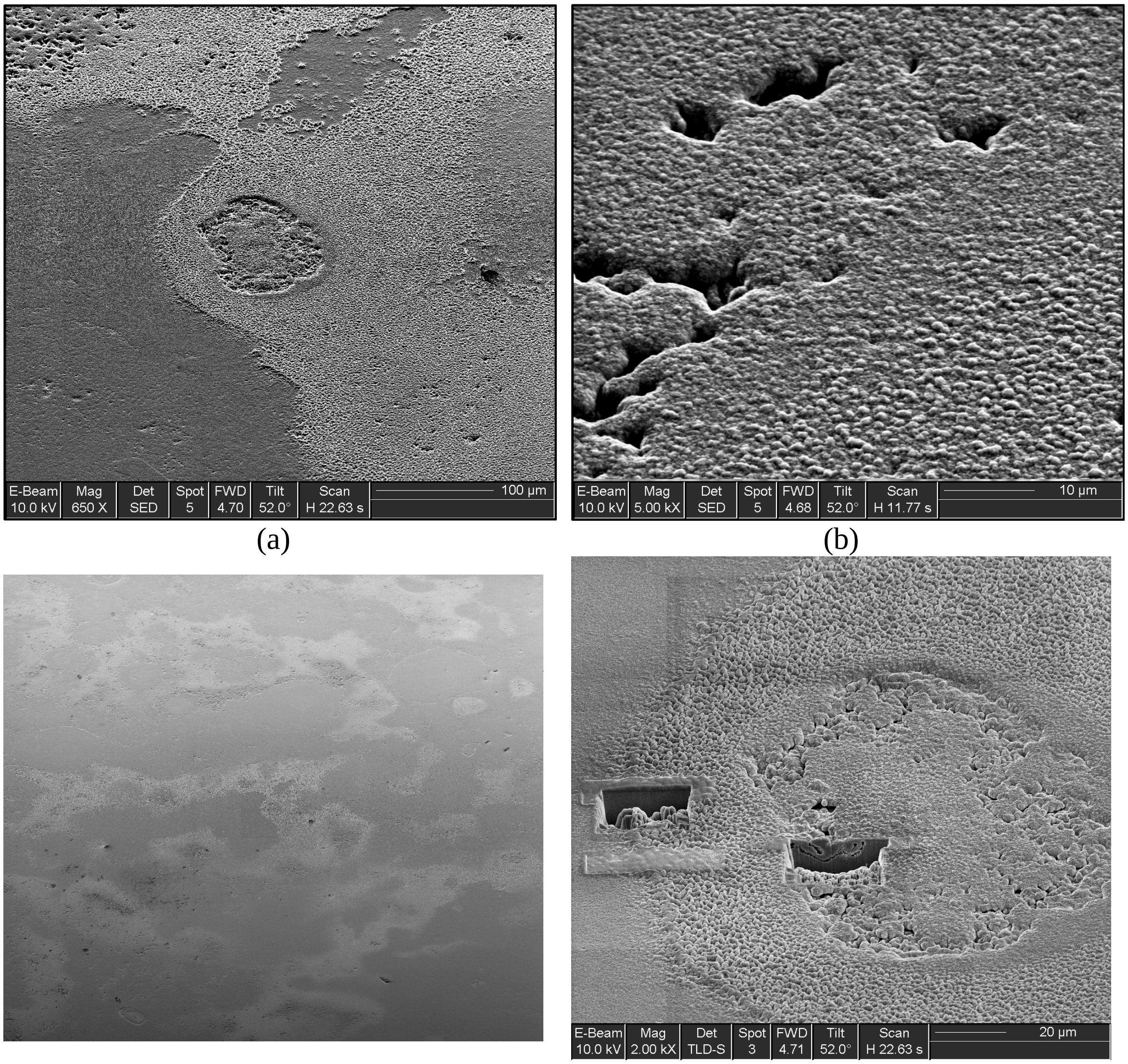

(a) (b)

(c) (d)

Fig. 4.6.2.6. SEM images of the varying surface morphology of a copper-sulfide product layer formed at high humidity (80%). The feature in the middle of (a) was examined in more detail (see next figure) using micro-sections as shown in (d). Frames (b) and (c) are magnified views of the rough area on the right of frame (a) and the smooth area on the left of frame (a) respectively.

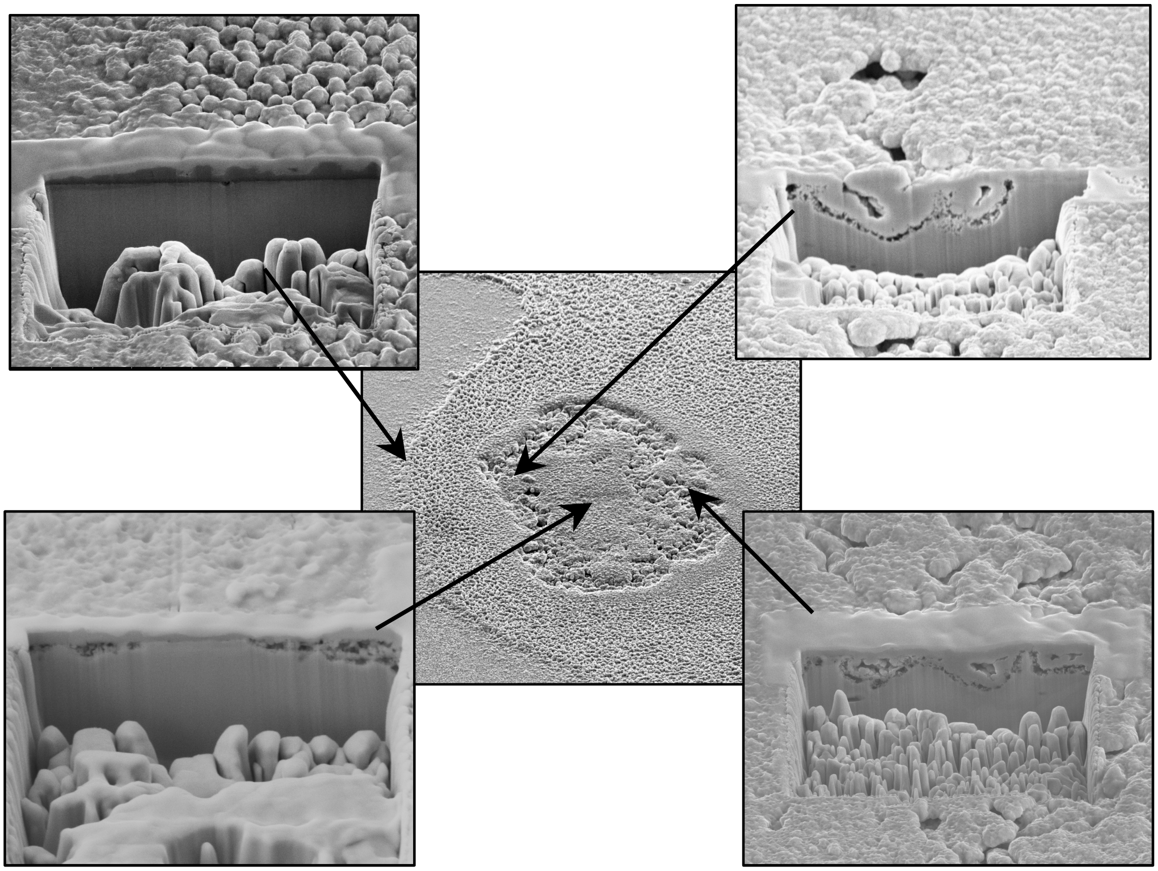

Fig. 4.6.2.7. Several SEM images taken around the feature shown in the previous figure that clearly demonstrate the complex nature of the sulfidation process at high humidity.

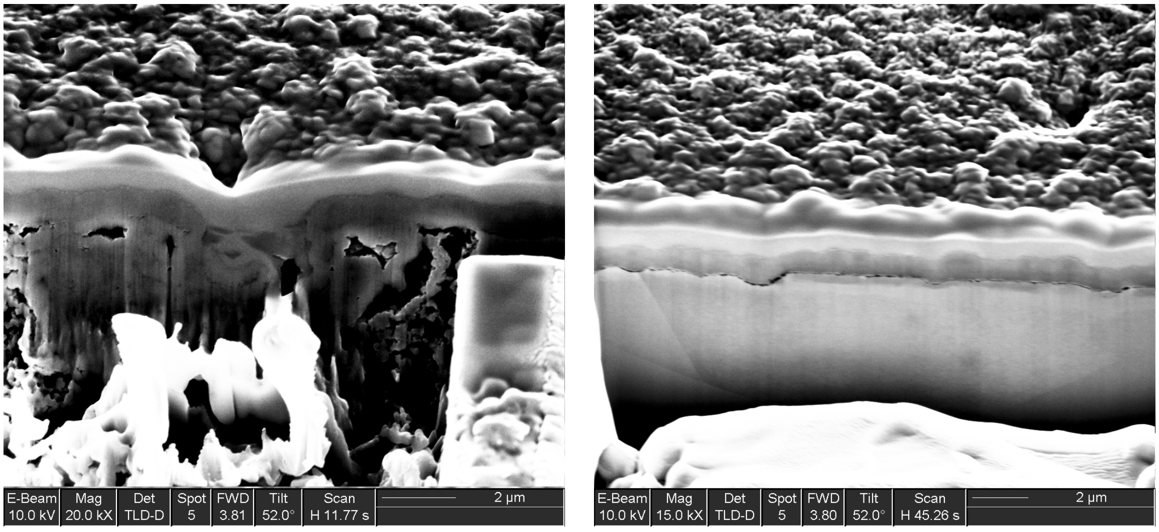

Fig. 4.6.2.8. Two additional SEM images of the Cu2S product layer grown at 80% humidity again showing the high degree of variability.

5.0 Effect of Environmental Parameters on Copper Sulfidation Kinetics

5.1 Relative Humidity and Exposure Time

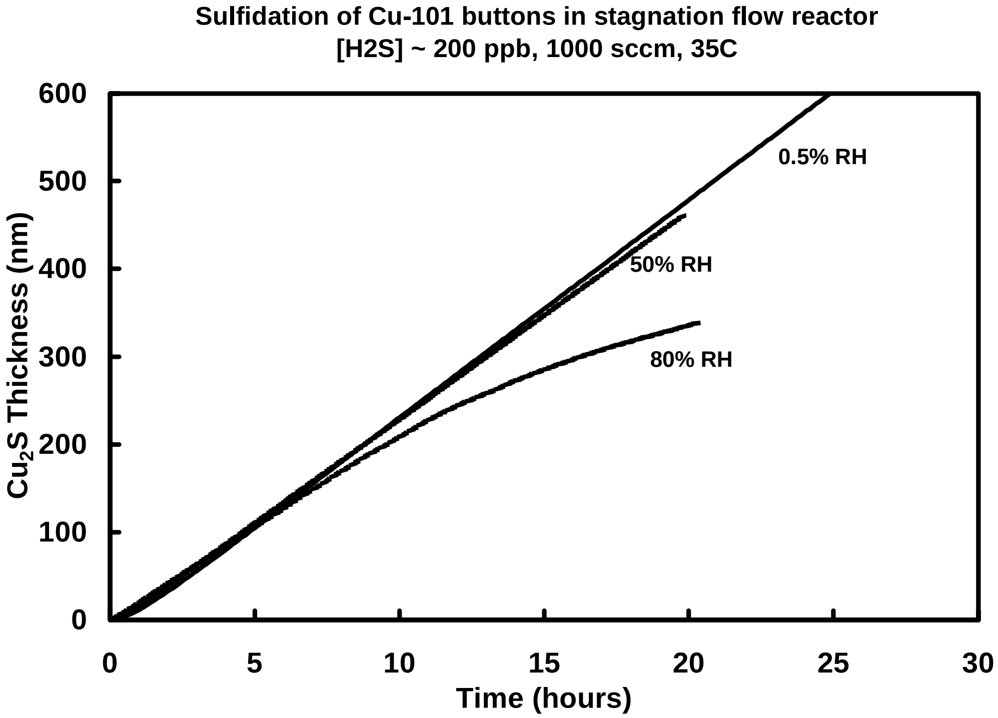

(a)

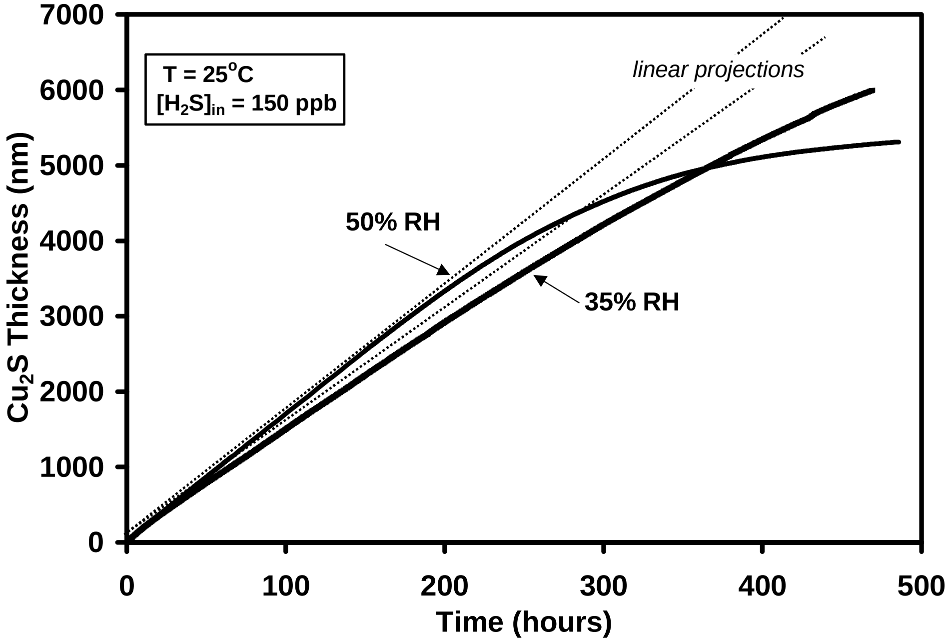

(b)

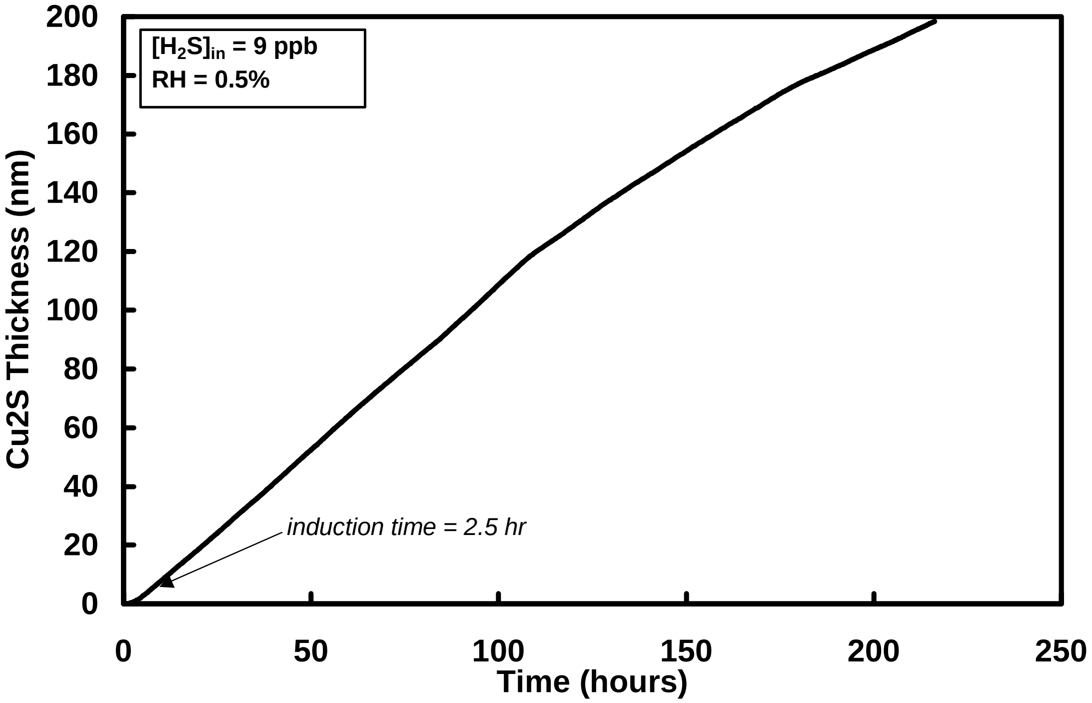

(c)

Fig. 5.1.1. The effect of two relative-humidity considerations on copper sulfidation kinetics: (a) at 35°C, and (b-c) long-term aging in a variety of mid and low humidity conditions showing the slow initiation of Stage-II at moderate and low humidity levels.

The primary effects of relative humidity on the copper sulfidation kinetics were shown previously in figure 3.4. The important observations to be gained from these figures include: (1) the Stage-I rate increased slightly with increased relative humidity, (2) there did not appear to be a critical relative humidity below which the rate significantly decreases, (3) at moderate to low humidity levels, the transition from Stage-I to Stage-II was not observed, (4) at higher humidity, the transition from Stage-I to Stage-II occurred at Cu_2S thickness levels of about 150 to 300 nm (reasonably consistent with Graedel's observed 150 nm), and (5) an initial induction period existed prior to entering Stage-I whose time was inversely proportional to the humidity. These findings appear to be relevant at other temperatures, as shown, for example, at 35°C in Figure 5.1.1a.

Findings (2) and (3) were quite unexpected. For example, electrochemical oxidation/reduction reactions that occur in thin adsorbed water layers are typically much faster than dry gas-solid reactions and a sigmoidal-type response to humidity is typical of atmospheric corrosion; and therefore, findings (2) and (3) would not be predicted from previous knowledge. At very high RH levels, the adsorbed water layer can be sufficiently thick to act like "bulk" water. As such, the expectation was that the surface reaction rate would slow significantly as the humidity decreased. Possibly, 0.5% RH still provides an adequate supply of water (H_2O concentration is still much greater than that of H_2S), but it is difficult to envision the water ever functioning as a "bulk" electrolyte at such low humidity levels. To test the validity of the third finding, a series of extended exposures were performed under a variety of conditions and concentration levels. As shown in figure 5.1.1b-c, a deviation from linearity that could mark the start of Stage-II was indeed observed in all cases. However, the transition did occur at Cu_2S thickness levels that are inconsistent with previous observations, particularly those observations for high humidity sulfidation.

5.2 H_2S and O_2 Concentration

Based on the established chemical reaction associated with this sulfidation process (equation 1), a dependency on both the concentration (partial pressure) of H_2S and O_2 would be expected. The effect of $[H_2S]$ on the Stage-I sulfidation kinetics is shown in figure 5.2.1. To determine the reaction order, the slope of each response shown in (a) and (b) is plotted in (c) as a function of the $[H_2S]$. As can be seen, a linear dependency for concentration levels up to about 125 ppb is evident. This first-order rate is consistent with the gas-phase mass transport controlling mechanism described in Section 4.2.2. However, the presence of a “saturation” effect above the 125 ppb level is not consistent with gas-phase mass transport alone. Again, this results is possible substantiation of a mixed mass transport / surface reaction controlled regime. The graph shown in figure 5.2.1d is another indicator of this relatively first-order effect. At this time, the Stage-II dependency on $[H_2S]$ cannot be determined without more sophisticated mathematical modeling. Based on the limited amount of data available at high humidity, the Stage-II response appears similar at all H_2S levels studied. This indicates that there may not be a H_2S dependency, an observation that is consistent with a Stage-II rate controlled only by the transport of Cu^+ through the Cu_2S layer, as proposed earlier by Graedel and noted in Section 4.5.

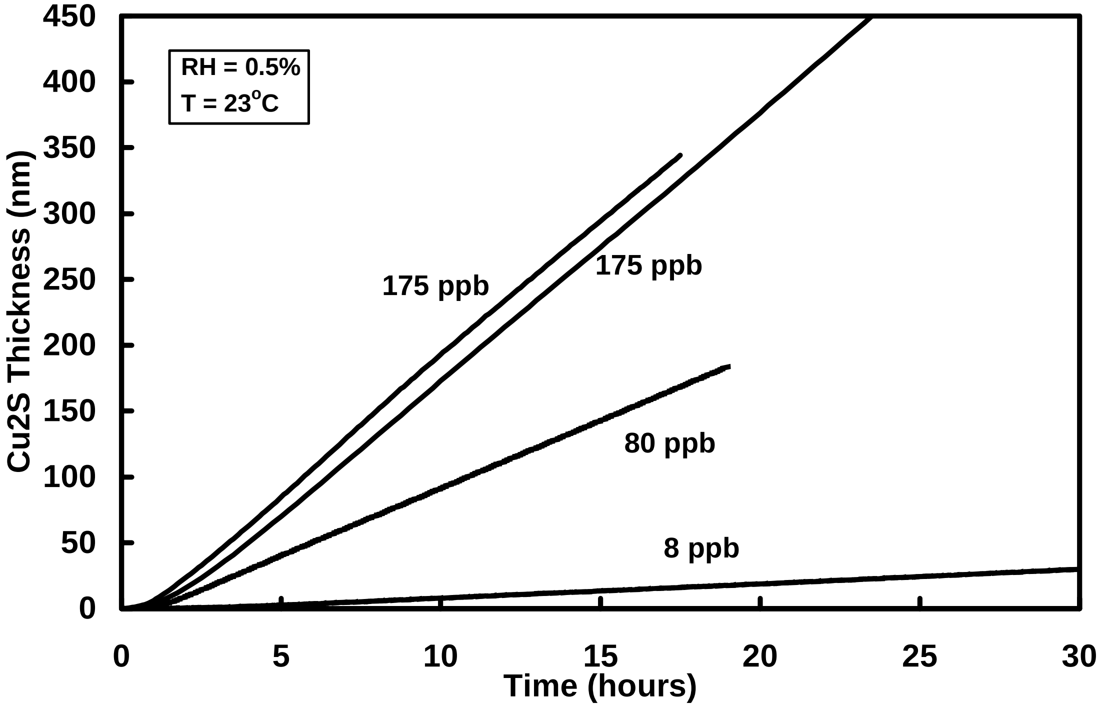

(a)

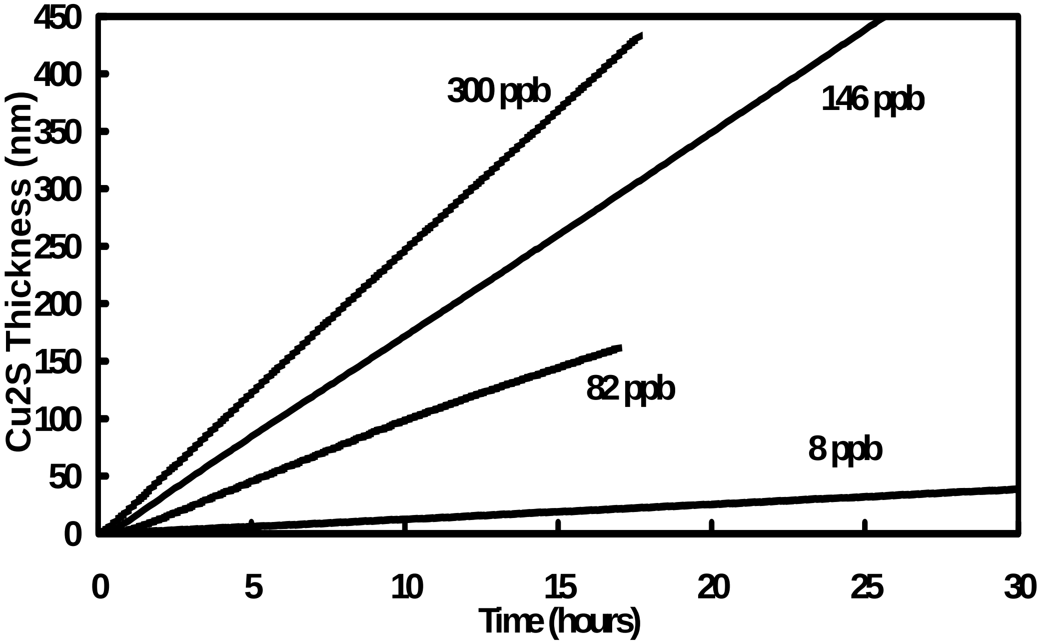
450
400
350
300
250
200
150
100
50
0
Cu2S Thickness (nm)
300 ppb
146 ppb
82 ppb
8 ppb
0
5
10
15
20
25
30
Time (hours)

(b)

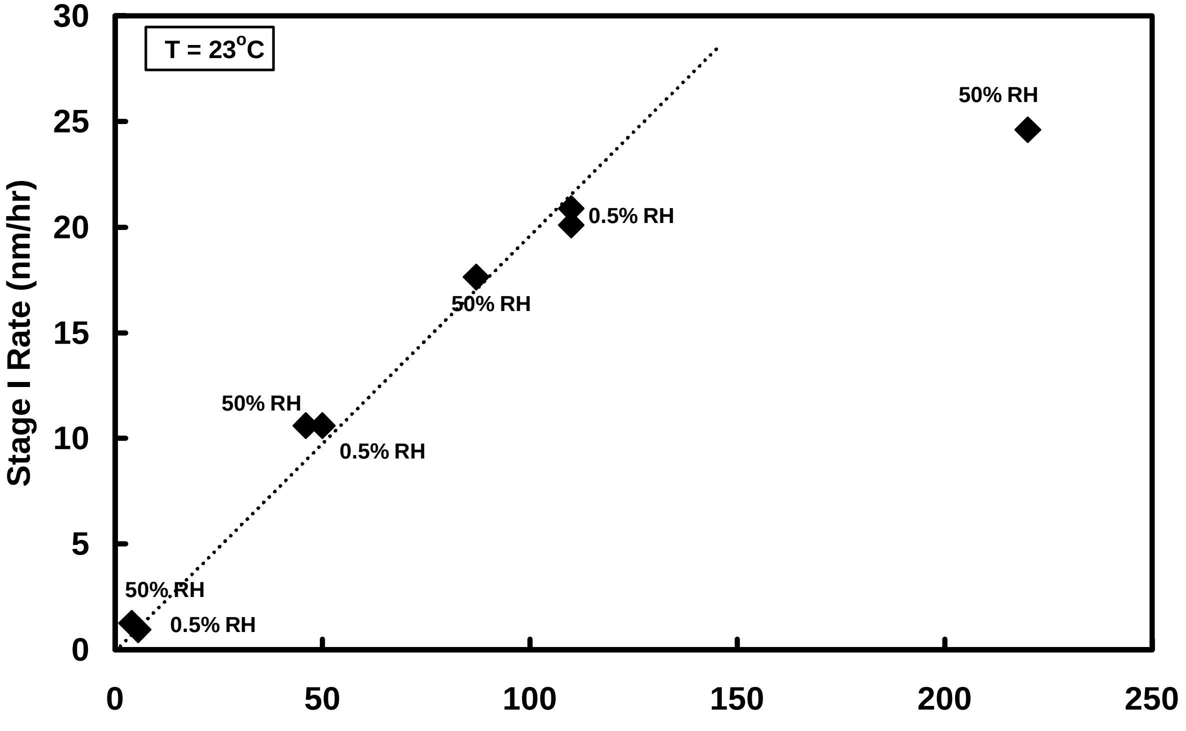
T = 23°C
30
25
20
15
10
5
0
Stage I Rate (nm/hr)
50% RH
0.5% RH
50% RH
50% RH
0.5% RH
50% RH
0.5% RH
0
50
100
150
200
250
[H2S]out (ppb)

(c)

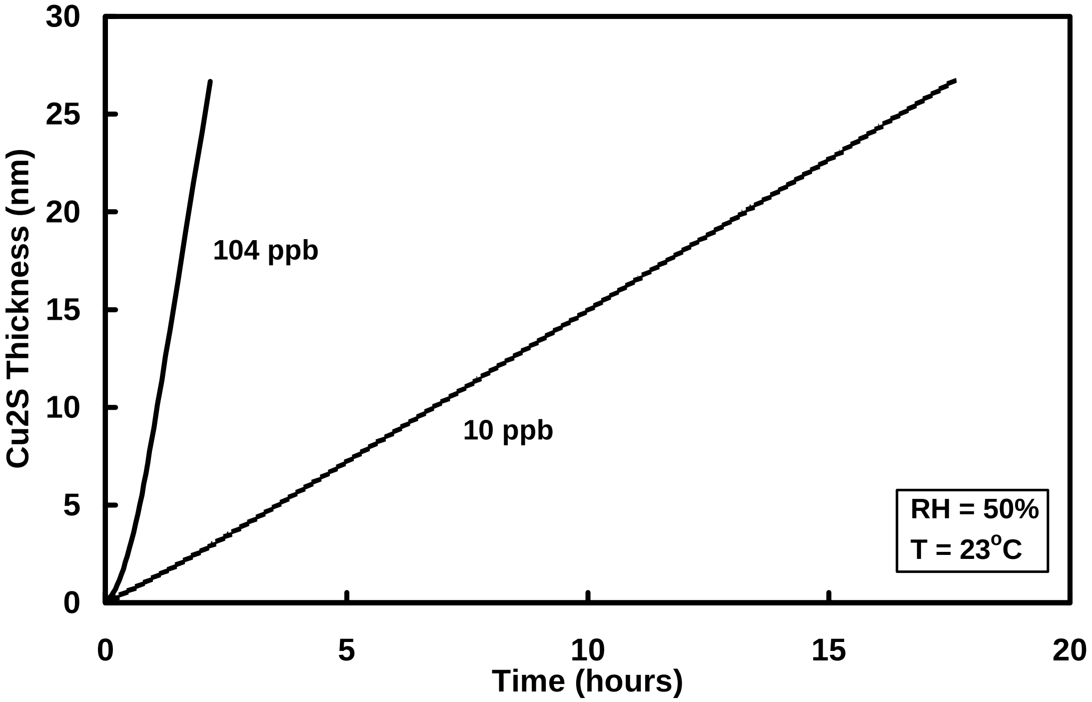

(d)

Fig. 5.2.1. Effects of [H_2S] on Stage-I growth: (a) kinetics at 0.5% RH, (b) kinetics at 50% RH, (c) rate data from frames (a) and (b) vs. outlet [H_2S] showing linear (first order) relationship up to about 125 ppb, and (d) a graphical confirmation of the first-order H_2S effect – 1/10th time to same thickess at 10x higher concentration.

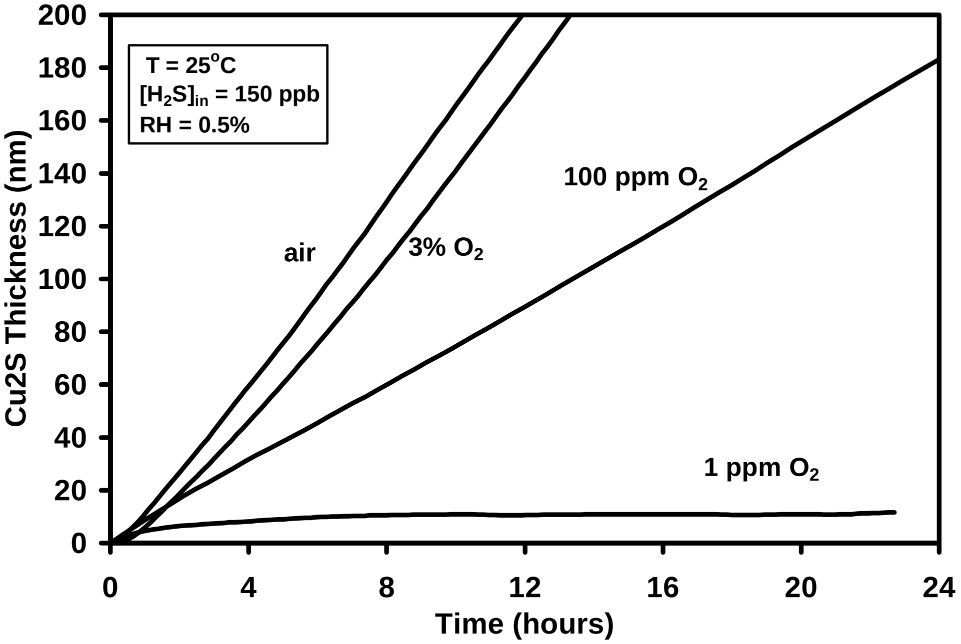

(a)

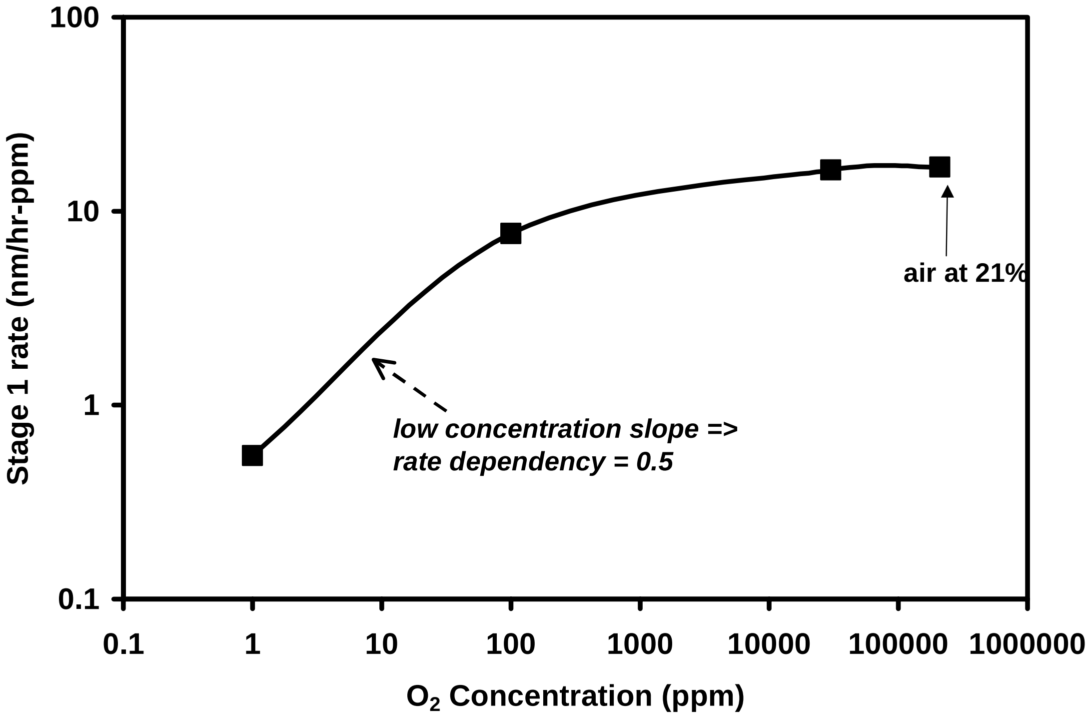

(b)

Fig. 5.2.2. The effect of oxygen concentration on the kinetics of copper sulfidation (a) and (b) the graphical relationship of rate on [O_2] showing an approximate half order dependency at levels up to about 100 ppm.

For most corrosive atmospheres encountered, the concentration of O_2 is much higher than that of H_2S and [O_2] is relatively constant. However, in order to determine the effects of O_2 on the initial sulfidation rate, sulfidation experiments were performed with greatly decreased levels of oxygen. The effect of [O_2] on the Stage-I kinetics is shown in figure 5.2.2. As shown in frame (b), the sulfidation kinetics are only affected by oxygen when the level decreases to relative low levels (< about 500-1000 ppm). Below this level, the dependency is approximately half order. At this time, we do not have sufficient insight into the process to formulate a mechanism that might explain this dependency.

5.3 Temperature

Our initial expectation was that the stage I sulfidation process would be thermally activated because mass transport and most surface reactions have positive activation energies. However, if the adsorbed layer properties are analogous to bulk solution, the quantity of H_2S and O_2 that is soluble in the adsorbed water layer probably decreases with temperature and the overall rate would correspondingly decrease. To characterize this important thermal parameter as accurately as possible, kinetic measurements were made on both wrought and e-beam evaporated thin-film samples as a function of temperature. Importantly, figure 5.3.1 is a plot that confirms that the thin-film copper sulfidizes in a manner very similar to the wrought product (based on the mass-balance calculation).

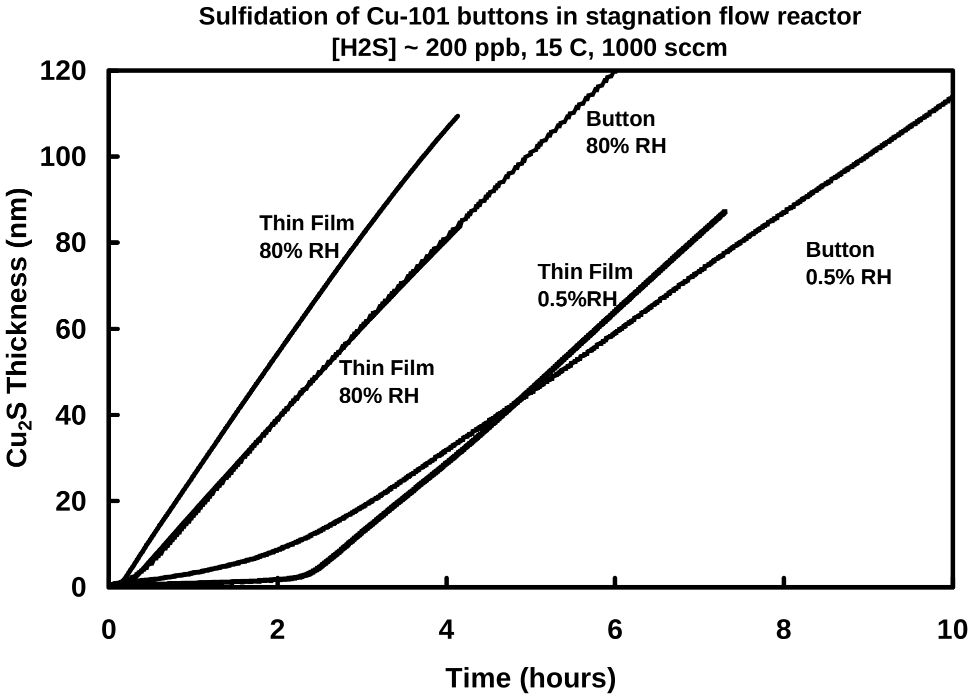

Fig. 5.3.1. Comparison of the sulfidation behavior of the e-beam evaporated copper films versus that for the wrought copper buttons.

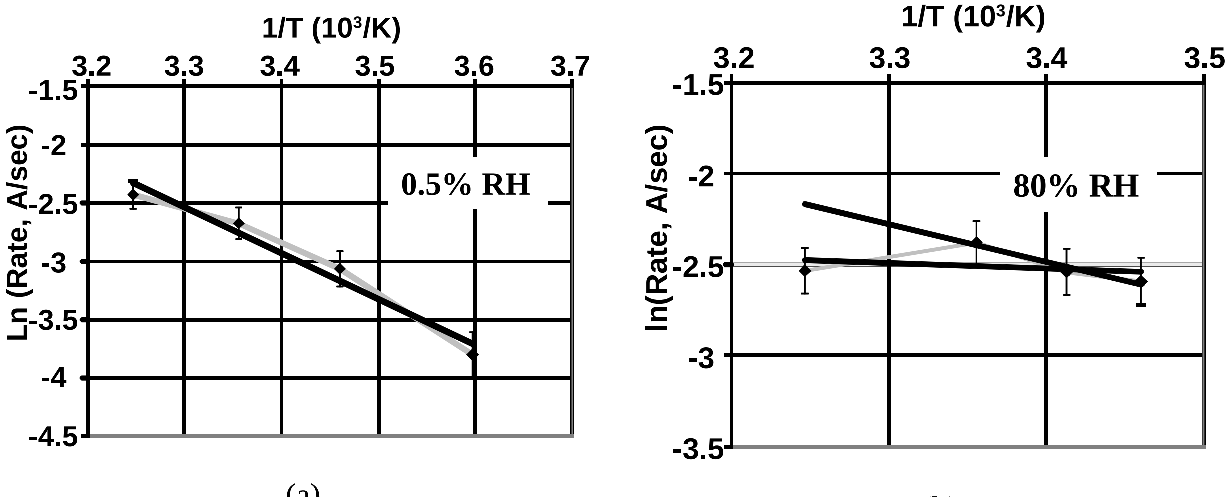

(a)

(b)

Fig. 5.3.2. Effective activation energy determined from thin-film Cu samples for stage-I growth at low (a) and high (b) RH.

The activation energies for sulfidation was measured from thin-film Cu samples for stage-I growth at low (a) and high (b) RH as shown in figure 5.3.2. These activation energies are for the overall sulfidation process and as such can reflect the energy for more than one mechanism. In fact, these effective activation energies (E_A, termed effective because they may not be for a single mechanism) give clues to different primary sulfidation mechanisms at low and high RH. E_A at low humidity was found to be greater than E_A for high humidity sulfidation, consistent with differences in growth rates at the two humidities. At 0.5% RH, E_A= 0.34 eV (7.8 kcal/mole) which is a value consistent with mixed kinetic mechanisms of a surface reaction limited process and possibly gas-phase diffusion limited supply of H_2S. A single value for E_A at high RH was more difficult to determine because it was such a small number, but bounds can be put on the size of this activation energy: $0.03\ \mathrm{eV} < E_A < 0.18\ \mathrm{eV}$ (0.6 to 4.1 kcal/mole). This range of activation energy is most consistent with gas-phase diffusion limited supply of the sulfidizing species.

The results from a portion of the measurements performed on bulk Cu-101 at two humidity levels are shown in figure 5.3.3a and c. The activation-energy plot for Stage-I at 0.5% RH and wrought copper is presented in frame (b). Including the results from the measurements with thin films, the Stage-I activation energy at low humidity can be bounded between 6-8 kcal/mole. This finding is consistent with the mixed kinetic control mechanism postulated above. That is, this value is much higher than the 2-4 kcal/mole typically associated with gas-phase diffusivity and lower than energies often associated with surface reaction. At the high 80% RH level, the activation energy for Stage-I was determined to be very low (certainly < 4 kcal/mole). One can easily see this by observing the lack of a significant difference in the initial linear portion of the responses plotted in Figure 5.3.3c. The 5^{o}C data are the exception to the lack of any trend.

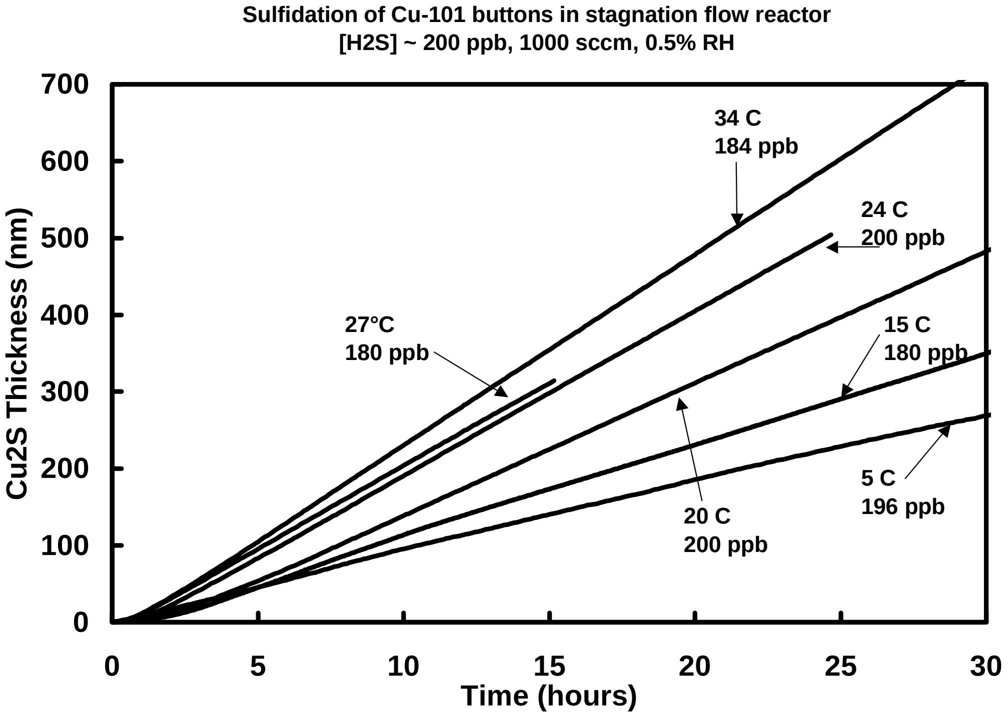

(a)

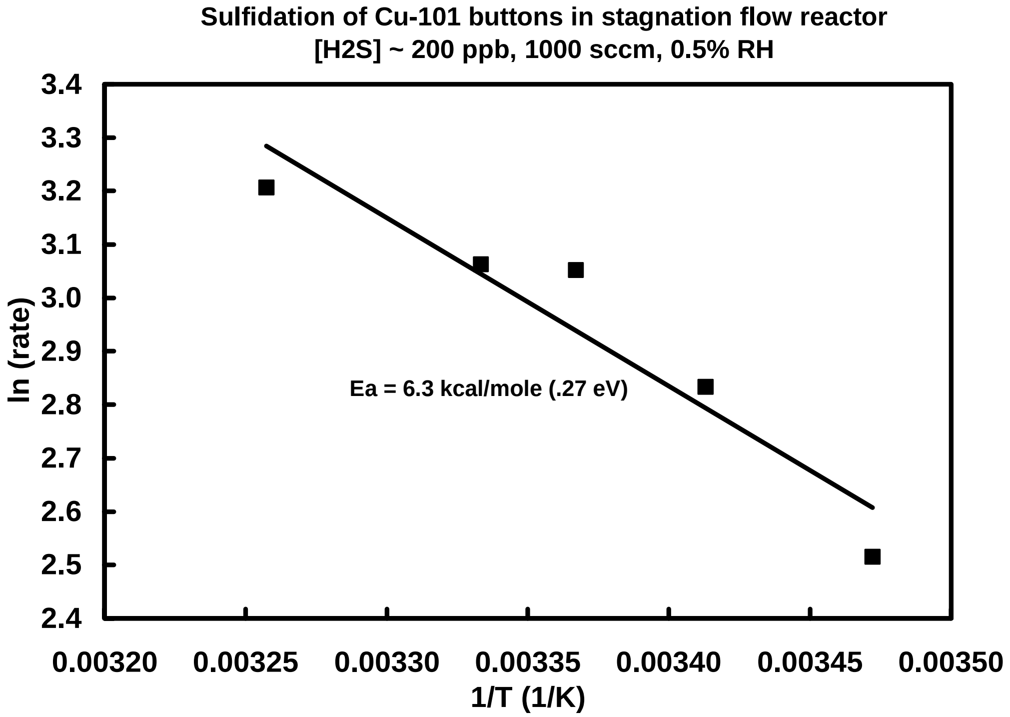

(b)

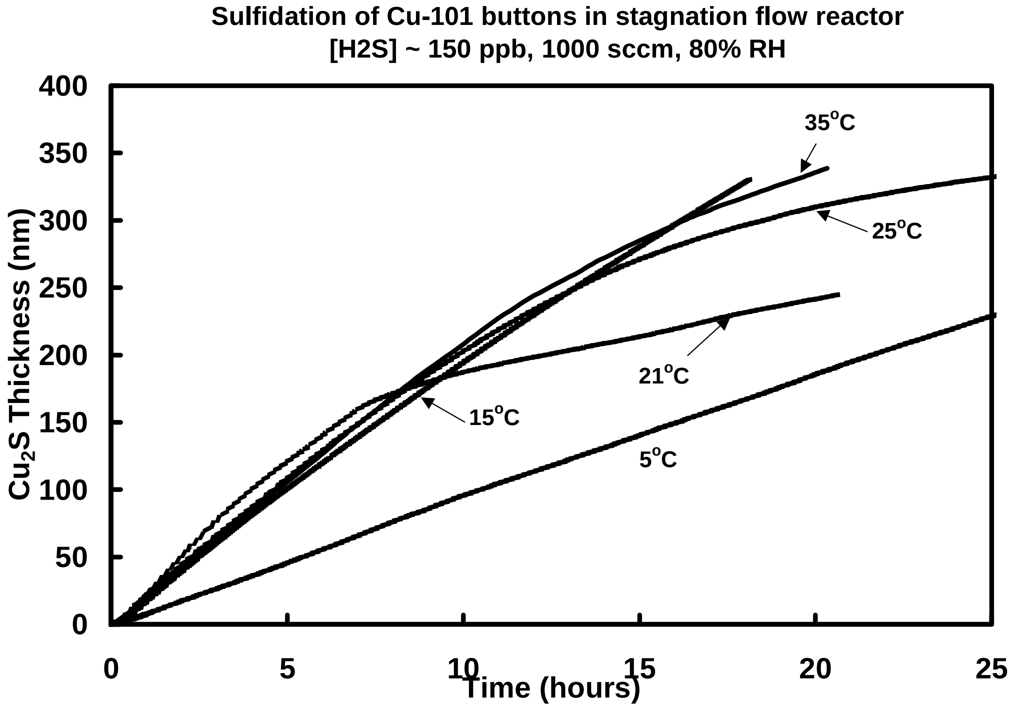

(c)

Fig. 5.3.3. The effect of temperature on copper sulfidation: (a) rate at 0.5% RH, (b) slopes from frame (a) used in a Stage-I activation energy plot, and (c) rate at 80% RH.

As stated earlier, based on the observed faster Stage-I rate at high humidity (Figure 3.4b), the expectation should be that the influence of the surface reaction should be less as the humidity increases and therefore the overall rate should become more controlled by gas-phase mass transport. As such, the lower apparent activation energy at high RH to levels more consistent with gas phase diffusion is a consistent finding. As a final note, the fidelity of the Stage-II behavior shown in Figure 5.3.3b is not adequate to enable an accurate calculation of the Stage-II activation energy. Using a simple $t^{0.5}$ dependency (basis demonstrated in the next section), our best estimate is that the Stage-II activation energy is also very low (certainly less than a few kcal/mole). A more sophisticated model for Stage-II kinetics is again needed to actually quantify this value.

5.4 Light

Many of the sulfidation experiments on bulk Cu 101 were performed under high-levels of illumination to enable the optical-interference measurements described in Section 4.2.3 to be made. It is well known that Cu_2S is light-sensitive, increasing the concentration of electron-hole pairs under illumination. Thus, a number of experiments were conducted to determine if light would effect the kinetics of sulfidation. Results are shown in figure 5.4.1 which demonstrate that the general sulfidation behavior is similar with the light on or off, but that the presence of light does accelerate the sulfidation rate. Possible explanations for the increased rate with the higher concentration of electron-hole pairs include: a modification of the various surface reactions and overall reaction rate (assuming only partial gas-phase mass transport control), or a modification of the ionic mobility (faster Cu^+ vacancy transport). More experimentation is needed to isolate these possibilities as a function of the environmental parameters.

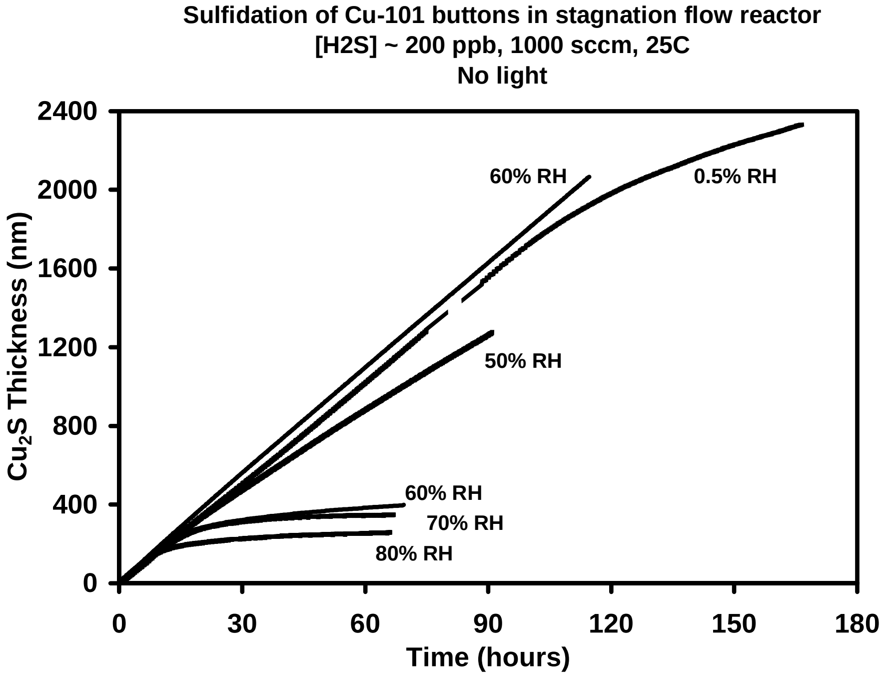

(a)

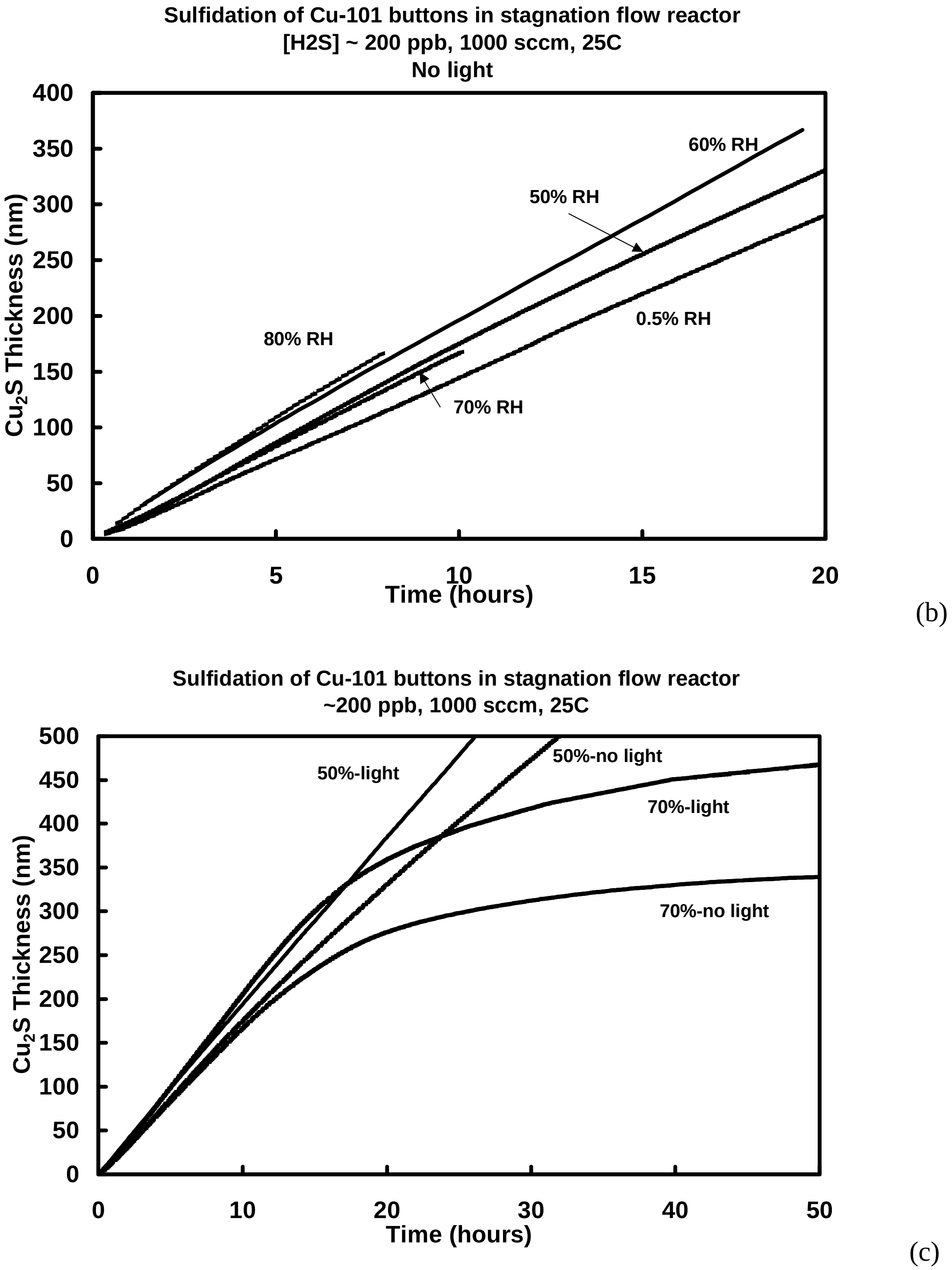

Fig. 5.4.1. The effect of relative humidity on the copper sulfidation characteristics in the absence of incident light: longer (a) and shorter-term (b) general behavior that is similar in response to that observed in the presence of light (as shown in Figure 3.4), and (c) direct comparison at two humidity levels showing how the presence of light enhances the reaction rate.

6.0 Copper Sulfidation Mechanisms and Kinetic Parameters

The significant findings from numerous kinetic sulfidation experiments include the following:

- Initial (Stage-I) kinetics are linear and first-order with respect to [H_2S] (Figures 3.4c and d). The intrinsic surface sulfidation rate must be extremely fast.
- Humidity has a dramatic effect on sulfidation growth mechanisms.
- Cu is fastest moving species in the solid state at both high and low RH, for both linear and $t^{1/2}$ kinetics.
- Stage-I rate is controlled primarily by gas phase mass transport at higher RH levels, but evidence exists of partial surface reaction control at lower RH levels. One possible explanation for this difference (supported by modeling studies) is that at high RH, the reaction rate increases because the sticking coefficient increases. The activation energy for this stage in low humidity conditions is consistent with mixed kinetic control.
- Stage II has a relatively parabolic shape and is observed only at mid to high humidity levels (Figure 3.4b).
- Stage II is indeed controlled by Cu^+ ion transport through the Cu_2S product layer (diffusivity measured with marker experiments to be ~10^{-16} cm^2/sec).

A summary of our understanding of the relevant mechanisms to be considered for sulfidation of Cu at low and high RH, and in early and later stages of sulfidation, are presented in tabular form below.

Table 6.1. Growth mechanisms

	Low RH	**High RH**
Stage I Cu_2S rate ~ t	Mixed mechanisms: surface reaction, gas-transport limited, solid-state diffusion	Gas-phase diffusion limited
Stage II Cu_2S rate ~ $t^{1/2}$	Not fully observed, yet	Solid-state diffusion limited; D_{Cu} (25 °C) ~ $1x10^{-16}$ cm^2/s.

7.0 Summary

As noted earlier by Graedel and co-workers, copper sulfidizes in two distinct stages. In this investigation, several other characteristics of the sulfidation process have been identified including the following:

- Initial (Stage-I) kinetics are linear and first-order with respect to [H_2S]. If the humidity is low, an induction period exists that is related to the nature of the native copper-oxide layer. The measured rate is affected by humidity with the rate being about 2 times higher at 80% RH than at 0.5% RH. The probable explanation for the contribution of humidity is that at high RH, an adsorbed water layer enables faster reduction of the oxide layer.
- The Stage-I rate is controlled primarily by gas phase mass transport of H_2S at higher RH levels, but evidence exists of partial surface reaction control at lower RH levels. Nevertheless, the intrinsic surface sulfidation rate must be extremely fast. The measured activation energies for this stage are consistent with mixed kinetic control (6-8 kcal/mole) at low RH and primarily gas phase transport at high RH (< 4 kcal/mole). Further, the sulfide

layer thickness could reach many micrometers at low humidities without showing a transition to square-root of time dependence (as in the high RH case).

- Stage II has a relatively parabolic shape and is observed only at mid to high humidity levels. Possibly, the presence of water affects the ionic diffusivity of the copper-sulfide product layer. That is, if the diffusivity is lower when the film is grown at high humidity (e.g., less defects present), then a transition from Stage-I to Stage-II will occur at lower film thickness levels. As determined by marker experiments, the kinetics of this stage are indeed controlled by Cu^+ ion (vacancy) transport through the Cu_2S product layer. The Cu^+ diffusivity measured with marker experiments was $\sim 10^{-16}$ cm^2/sec.
- Light was sped the sulfidation of Cu in the linear time-dependence regime. This result is consistent with increased electron-hole generation which speeds the reactions involved to form the sulfide layer. Copper sulfide is a p-type semiconductor and therefore the generation of excess electrons enhances the sulfidation rate.

Finally, the approach of using a combinatorial microlab was evaluated as a methodology to perform physics and chemistry experiments. It was found that a great deal of effort is required to develop well characterized experiments at the micrometer length scale if quantitative results are desired. Nevertheless, qualitative comparisons can be made using experiments run in parallel and then followed by more detailed studies with rather conventional approaches. An essential element necessary to performing these small length-scale experiments is the ability to fabricate the samples and the detection schemes, in-house. It is likely, that in the future, lithographic techniques to create such samples and detection schemes (microsystems) will be found as common place as the personal computer is found today. Therefore, Sandia should continue to invest in a microsystems approach for physics and chemistry experiments.

8.0 References

[1] D. A. Jones, Principles and Prevention of Corrosion, Prentice Hall, Englewood Cliffs, NJ, p. 198 (1992)
[2] M. Pourbaix, Atlas of Electrochemical Equilibria in Aqueous Solutions, NACE, Houston (1974)
[3] M. F. Ashby, Third International Conference on Strength of Metals and Alloys, vol. **2**, Cambridge, England, p. 8 (1973)
[4] M. F. Ashby, Acta Met. **20**, 887 (1972).
[5] F. W. Crossman and M. F. Ashby, Acta Met. **23**, 425 (1975).
[6] T. E. Graedel, J. P. Franey, and G. W. Kammlott, "The Corrosion of Copper by Atmospheric Sulfphurous Gases," Corrosion Science **23**, 1141 (1983).
[7] T. E. Graedel, J. P. Franey, G. J. Gualtieri, G. W. Kammlott, and D. L. Malm, "On the Mechanism of Silver and Copper Sulfidation by Atmospheric H_2S and OCS," Corrosion Science **25**, 1163 (1985).
[8] J. P. Franey, T. E. Graedel, and G. W. Kammlott, "The Sulfiding of Copper by Trace Quantities of Hydrogen Sulfide," Chapter 25 in Atmospheric Corrosion, ed. By W. H. Ailor, John Wiley and Sons, New York, p. 383 (1982)
[9] T. E. Graedel, J. P. Franey, G. W. Kammlott, J. M. Vandenberg, and P.L. Key, J. Electrochem. Soc. **134**, 1632 (1987)
[10] S. P. Sharma, J. Vac. Sci. Technol. **16**, 1557 (1979)

[11] P. B. P. Phipps and D. W. Rice, in Corrosion Chemistry, G. R. Brubaker and P. B. P. Phipps, Ed., ACS Symp. Ser. **89**. Am. Chem. Soc., p. 256-258 (1979)
[12] P. W. Brown and L. W. Masters, in Atmospheric Corrosion, W. H. Ailor, Ed., Electrochemical Society, p. 31 (1982)
[13] R.F. Service, Science **283**, 165 (1999).
[14] S.B. Zhang, S.H. Wei, A. Zunger, and H. Katayamayoshida, Phys. Rev. B **57**, 9642 (1998); see also R. W. Cahn, Nature **389**, 121 (1997).
[15] Transport of Ions in Matter (TRIM) computer code, J. F. Ziegler, IBM Research Laboratory, Yorktown Heights, New York (1992).
[16] M. Scorocco, Chem. Phys. Lett. **63**, 52 (1979).
[17] S. Poulson, P.M. Parlett, P. Stone, and M. Bowker, Surface and Interface Analysis **24**, 811 (1996).
[18] S.K. Chawla, B.I. Rickett, N. Sankarraman, and J.H. Payer, Corrosion Science **33**, 1617 (1992).
[19] I. Grozdanov and M. Najdoski, J. Sol. State. Chem. **114**, 469 (1995).
[20] K. Yaminaka, Japan. J. Appl. Phys., 28 (4), 632-637 (1989).
[21] D.E. Eastman et al., Phys Rev. **B 2**(1) (1970).
[22] Q. Dai, J. Hu, A. Freedman, G. N. Robinson and M. Salmeron, J. Phys. Chem., **100** (1), 9-11 (1996).
[23] W. G. Breiland and K. P. Killeen, J. Appl. Phys. **78**, 6726 (1995).
[24] C. R. Clayton, G. P. Halada, and S. V. Kagwade, Electrochemical Society Proceedings, Vol **98-17**, 223 (1999).
[25] N. E. Cipollini, Journal of the Electrochemical Society, **129**, 1517 (1982).
[26] L. H. Allen and E. Buhks, "Copper Electromigration in Polycrystalline Copper Sulfide, "*J. App. Physics*," 56 (2), 1984, pp. 327-335.
[27] A. Etienne, "Electrochemical Method to Measure the Copper Ionic Diffusivity in a Copper Sulfide Scale," Journal of the Electrochemical Society, **117** (7), 870-877 (1970).
[28] C. M. Rangel and T. I. C. Paiva, Surface and Coatings Tech. **83**, (1996) 194; B. D. Sartwell, P. N. Natishan, E. P. Donovan, S. N. Bunker, and A. J. Armini, Surface and Coatings Tech. **83**, 183 (1996); H. Schmidt, G. Stechmesser, J. Witte, and M. Soltani-Farshi, Corrosion Science **40**, 1533 (1998).
[29] N. G. Thompson, B. D. Lichter, B. R. Apleton, E. J. Kelly, and C. W. White, in "Ion Implantation Metallurgy", edited by C. M. Preece and J. K. Hirvonen (The Metallurgical Society of AIME, Warrendale, PA, 1980) p. 181; G. Dearnely, in "Applications of Ion Beams to Metals", edited by S. T. Picraux, E. P. EerNisse, and F. L. Vook (Plenum Press, New York, 1974) p. 63.
[30] J. F. Ziegler and J. P. Biersack, The Stopping and Range of Ions in Solids, (Pergamon, New York, 1985); see also [15].
[31] G. Kresse and J. Hafner, Phys. Rev. B **47**, 558 (1993); **49**, 14251 (1994); G. Kresse and J. Furthmüller, Comput. Mater. Sci. **6**, 15 (1996); Phys. Rev. B **54**, 11169 (1996).
[32] D. Vanderbilt, Phys. Rev. B **41**, 7892 (1990).
[33] W. Kohn and L. J. Sham, Phys. Rev. **140**, A1133 (1965); D. M. Ceperley and B. J. Alder, Phys. Rev. Lett. **45**, 566 (1980), J. P. Perdew and A. Zunger, Phys. Rev. B **23**, 5048 (1981).
[34] P.G. Shewmon, Diffusion in Solids, p.120, McGraw-Hill, New York 1963.

APPENDIX A
Analysis of the H_2S Gas Phase Copper Sulfidation Experiments

Harry K. Moffat

A1. Introduction

In a previous Sandia memorandum, we presented evidence for mass transport limited growth of the initial copper sulfide corrosion films under at least some conditions in the stagnation point flow reactor [A1]. The agreement between experiment and a numerical model based on the gas-phase mass transport limited was about 30% off. The experimental corrosion rates, as determined by in-situ reflectometry, were actually higher than the mass transport limit. Several reasons were brought forth to explain the discrepancy. The most likely reason was the possibility of inaccurate fluid boundary conditions, stemming from a possible 3D or time-transient mode of flow. SPIN calculations showed such deviations in flow inlet conditions could create such a discrepancy in the calculations as to explain the differences.

In this appendix, we analyse a new set of experiments that were carried out using the same stagnation point flow reactor. In these experiments measured the “mixing cup” concentration of gas-phase sulfur in the effluent, instead of the corrosion rate directly. By measuring the net loss of sulfur through the reactor and comparing that to a model, we may derive corrosion kinetics. Note, because the measurement is one that is based on a quantity integrated across the copper coupon, corrosion kinetics will not be as directly determinable as those from a local corrosion measurement. In particular, any dependence of the growth rate on the thickness of the corrosion product will only be determined via a deconvolution that may cause a smearing of the effect. However, we may certainly determine whether the corrosion rates observable are due to mass transport effects.

Particular emphasis in the subject set of experiments was placed on the effect of humidity on the corrosion rate. We will attempt to deconvolute the effects of mass transport within the chamber from the surface reaction rate constant, thus obtaining a better idea of the dependence of the surface reaction rate constant on the relative humidity. Lastly, suggestions for improvement in the experiment will be made.

A2. Reactor Conditions

A2.1 Reactor configuration

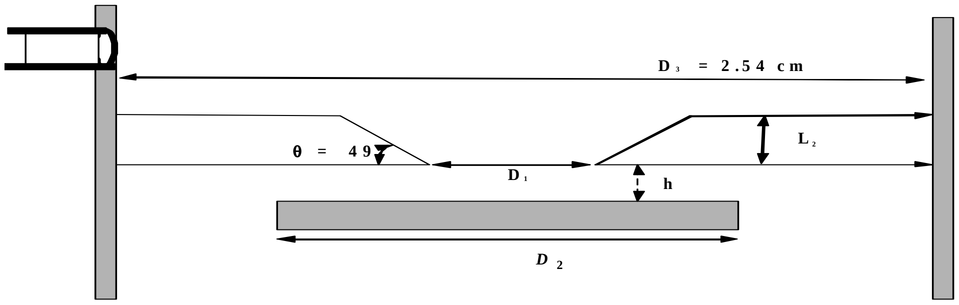

The chamber is based around an axisymmetric design as depicted in Figure A1. L_2 is equal to 0.3175 cm. D_1 is equal to 0.3175 cm also. Then, the length of the slanted section is 0.4206916 cm and the value of D_3, the diameter of the opening at the top of the hole is equal to 0.8694970 cm. The nominal starting height, *h*, of the reactor is 32/1000 inches, 0.08128 cm. However, *h* may easily be adjusted to give better performance. The bulk of thw work reported here is with $h = 0.4$ cm, though it was not measured accurately. However, as later discussed in this memo, integrated film deposition rates exhibited little dependence on *h*. D_2 is equal to 5/8 inches.

Figure A1. Dimensions of the stagnation flow reactor.

Several features of the chamber design are not axisymmetric. In our 1- and 2-D numerical analysis we will ignore these. First, the gas enters the top mixing chamber through a 3/8 inch diameter tube located halfway up one side of the chamber. Note the top of the top chamber is reserved for optical access; thus the gas entrance was not located there. The other nonaxisymmetric design is the copper coupon. The coupon was cut from a wrought bar or was a copper films that was deposited on a round silica substrate. Three screws located at the edges of the copper sample were used to set the height of reactor, *h*, accurately. Thus, the amount of area that was exposed to the corroding gases was decreased by the cross-sectional area of the posts. Actually, these screws also left “shadows” on the copper sulfide films that slightly increased the total amount of shielded area. Between 5 to 10% of the total area was shielded in this manner. The sides of the copper coupons were covered with tape and thus protected from corrosion.

A2.2 Bulk Gas Flow Rate

The base case fluid flow rate is 1 standard liter per minute (SLPM) - 1 liter of air per minute at 0 C and 1 atm. The actual flow rate may differ from this value due to calibration differences. Let's calculate the net molar flow rate, *Q*, into the reactor based on this flow rate:

$$\begin{aligned} Q &= \frac{1\ \mathrm{dm}^3}{\mathrm{min}}\left(\frac{1000\ \mathrm{cm}^3}{1\,\mathrm{dm}^3}\right)\left(\frac{1\ \mathrm{min}}{60\,\mathrm{sec}}\right)\left(\frac{1\ \mathrm{atm}}{\dfrac{82.05\,\mathrm{cm}^3\quad \mathrm{atm}}{\mathrm{mol\,K}}}\right)\left(\frac{1}{273.15\ \mathrm{K}}\right) \\ &= 7.44\times10^{-4}\quad \frac{\mathrm{mol}}{\mathrm{sec}} \end{aligned} \tag{A1}$$

Let's calculate the density of the gas, ρ, assuming that the gas is at 1 atm. and 25 C.

$$\begin{aligned} \rho &= \left(\frac{1\ \mathrm{atm}}{\dfrac{82.05\,\mathrm{cm}^3\quad \mathrm{atm}}{\mathrm{mol\,K}}}\right)\left(\frac{28\ \mathrm{gm}}{\mathrm{mol}}\right)\left(\frac{1}{298.15\ \mathrm{K}}\right) \\ &= 1.144\times10^{-3}\quad \frac{\mathrm{gm}}{\mathrm{cm}^3} \end{aligned} \tag{A2}$$

Combining the two calculations and adding in the entrance area of the inlet into the lower chamber, *A*, (D1 in the figure), we can derive the average velocity entering the lower chamber, *v*:

$$A = \frac{D_1^2}{4}\pi = 0.07917304\ \mathrm{cm}^2 \tag{A3}$$

$$\begin{aligned} v &= \frac{Q}{A}\frac{\overline{M}}{\rho} \\ &= \left(\frac{7.44\times10^{-4}\ \dfrac{\mathrm{mol}}{\mathrm{sec}}}{0.07917304\ \mathrm{cm}^2}\right)\left(\frac{28\ \dfrac{\mathrm{gm}}{\mathrm{mol}}}{1.144\times10^{-3}\ \dfrac{\mathrm{gm}}{\mathrm{cm}^3}}\right) \\ &= 230.0\ \frac{\mathrm{cm}}{\mathrm{sec}} \end{aligned} \tag{A4}$$

This velocity forms the basis of the 1D SPIN model for the corrosion process.

For purposes of the numerical model, we need to calculate the velocity at the top of the domain, at a diameter of D_3.

$$A = \frac{D_3^2}{4}\pi = 5.067074\ \text{cm}^2 \tag{A5}$$

$$\begin{aligned} v &= \frac{Q}{A}\frac{\overline{M}}{\rho} \\ &= \left(\frac{7.44\times 10^{-4}\ \frac{\text{mol}}{\text{sec}}}{5.067074\ \text{cm}^2}\right)\left(\frac{28\ \frac{\text{gm}}{\text{mol}}}{1.144\times 10^{-3}\ \frac{\text{gm}}{\text{cm}^3}}\right) \\ &= 3.59503\ \frac{\text{cm}}{\text{sec}} \end{aligned} \tag{A6}$$

A2.3 Reactant Flows

The composition of H_2S in the inlet was 200 ppb under baseline experimental conditions. Thus, the mole fraction of H_2S in the inlet stream is equal to $X_{\text{H}_2\text{S}} = 2.0\times 10^{-7}$. Thus, the total flow rate of H_2S, $Q_{\text{H}_2\text{S}}$, is equal to

$$Q_{\text{H}_2\text{S}} = Q\times X_{\text{H}_2\text{S}} = 1.488\times 10^{-10}\ \frac{\text{mol}}{\text{sec}} \tag{A7}$$

The baseline composition of water was set to 80% relative humidity at 25 C. We will assume, then, that water is in excess with respect to H_2S. A calculation of the water mole fraction may be done, if necessary. In these initial calculations, which assume mass transport limited growth of H_2S to the surface, we have ignored the presence of water. 80% relative humidity air contains roughly 6% water; this amount of water is expected to have a negligible effect (~3%?) on the transport properties of H_2S. In the future, we may extend the analysis to include water transport in the gas if warranted using a 1D SPIN model, with appropriate boundary conditions established from a 2D axisymmetric analysis — more on this later.

Now, let's calculate the total moles of Sulfur supplied to the reactor during the course of a two hour experiment.

$$\text{mol S available} = Q_{\text{H}_2\text{S}}(2\ \text{hr}) = 1.07\times 10^{-6}\quad \text{mol S} \tag{A8}$$

This provides a maximum on the total amount of Cu_2S that may be grown during the experiment in the apparatus. Kinetic and mass transport related restraints may limit the actual amount of Cu_2S grown below this theoretical maximum.

A2.4 Maximum Film Growth Rate Under Base Conditions

The density of Cu_2S is equal to 5.5 - 5.8 gm cm^3 [A2]. Let’s use 5.6 gm cm^3 here. With molecular weights of 63.5 gm mol^{-1} and 32.066 gm mol^{-1} for Cu and S, respectively, the molecular weight of Cu_2S is equal to 159 gm $(\mathrm{mol}\ Cu_2S)^{-1}$.

Let’s do a rough calculation on the maximum growth rate of copper sulfide that could be deposited during this time using the nominal 5/8 inch substrate. Then, we will calculate the growth rate assuming that all sulfur molecules are incorporated into the growing product layer.

$$\begin{aligned}\frac{\text{Deposited mol S}}{\text{A}} &= \frac{\left(1.488\times10^{-10}\ \dfrac{\text{mol S}}{\text{sec}}\right)}{\left(1.979\ \text{cm}^2\right)}\left(\frac{1\ \text{mol Cu}_2\text{S}}{1\ \text{mol S}}\right)\left(\frac{1\ \text{cm}^3}{5.6\ \text{gm}}\right)\left(\frac{10^7\ \text{nm}}{1\ \text{cm}}\right)\left(\frac{159\ \text{cm}}{1\ \text{mol Cu}_2\text{S}}\right) \\ &= 76.8\ \frac{\text{nm}}{\text{hr}}\end{aligned} \quad \text{(A9)}$$

A2.5 Calculation of Dimensionless Numbers

Let’s calculate the appropriate Reynolds number, *Re*, for the stagnation point flow reactor. From the CRC [A2], the viscosity of air, μ, at 300 K is equal to $18.6(7.0)\times10^{-6}\ \text{Pa s} = 18.6\times10^{-5}\ \text{gm cm}^{-1}\ \text{s}^{-1}$. Plugging this number into the expression for the Reynolds number in a stagnation point flow geometry and using the height of the main chamber as the characteristic dimension, we obtain:

$$\begin{aligned}\text{Re} &= \frac{\rho v h}{\mu} \\ &= \frac{\left(1.16\times10^{-3}\ \dfrac{\text{gm}}{\text{cm}^3}\right)\left(229\ \dfrac{\text{cm}}{\text{s}}\right)\left(0.08128\ \text{cm}\right)}{18.6\times10^{-5}\ \dfrac{\text{gm}}{\text{cm s}}}\ . \\ &= 116\end{aligned} \quad \text{(A10)}$$

Thus, the flow in the reactor is inertially dominant. Note, while *Re* is above one, it’s still very low compared to the value necessary to support turbulent flow (~5000). Thus, the flow will be in the laminar regime, and we should carry out a boundary layer analysis based on the assumption of laminar flow. Note, if we had used the diameter of the nozzle, 0.3125 cm, as the characteristic dimension in the Reynolds number calculation, we would have reached the same conclusions concerning the regime of flow.

The Schmidt number for mass transport of H_2S through air may also be calculated. Assuming that the (Lennard Jones) LJ collision depth is 3.6 A and LJ intermolecular force constant is 301 K, then the binary diffusion coefficient of H_2S in N_2 may be calculated using standard gas-phase formulas to be equal to 0.166 $\mathrm{cm}^2\ \mathrm{s}^{-1}$ at 1 atm. and 300 K. When combined with a value for the kinematic viscosity of air at 25 C of $\upsilon = 0.166\ \mathrm{cm}^2\ \mathrm{s}^{-1}$ (derived in the next section), the following value for the Schmidt number is obtained.

$$Sc = \frac{\upsilon}{D_{\mathrm{H_2S,N_2}}} = 0.96 \tag{A11}$$

In the analysis below we will assume that $Sc = 1$. Let's calculate a boundary layer thickness for the stagnation point flow reactor

$$\delta = \sqrt{\frac{\upsilon h}{v}} = 0.007544\ \mathrm{cm}. \tag{A12}$$

Thus, the nominal height of the reactor is a factor of 10 larger than the boundary layer thickness. We have plenty of room to reduce the height of the reactor, if it turns out that is the correct direction to go.

A2.6 Viability of SPIN Calculations

SPIN is a computer program that employs the 1D von-Karmon similarity solution approximation to solve for the heat, mass, and momentum transfer in stagnation point flow and rotating disk flow geometries. When first starting to study the stagnation point flow corrosion reactor, a SPIN calculation was carried out. Only momentum and mass transfer in the lower chamber was considered. One atmosphere was assumed. The velocity a distance *h* away from the surface was 228 cm sec^{-1}. *h* is equal to 0.08128 cm. The mole fraction of H_2S was equal to 1.0×10^{-7}. A simple sticking coefficient mechanism at the surface was used, where H_2S goes to $H_2(g) + Cu_2S$. Transport of copper through the bulk product layer was assumed to be infinitely fast. Initially, the radial velocity was set to zero at the top of the domain.

The numerical result was a net deposition rate is equal to 69.73 nm hr^{-1}. A preliminary experimental result obtained in 1999 from Bill Breiland's in situ reflectance monitor was 63 nm hr^{-1}. However, the experimental deposition was visually non-radially non-uniform. A donut pattern was produced with a deposition rate that was highest at roughly the diameter of the hole of the nozzle. This observation was the prime motivator for the 2D results presented in the rest of the memo. The boundary layer thickness (defined as a 20% drop in the H_2S free stream concentration) as determined by SPIN was equal to 0.0106 cm, roughly agreeing with Eqn. 12.

Note, there is an inviscid component to the flow solution (but not the heat or mass transfer solution) extending far out into the gas, that actually provides uncertainty to the SPIN flow boundary conditions at the top of the domain. It turns out, as will be shown below, that the assumptions employed above of a zero radial velocity are not validated by the 2D axisymmetric model. The flow boundary condition has a large impact on SPIN's corrosion rate prediction, also. Thus, the agreement with experiment demonstrated by the SPIN calculations was merely fortuitous. Our first SPIN calculations, where a zero radial velocity at the top of the domain was assumed, did not take into account of the true Euler solution to the stagnation point flow problem far from the susceptor. This solution, in radial coordinates is given by

$$v_r = \frac{a\,r}{2}, \qquad v_z = -a\,z \text{ , where a is an adjustable constant.} \tag{A13}$$

The value of *a* is important, but SPIN can not a priori predict the value of *a*. One reasonable value for *a* would be that value that yields a matching condition with respect to v_z at the top of the SPIN domain, i.e., the nozzle exit. Adjusting *a* to match the top boundary conditions of the SPIN calculation.

$$a = \left(\frac{228\ \frac{\text{cm}}{\text{s}}}{0.08128\ \text{cm}} \right) = 2805\ \text{s}^{-1} \tag{A14}$$

If SPIN's input file were adjusted to this value of *a*, the deposition rate would be reduced to 32 nm hr^{-1}. Thus, *a* is important and unknown. A 2D or higher analysis is needed to shed light on the what the best boundary conditions is for a SPIN calculation. This result is worthwhile to remember, for it may be beneficial to use SPIN, calibrated for a particular flow rate in a parametric kinetics mechanism analysis.

A3. MPSalsa Analysis

While the SPIN calculation was very successful, we seek a better solution that will yield information concerning the radial distributions and the uncertainties in flow boundary conditions for SPIN. We will assume a 2D axisymmetry. However, this assumption should be questioned. I initially used MPSalsa, because it employs surface chemkin to calculate the growth rates at the opper coupon interface, and MPSalsa was the shortest route to a completed analysis [A3].

A3.1 Setup of the Mesh and Problem

Figure A2 contains a picture of the entire mesh. Note, the requirements on the mesh are really quite stringent, in that there needs to be a lot of refinement at the copper surface to resolve the boundary layer (0.01 cm). At the same time the mesh should be graded fairly uniformly, and provide sufficient coverage for the rest of the domain to resolve recirculations produced by the inertially-dominated flow. Figure A3 provides a blowup of the mesh near the deposition zone, showing that the boundary layer is resolved.

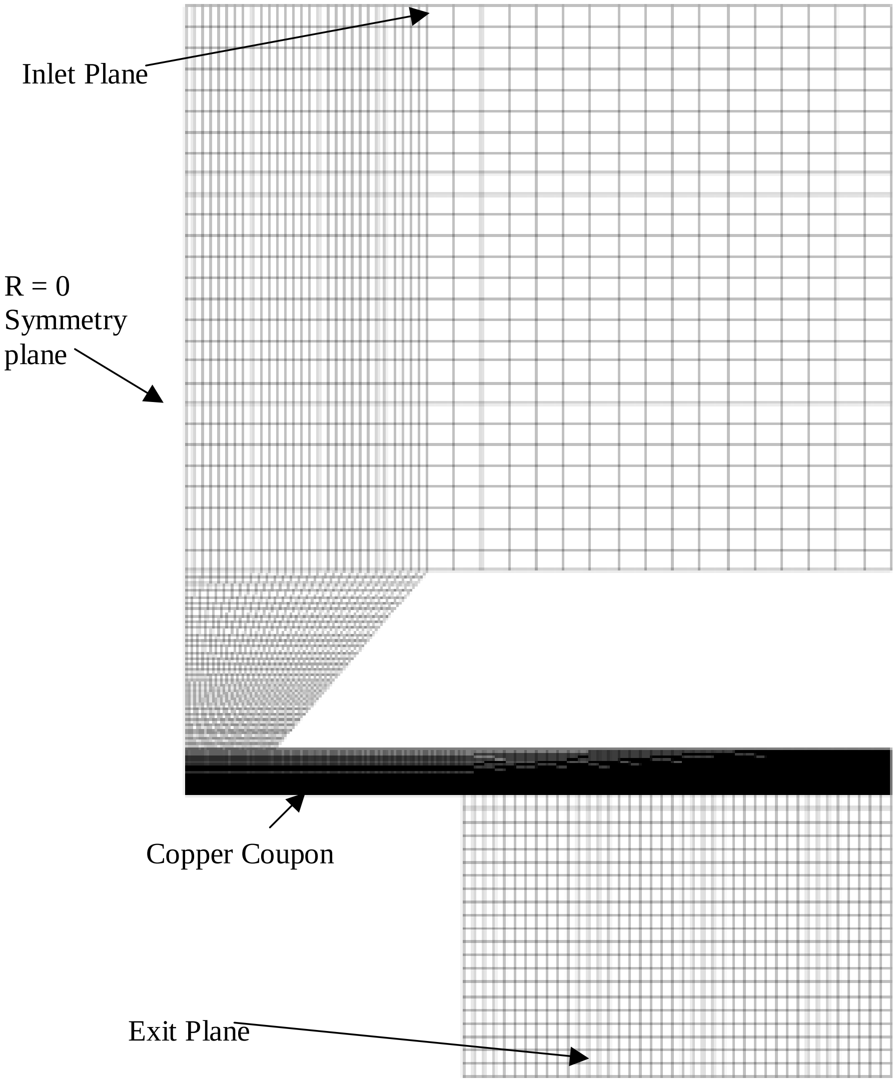

Figure A2. Full mesh for the 0.813 height calculation.

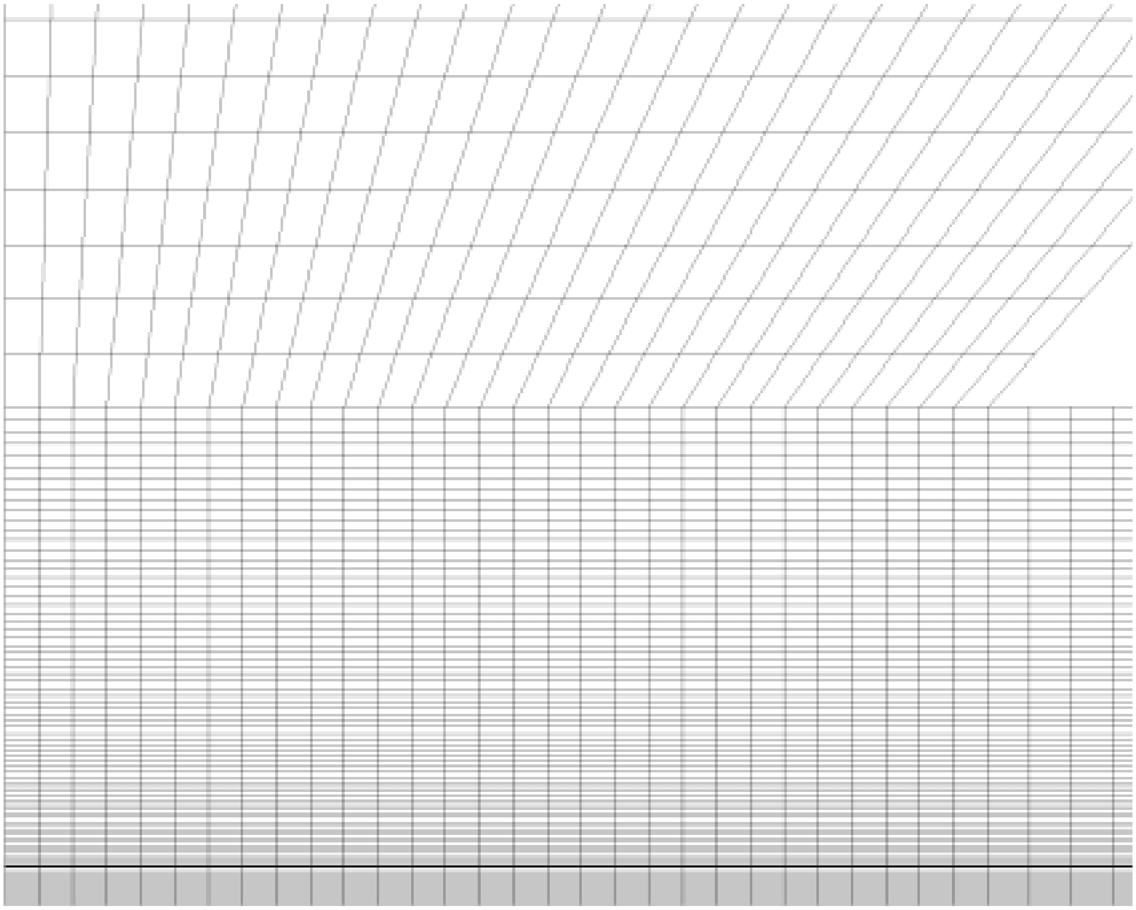

Figure A3. Blow up of the mesh near r = 0 at the copper coupon.

Details concerning the inlet and the swirling flow in the top region were ignored by setting the inlet plane a fairly large distance away from the nozzle. The inlet gases enter at the top of the chamber via a uniform velocity. This velocity is very slow due to the large diameter of the top of the chamber. The gas velocity increases considerably through the nozzle, which is directed at the deposition surface. The boundary layer is reduced by this jetting action leading to decreased mass transport resistance. The flow than slows down as it expands radially. It goes around a corner and then exits at the bottom of the reactor. Exit boundary conditions are very important for numerical robustness issues. Initially, I used this geometry in Figure A2, because it resembled the experimental setup. However, numerically it lead to some convergence problems, due to the fact that a large recirculation zone appeared in the exit region. Along part of the exit boundary (using zero traction boundary conditions on the flow), it turned out that the flow entered the domain, while along the outer part the flow left the domain. This type of behavior causes extreme problems when formulating the exit boundary conditions for an advection-diffusion equation that is added to the solution. It would also cause needless complications when trying to integrate the flux of H_2S along the exit boundary. Therefore, in order to avoid these unnecessary complications, I changed the exit region shape to that in Figures A4 and A5 without changing the mesh topology.

At the top of the domain, the inlet velocity, v_3, is set to the total flow rate divided by the chamber area at that point,

$$A_3 = \frac{D_3^2}{4}\pi = 5.0671\,\mathrm{cm}^2 \tag{A15}$$

$$\begin{aligned} v_3 &= \frac{Q}{A}\frac{M}{\rho} \\ &= \left(\frac{7.44\times10^{-4}\ \frac{\mathrm{mol}}{\mathrm{sec}}}{5.0671\,\mathrm{cm}^2} \right) \left(\frac{28\ \frac{\mathrm{gm}}{\mathrm{mol}}}{1.15\times10^{-3}\ \frac{\mathrm{gm}}{\mathrm{cm}^3}} \right) \\ &= 3.57498\ \frac{\mathrm{cm}}{\mathrm{sec}} \end{aligned} \tag{A16}$$

These calculations were all carried out in two steps. First, the flow solution was calculated, using numerical damping. The flow solution was then used as an initial guess to a coupled flow mass transfer calculation. This calculation, which was extremely large in terms of its memory requirements for solution (910 megabytes), converged rapidly due to the fact that the mass transport system was in the dilute limit, and therefore the nonlinearity were minor.

A3.2 Description of MPSalsa Results

Figure A4 contains a false color image of the H_2S concentration for the base case height of 0.812 mm. Figure A5 contains a false color image of the radial velocity for the same case. There is a flow separation point at the nozzle tip, as expected. Flow reattachment occurs towards the end of the copper coupon.

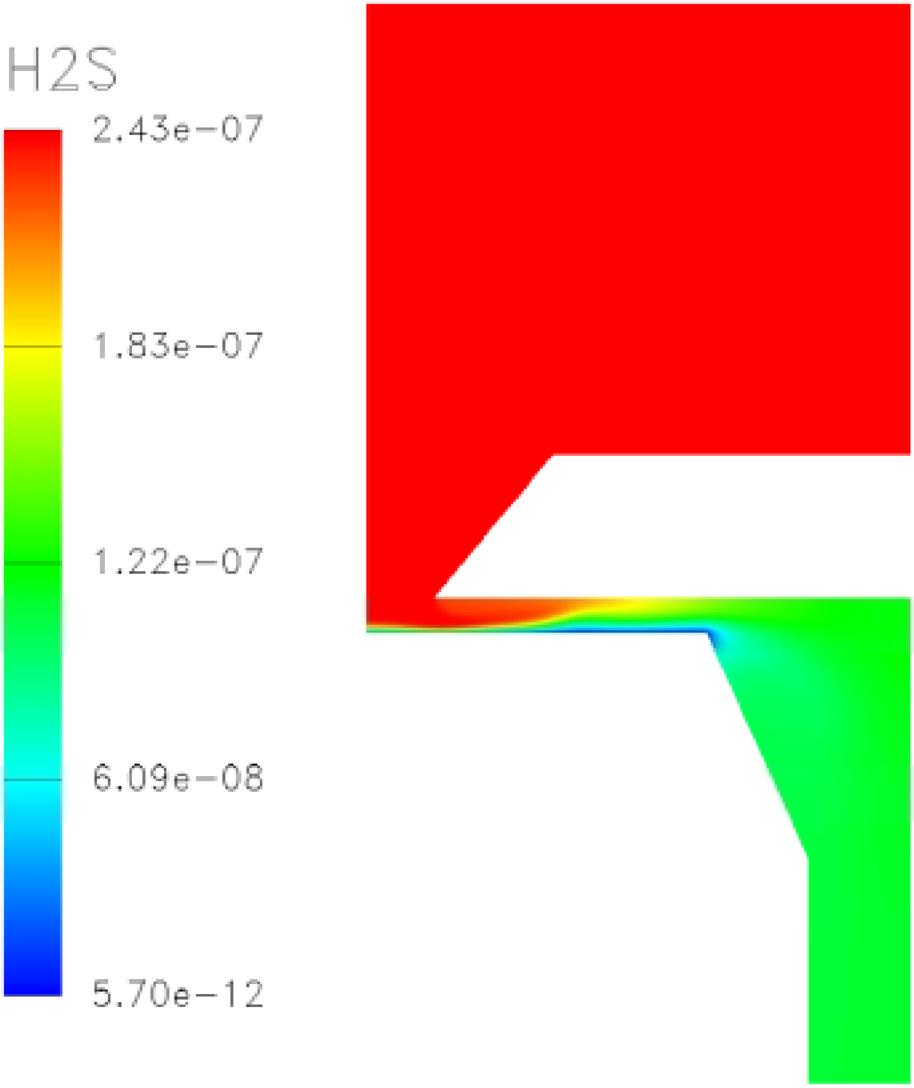

Figure A4. H_2S mole fractions for 0.812 mm case.

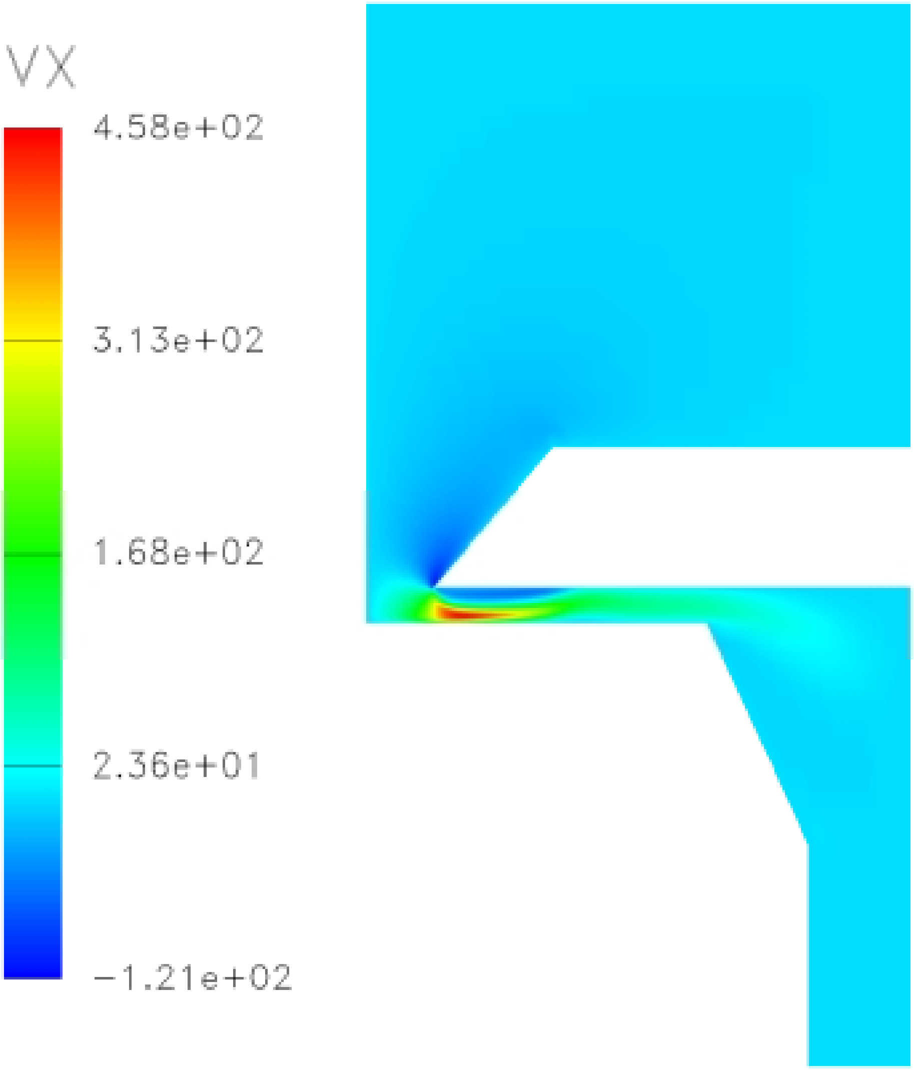

Figure A5. Radial velocities for base case, 1 slpm, height = 0.813 mm.

Thus, a fairly benign recirculation cell occurs on the lee side of the nozzle tip. This recirculation cell gets energetic if the inlet velocity is increased (calculation not shown).The numerically determined growth rates at the edge of the copper coupon oscillated wildly, due to the lack of resolution and the fact that the deposition rate abruptly drops to zero on the other side of the corner. These are artifacts of the numerical solution and can be safely ignored. The exit region exhibits a large lazy recirculation that can also be ignored, but perhaps leads to problems in solution convergence. (I did have some problems in converging to the flow solution. I had to use the numerical damping algorithm to converge to the flow solution. Also supg stabilization was necessary for both the nonlinear and linear subproblems.

In Figure A6, the dependence of the corrosion rate as a function of radius and the adjustable parameter *h* is shown. The modeling work in our previous memo indicated that the magnitude of the doughnut-shaped sulfidation profile could be reduced by going to a 4 x base height of 3.12 mm. At this height the jet, the flow has enough time to adjust to the bending of its streamlines as it goes around the corner, without reducing the boundary layer height. Note, there is practically no dependence of the corrosion rate at the centerline with height! The reason for this is that the height parameter doesn't affect the flow behavior near the centerline for these flow rates. The flow orientates itself at the centerline according to the inviscid flow solution, relatively independently of the height parameter. Note, at higher inlet velocities, this actually turns out not to be true due to enhanced jetting towards the centerline caused by the fluted design of the nozzle (calculation done but not shown).

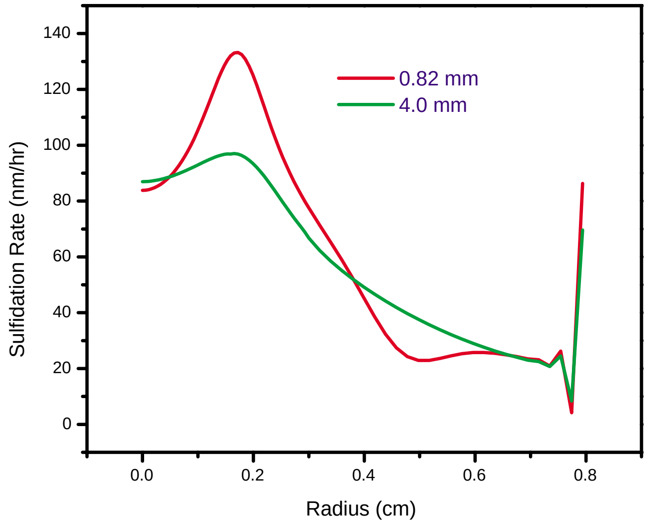

Figure A6. Corrosion rate as a function of radius for two reactor heights.

Figure A6 also shows a an initial experimentally determined corrosion rate for an RH of 80%, the highest corrosion rate observed, assuming a uniform sulfidation rate.

A3.3 Integrated Fluxes over the Inlet and Exit Regions

The subroutine `f_ss_centroid()` in MPSalsa was used to calculate integrated quantities over side sets. `f_ss_centroid()` will write out one entry for the value of a quantity at the centroid of each element on a side set. One of the entries can be the surface area of the element. Therefore, we can develop expressions for the flux of total mass and flux of H_2S crossing a boundary oriented in the axial direction and specified by the inner radius, R_1, and outer radius, R_2, by summing up the individual element contributions.

$$MassFlux = \int_{R_1}^{R_2} 2\pi \, \rho \, \boldsymbol{u} \bullet \boldsymbol{n} \, r \, dr = \sum_{i=1}^{N} A_i \, \rho_i \, v_{z,i} \tag{A17}$$

$$\mathrm{H_2S}\ \ Flux = \int_{R_1}^{R_2} 2\pi \, \rho \, \boldsymbol{u} \bullet \boldsymbol{n} Y_{\mathrm{H_2S}} \, r \, dr = \sum_{i=1}^{N} A_i \, \rho_i \, v_{z,i} \, Y_{H_2S,i} \tag{A18}$$

The element contributions were summed up within Excel.

The following are the results from the base case, a reactor height of 0.82 mm and the case of an expanded height of 4.0 mm. A sticking coefficient of H_2S of 1 is assumed in both cases. The results are practically identical indicating that the reactor height does not influence the total amount of H_2S consumed. Note, though the total consumption is nearly identical, the sulfidation profiles on the coupon produced by the two cases are very different (Figure A6). The 0.82 mm case demonstrates a doughnut profile near the center, while the 4.0 mm case has a much more uniform profile. The 4.00 mm case has a larger deposition at intermediate radii to make up for the lack of the doughnut profile.

MPSalsa Program Notes: The total mass balance was really quite good. In minus Out was balanced to at least 6 significant figures. It is not worthwhile to expect anything better considering all of the file I/O needed to get to this answer, and considering some of the intermediary steps may have introduced rounding errors. To get a better mass balance would require a calculation carried out within MPSalsa of the total flux through a side set. This calculation hasn't been installed yet, but it doesn't look very hard to get it installed. The element balance on Sulfur that can be calculated from Table A1 seems to be more problematic. It is off at the 0.7% level for both case studies. Moreover, the stefan flow at the end node of the coupon was clearly in error. Note, the coupon Sulfur mass fluxes were calculated via the calculation of the surface reaction rate from the rate constant and the H_2S mass fraction. Thus, though, it did not involve using the stefan-flow velocity at the surface, the sulfur mass balance was still slightly in error.

Table A1. Integrated Flux Analysis of Sulfidation Experiments Assuming Unity Sticking Coefficient

Height	**Inlet (gm H2S / s)**	**Coupon (gm H2S/ s)**	**Outlet (gm H2S / s)**	**Fraction Consumed**
0.82	5.0155784E-9	2.74323E-9	2.2422410E-9	0.447
4.0	5.01558E-9	2.71912E-9	2.25844E-9	0.450

A3.4 Dependence on the Surface Reaction Rate Constant

As the surface reaction rate decrease the fraction of unconsumed H_2S in the gas increases. Figure A7 presents this dependence under the base case conditions. The MPSalsa model is displayed in red, while a back-of-the-envelope model is displayed in black. The simple model compares the total flux into the reactor to the total possible flux consumed by the surface reaction assuming the outlet concentration of H_2S is available to the surface. Thus, the simple CSTR model does not include any mass transport resistance, but does employ a rough mass balance on the available sulfur.

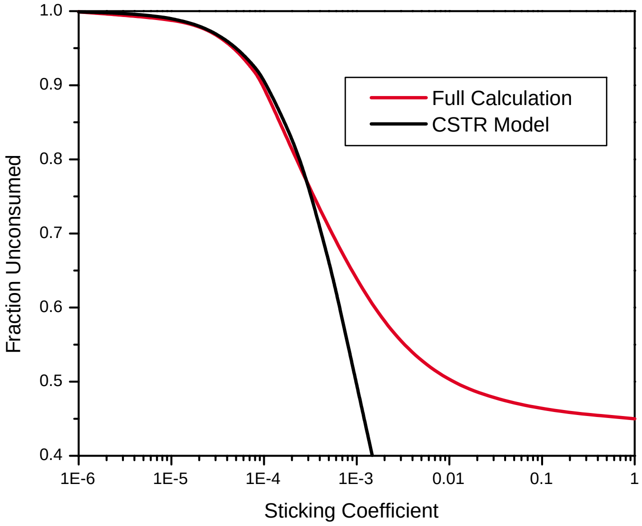

Figure A7. Fraction unconsumed versus sticking coefficient.

The flow rate of H_2S into the reactor under base case conditions, $MF_{\mathrm{H_2S}}$, is equal to the total mass flux into the reactor, *TMF*, multiplied by the mass fraction of H_2S, $Y_{\mathrm{H_2S}}$.

$$MF_{\mathrm{H_2S}} = TMF \quad Y_{\mathrm{H_2S}} \qquad \text{where} \tag{A19}$$

$$\begin{aligned} TMF &= v\ A_{\mathrm{inlet}}\ \rho = \left(3.59503\,\frac{\mathrm{cm}}{\mathrm{sec}}\right)\left(5.067074\ \mathrm{cm}^2\right)\left(1.144\times10^{-3}\,\frac{\mathrm{gm}}{\mathrm{cm}^3}\right) \\ &= 2.0839\times10^{-2}\,\frac{\mathrm{gm}}{\mathrm{s}} \end{aligned} \tag{A20}$$

The area of the coupon is equal to $A_{coupon} = 1.722013\ \mathrm{cm}^2$. The molecular weight of H_2S is equal to 34.082 gm mol^{-1}. The effusive flux of H_2S molecules hitting the surface, $F_{effusive}$, is equal to

$$\begin{aligned} F_{effusive} &= \text{effusive flux rate constant} = \tfrac{1}{4}\hat{v}_{\mathrm{H_2S}} = \sqrt{\frac{RT}{2\pi W}} \\ &= \left[\frac{\left(8.3134\times10^{7}\ \frac{\mathrm{gm\ cm^2}}{\mathrm{s^2\ mol\ K}}\right)\ 298.15\ K}{2\ \pi\ \left(34.082\ \mathrm{gm\ mol^{-1}}\right)} \right] \quad . \\ &= 8.3134\times10^{4}\ \mathrm{cm\ s^{-1}} \end{aligned} \tag{A21}$$

Then, $F_{effusive}$ may be employed to calculate the a surface reaction rate based on a reactive sticking coefficient for H_2S, γ, Eqn. 22.The denominator is a correction to the normal expression due to the breakdown in the Maxwell-Boltzman velocity distribution near a high-sticking coefficient surface [A4].

$$k_{effusive} = F_{effusive}\ \left(\frac{\gamma}{1-\frac{\gamma}{2}} \right) \tag{A22}$$

Thus the total mass flux loss rate due to surface reactions is equal to

$$\begin{aligned} Rate_{surface} &= k_{effusive}\ A_{coupon}\ \rho\, Y^{\mathrm{s}}_{\mathrm{H_2S}} = \left(\frac{\gamma}{1-\frac{\gamma}{2}} \right) \left(21.194\ \frac{\mathrm{gm}}{\mathrm{s}} \right) Y^{\mathrm{s}}_{\mathrm{H_2S}} \\ &= k_s\ Y^{\mathrm{s}}_{\mathrm{H_2S}} \end{aligned} \tag{A23}$$

$Y^{\mathrm{s}}_{\mathrm{H_2S}}$ expression stands for the mass fraction of H_2S at the surface. Assuming that the mass fraction at the surface is equal to the mass fraction of H_2S in the effluent stream, $Y_{\mathrm{H_2S}}$, (CSTR assumption), we may calculate $Y^{\mathrm{s}}_{\mathrm{H_2S}}$ from the following expression representing an overall total continuity equation for H_2S in the reactor.

$$TMF\ Y_{\mathrm{H_2S}} = k_s\ Y^{s}_{H_2S} + TMF\ Y^{s}_{H_2S} \tag{A24}$$

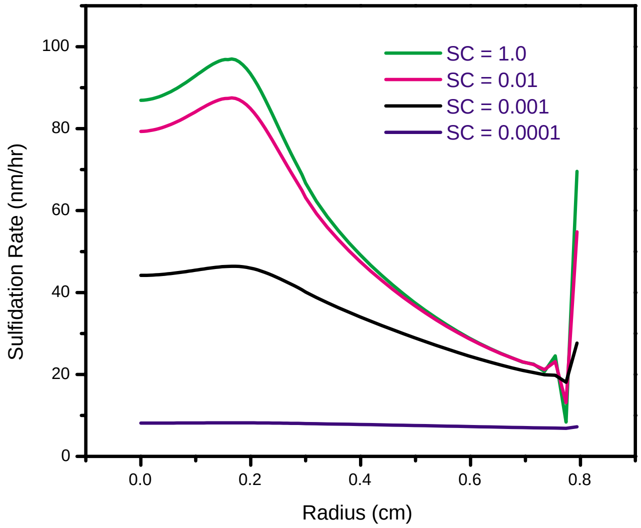

Figure A8. Variation of the layer thickness as a function of radius for various sticking coefficients.

$$Y^s_{H_2S} = \frac{TMF\ Y_{\mathrm{H_2S}}}{k_s + TMF} \tag{A25}$$

Thus, the mixing-cup fraction in the effluent that is unreacted can be calculated from Eqn. . This is the equation that is plotted in Figure A7.

$$\text{Fraction Unconsumed} = \frac{Y^s_{H_2S}}{Y_{\mathrm{H_2S}}} = \frac{TMF}{k_s + TMF} \tag{A26}$$

Figure A8 presents the growth rate as a function of the radius for various values of the sticking coefficient. one can see that if the sticking coefficient were reduced to 0.0001 (i.e., by lowering the oxygen content in the gas), then the assumption of a uniform growth rate may be made.

A4. Dependence on Inlet Velocity

The base case employed a total velocity of 1.0 slpm. Other experimental data at velocities of 0.5 slpm and 2.0 slpm were taken at a relative humidity level of 50%. I evaluated the dependec of the numerical model on the total flow rate. Note, in the tables below, I assumed that the inlet H_2S concentration was always 200 ppb, even when presenting the experimental numbers. Table A2 contains the numerical results assuming mass transport limiting growth. The last column in the table, Fraciton Unconsumed, is the actual experimental observable.

Table A2. Flow Rate Dependence Assuming Mass Transport Control

Flow Rate	H2S In (gm s-1)	H2S Out (gm s-1)	Mass Dep. (gm s-1)	GR (nm h-1)	Fraction Unconsumed
0.5 slpm	2.523348E-9	9.0517E-10	1.61818E-9	24.52	0.35872
1.0 slpm	5.01558E-9	2.25919E-9	2.75638E-9	41.76	0.45043
2.0 slpm	1.00934E-8	0.58494E-9	4.50845E-9	68.30	0.55333

Another way to analyse the data would be to first calculate the sticking coefficient that matches the Fraction Unconsumed, 0.61, measured in the experiment at the base flow conditions of 1 slpm with a relative humidity of 50%. This sticking coefficient, found by interpolating the line in Figure A2, turns out to be close to 1.7E-3. Then, use this sticking coefficient in the numerical model to compare the effect of the flow rate on the numerical model predictions versus the experimental measurements. The results of this analysis are presented in Table A3.

Table A3. Flow Rate Dependence Assuming a Sticking Coefficient of 0.0017

Flow Rate	H2S In (gm s-1)	H2S Out (gm s-1)	Mass Dep. (gm s-1)	GR (nm h-1)	Fraction Unconsumed
0.5 slpm	2.523348E-9	1.11527E-9	1.4081E-9	21.33	0.4420
1.0 slpm	5.01558E-9	2.8398E-9	2.2658E-9	34.33	0.5630
2.0 slpm	1.00934E-8	6.9021E-9	3.1913E-9	48.35	0.6838

The observed experimental flow rate dependence is presented in Table A4

Table A4. Flow Rate Dependence

slpm	FU 10 hour	FU lowest	FU highest	in	out	Mass Dep.	nm h-1
0.5	0.586	0.525	0.67	2.523E-9	1.4785E-9	1.044E-9	15.82
1.0	0.61	0.584	0.63	5.016E-9	3.0598E-9	1.956E-9	29.64
2.0	0.77	0.676	0.788	1.009E-8	7.769E-9	2.321E-9	35.17

FU 10 hour, the observed fractional unconsumed at 10 hours, was used fill in the last three columns of the table, i.e., to estimate the mass of sulfur deposited, and thus the sulfidation rate.

I redid the numerical flow rate studies using a sticking coefficient of 0.001. The results are shown in Table A5

Table A5. Sticking Coefficient of 0.001

Flow Rate	H2S In (gm s-1)	H2S Out (gm s-1)	Mass Dep. (gm s-1)	GR (nm h-1)	Fraction Unconsumed
0.5 slpm	2.523348E-9	1.23154E-9	1.29181E-9	19.568	0.48806
1.0 slpm	5.01558E-9	3.08477E-9	1.93081E-9	29.25	0.61504
2.0 slpm	1.00934E-8	7.44766E-9	2.64574E-9	40.077	0.73787

To compare, I carried out a flow rate dependence study assuming a sticking coefficient of 0.0002. Table A6 contains the results of these calculations. Figure A9 contains the complete dependence of the fraction unconsumed versus sticking coefficient for the case of the three different velocities studied.

Table A6. Sticking Coefficient of 0.0002

Flow Rate	H2S In (gm s-1)	H2S Out (gm s-1)	Mass Dep. (gm s-1)	GR (nm h-1)	Fraction Unconsumed
0.5 slpm	2.523348E-9	1.8202E-9	0.70314E-9	10.651	0.7213
1.0 slpm	5.01558E-9	4.1897E-9	0.82588E-9	12.510	0.83018
2.0 slpm	1.00934E-8	9.1159E-9	0.97750E-9	14.807	0.9032

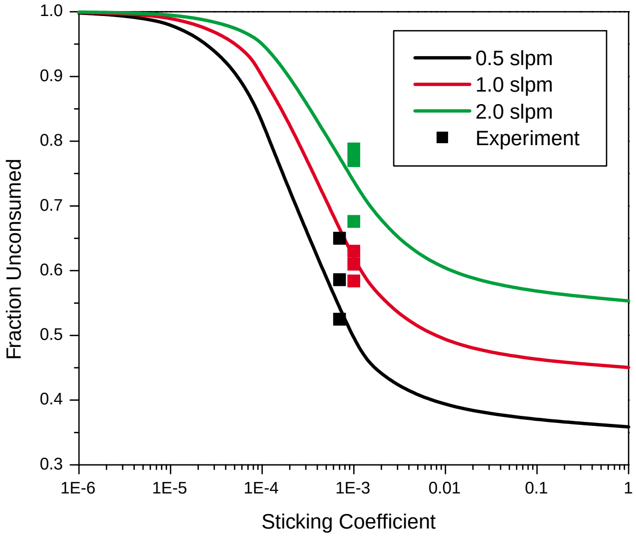

Figure A9. Velocity Dependence at a relative humidity of 50%.

Also shown are the experimental results for the three velocities. The value of the fraction unconsumed varied as a function of time for the three cases. The minimum, 10 hour, and maximum values of the fraction unconsumed values are shown on the plot for each of the three velocities. There is a lot of scatter in the data. However, we can begin to believe that the sticking coefficient for H_2S on the surface under these conditions is roughly 1.0×10^{-3} to within a factor of 5. There is also a trend towards decreasing sticking coefficients as a function of time by roughly a factor of 3 over the experiment. It's probably dangerous to presume much more from the data than these rough numbers, given the scatter in the data and the fact that the data encompasses a great deal of non uniformity vs. radius (roughly a factor of 2, see Figure A8). The next step in the analysis would be to try to extract a sticking coefficient versus layer thickness relationship. However, uncertainties in absolute growth rates discussed later as well as the non-uniformity issue would hinder the accuracy of the analysis.

To sum up, the dependence on velocity study was more inconclusive than I had hoped. The consistency in the experimental numbers and the sticking coefficient really cannot be narrowed down via this method due to the lack of variation in the dependence of the fraction unconsumed as a function of velocity for varying sticking coefficients. However, we can definitely say that the sticking coefficient is roughly 0.001 within a factor of 5, and fair agreement of the experimental results with the numerical model is achieved for the dependence on velocity.

A5. Numerical Convergence Study

Due to the problematic behavior of the growth rate versus radius plots (see Figure A6), a convergence study is needed to ensure that the bottom line results are not affected. Thus, the mesh was refined about the coupon corner. Figure A10 displays the results of the study. (Note, another refinement of the mesh is under construction. However, the tflops machine has to be used, because the problem becomes too large for zuzax). Unfortunately, the problematic behavior did not go away as the mesh was refined about the corner point. Yes, it did get squashed into a smaller region about the corner. However, if there is any trend at all, the gyrations in surface H_2S concentration got worse as the mesh was refined. Note, in the refined grid simulation, the sulfidation rate went to zero on the node adjacent to the corner. The H_2S mass fraction was negative. This behavior is most likely due to a bug in the specification of the Stephen velocity alluded to earlier in this memo, and may also be the cause of the lack of elemental sulfur conservation. The Stephen flow velocity at the corner node appeared to be a factor of two lower than it should have been. In order to compensate for the lower mass average velocity and still satisfy the integrated boundary condition on the coupon, a counteractive diffusive flux of H_2S must be set up that causes the neighboring nodal values of H_2S mass fraction to be in error.

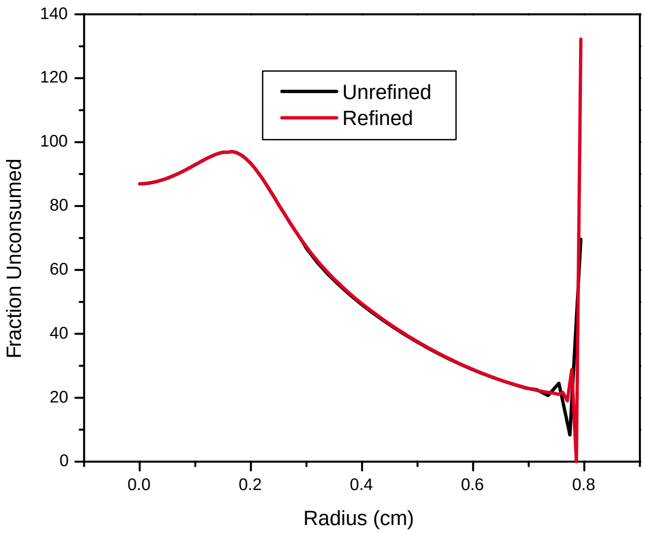

Figure A10. Convergence study: effect of doubling the mesh density near the problematic corner.

While the point convergence with mesh refinement didn't appear to occur, the integrated quantities, such as the experimental measurable fraction of H_2S consumed did appear to have been converged even on the coarsest mesh used. Table A7 contains the results.

Table A7. Convergence Study: Integrated Quantities

Quantity	Unrefined	Refined
# Nodes	15254	18206
Exit MF	2.061378E-2	2.061378E-2
Exit H2S MF	2.258437E-2	2.259193E-9
Inlet MF	2.061380E-2	2.061380E-2
Inlet H2S MF	5.015578E-9	5.015578E-9
Fraction Unconsumed	0.4502665	0.4504352

Note, another refinement of the mesh is under construction. However, the tflops machine has to be used, because the problem becomes too large for zuzax.

A6. Analysis of the Humidity Dependence

Figure A11 displays the experimental data taken as a function of the relative humidity level at the base velocity of 1 slpm. The data was normalized via the first data point for H_2S effluent concentration, where presumably the H_2S sticking coefficient is so low that no loss of H_2S in the reactor occurs. The data in Figure A11 exhibits many interesting trends. It clearly demonstrates that phase 2 only occurs for the high humidity level cases, with the transition roughly in the 60 to 70% humidity level. At the low humidity level cases, there is a complex dependence of the sulfidation rate as a function of humidity level. For example, perhaps a maximum at 60% is observed. Also, the establishment of Phase 1, presumably via loss or conversion of the native oxide is a roughly linear function of the humidity level (with high being good). Thus, high humidity levels promote the initial destruction of the native oxide.

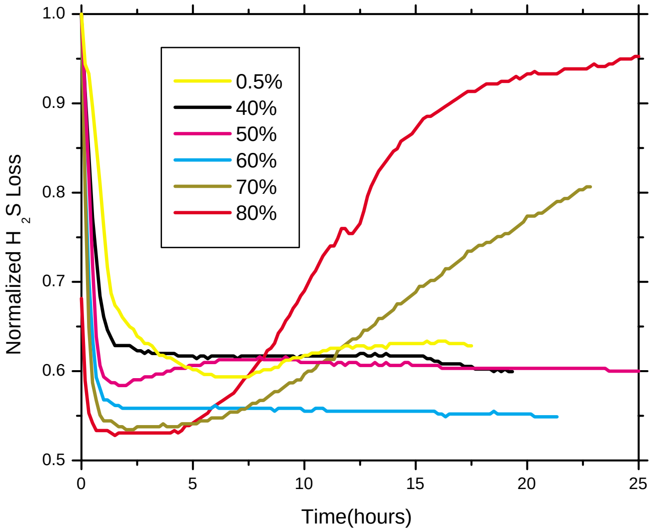

Figure A11. Fraction H_2S lost versus time as a function of varying humidity.

To convert the data in Figure A11, Figure A7 may be used as lookup table. I did this via an Excel spreadsheet. The results are presented in Figure A12

The high relative humidity cases exhibit a significant time-dependent sticking coefficient. Therefore, the sticking coefficient depends on thickness here. Thus, a case may be made that the thickness at every radius has to be followed in order to develop a model wherein the surface

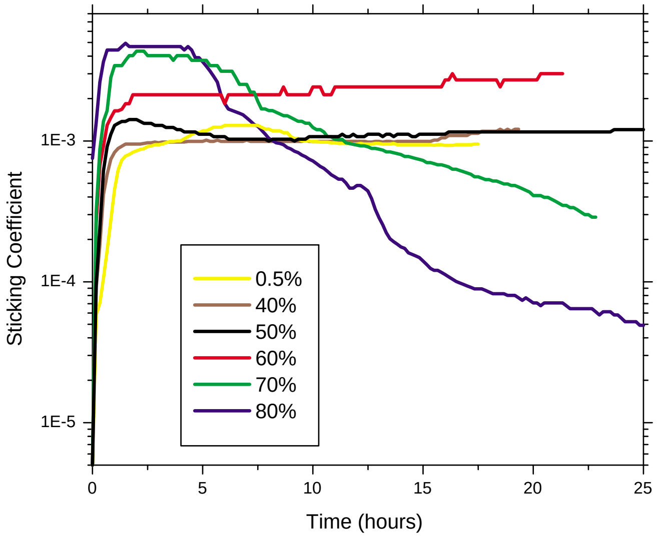

Figure A12. Sticking coefficient versus time for runs with the base case velocity as a function of the relative humidity. Note, the effusive flux of H_2S is $1.08 \times 10^4 \text{ cm s}^{-1}$. To obtain the surface reaction rate constant, multiply the sticking coefficient by the effusive flux.

reaction rate is a function of the existing thickness of the layer, and thus is a function of both the radius and the time. However, that analysis was not carried out here, because it seemed premature to spend significant amounts of resources analyzing data for which better data may be forthcoming after an additional tweaking of the experiment. Also, following the sticking coefficient as a function of layer thickness would necessarily involve predicting the absolute concentration of H_2S at the inlet of the reactor, a number which currently has a significant level of uncertainty to it.

A7. Uncertainties in the Corrosion Rate Calculation

Doing combinatorial experiments on this system will be extremely problematic until we can lower the surface reaction rate constant down either by lowering the oxygen content of the gas or by pretreating the surface to force the reaction into the slower stage 2 growth conditions. The reason why it the combinatorial experiments are hard is that each experiment would inevitably see a different gas-phase environment due to the fast overall surface reaction rate constant, and the gas- phase environment matters for high surface reaction rate constants.

The fraction unconsumed vs. sticking coefficient plot is the most accurate way to represent the data. It sidesteps a big problem, because only relative changes in the effluent H_2S concentration are used. The absolute measurement of the H_2S partial pressure entering the chamber is quite uncertain. And, a derivation of the sticking coefficient from the growth rate would necessary involve a determination of the entrance H_2S partial pressure to first order way. A determination of the sticking coefficient as a function of layer thickness would necessarily involve a determination of the absolute value of the H_2S partial pressure, because the layer thickness depends on a calculation of the growth rate.

There are several reasons for the uncertainty in the absolute value of the H_2S partial pressure.

The principle reason is that the signal from the sulfur elemental detector varies as a function of humidity, all other flow rates being held constant. Where the sulfur is lost as the humidity in the gas stream is increased is uncertain. There are two possible mechanisms. The first possibility is that H_2S is adsorbed uniformly on the walls of the tubing both before the reactor and after the reactor in a thin water layer adsorbed on the walls of the poly-piping. However, the observed H_2S from the detector was not observed to change as a function of time even after prolonged period of time of flowing the feed gasses directly into the detector. Thus, we will discount this possibility. The second possibility is that part of the H_2S is taken out of the effluent gas stream during the drying process, which is carried out immediately prior to measuring the sulfur content of the effluent. Hopefully, the removal of the H_2S in the drying process involves a linear relation so that the linearity of the detector is maintained! If this second possibility is the dominant reason for the apparent drop in measured H_2S concentration as a function of humidity, then we may make a linear multiplicative correction to the measured H_2S concentration to derive the actual H_2S concentration in the effluent to make the best of an uncertain situation. Thus, without placing the coupon in the reactor, we measure the content of H_2S under dry gas conditions. Then, we turn up the humidity to the desired value and measure the H_2S concentration again. We then apply the quotient of these two numbers at a given flow rate and humidity level to derive the "actual" H_2S concentration from the "measured" H_2S concentration. Then, we use the actual H_2S concentrations in the modeling of the growth rates and surface reaction rates as a function of layer thicknesses.

The other reason for the H_2S partial pressure uncertainty is the uncertainty in the calibration settings of the rotameter used to monitor the total flow rate. I used and assumed the definition of "standard liters per minute" commonly and uniformly used by the semiconductor industry, i.e., 1 standard atmosphere at 0 C. However, the rotameters may not have been calibrated with respect to that standard. The calibration method that was used seemed to be uncertain. Therefore, I stuck to the slpm standard mentioned above. Errors due to rotameter calibration issues could be on the order of 15%.

A8. Recommendations

The stagnation point for reactor is starting to produce good results. However, several refinements are still required. Redesign the susceptor by halving the radius of the current copper coupon and then encase it in lucite (Bill Breiland's suggestion). This will allow the growth rate to be more uniform over the radius than currently.

Understand the current uncertainties in the measurement of the absolute partial pressure of H_2S mentioned in Section A7. Measure the sulfidation rate of the coupon via another technique and try to correlate H_2S partial pressure, growth rate, and sticking coefficient measured here with each other. My prediction is that there will be serious issues with this correlation that should be worked out.

Reconcile different growth rate measurement techniques with each other. The in situ reflectance measurement technique is very powerful, but it has yet to be benchmarked against any other technique.

The result we are working to achieve is an apparatus and experimental technique that can reliably give us surface reaction rates as a function of layer thickness and gaseous reactants at the surface of the growth film. Once we achieved that goal, then models for the kinetics and transport in the product layer may be reliably validated.

A9. References

A1. H. K. Moffat, W. G. Breiland, “Analysis of a Stagnation Point Flow Reactor Design for use in Combinatorial Corrosion Experiments”, Sandia Memo, Sept. 30, 1999.

A2. *Handbook of Chemistry and Physics*, 73rd Ed., D. R. Lide Ed., CRC, Boca Raton 1993.

A3. M. E. Coltrin, R. J. Kee, F. M. Rupley, E. Meeks, “Surface Chemkin-III: A Fortran package for analyzing heterogeneous chemical kinetics at a solid-surface gas-phase interface,” Sandia Report, SAND96-8217, Albuquerque, NM, May 1996.

A4. *Transport Phenomena*, R. B. Bird, W. E. Stewart, and E. N. Lightfoot, J. Wiley Sons, New York, 1960.

APPENDIX B – Listing of Cu Sulfidation Kinetic Experiments

Phase A – all at ambient temperature in Bldg 806

Sample	**RH (%)**	**$[H_2S]_{set}$ (ppb)**	**$[H_2S]_{init}$ (ppb)**	**Flow Rate (sccm)**	**Temp (°C)**	**Δt (hours)**	**Sample type**	**Pickle (y/n)**	**Polish date**	**Thick (nm)**	**Comments**	**Disposition**
File: CuS - 805												
6-29-00a	0.5	400		1000	ambient	22					3% O2	repolish 1-16-01
6-30-00a	0.5	200		1000	ambient	120						sem
7-5-00a	0.5	200		1000	ambient	22						sem
7-6-00a	0.5	100		1000	ambient	19						repolish 1-16-01
7-7-00a	80.0	200		1000	ambient	67						
7-10-00a	40.0	200		1000	ambient	22						repolish 1-16-01
7-13-00a	70.0	200		1000	ambient	23						
7-14-00a	50.0	200		1000	ambient	64						
7-17-00a	60.0	200		1000	ambient	21						repolish 3-7-01
7-18-00a	60.0	200		1000	ambient	24						repolish 1-16-01
7-19-00a	50.0	200		2000	ambient	21						repolish 1-16-01
7-20-00a	50.0	200		500	ambient	22						repolish 1-16-01
7-21-00a	60.0	200		1000	ambient	72						
7-24-00a	50.0	100		1000	ambient	17						repolish 1-16-01
7-25-00a	20.0	200		1000	ambient	19						repolish 3-7-01
7-26-00a	50.0	400		1000	ambient	18						repolish 1-16-01
7-28-00a	20.0	200		1000	ambient	144						
8-03-00a	50.0	10		1000	ambient	96						repolish 3-7-01
8-10-00a	50.0	14		1000	ambient	25					equiv. Dose	
8-11-00a	50.0	133		1000	ambient	2.2					equiv. Dose	
8-17-00a	50.0	14		1000	ambient	258						

Phase B – performed in an incubator in Bldg 701

12-20-00a	0.5	200	187	1000	ambient	4	tf	n	--		Barbour ID 11/14/00	
12-21-00a	80.0	200	188	1000	ambient	4	tf	n	--		Barbour ID 11/22/00	
12-22-01a	0.5	200	187	1000	ambient	6	button	n	Aug-00		no pickle, as rec'vd from Alice	
1-2-01a	0.5	200	190	1000	ambient	20	"	y	Aug-00		pickle only	
1-3-01a	0.5	200	199	1000	ambient	21	"	y	Aug-00		sanded with 4000 grit	repolished 3-7-01
1-4-01a	0.5	200	197	1000	ambient	20	"	y	Aug-00		4000 grit sanding + zero air from cylinder	
1-5-01a	80.0	200	186	1000	ambient	5	"	y	Aug-00		zero air from cylinder	
1-9-01a	80.0	200	199	1000	ambient	21	"	y	Aug-00		back to dry house air	repolished 3-7-01
1-12-01a	0.5	200	201	1000	ambient	74	"	y	Aug-00		Re-polish 9-10-01 in house by s. lucero	
1-17-01a	50.0	168	159	1000	ambient	221	"	n	Aug-00			
1-26-01a	0.5	168	153	1000	ambient	63	"	y	Jan-01		Newly polished buttons (all on opposite side)	repolished 3-7-01
1-31-01a	0.5	168	160	1000	27	23	"	y	Jan-01			
2-1-01a	0.5	200	206	1000	27	95	"	y	Jan-01		2-5-01 lowered temp. to 20 °C for 7hrs.	repolished 3-7-01
2-5-01a	0.5	200	200	1000	27	23	"	n	Aug-00			
2-6-01a	0.5	200	200	1000	20	41	"	y	Jan-01			
2-1-01b	0.5	200	202	1000	20	24	"	n	Jan-01		Continue exposure of 2-1-01a.	
2-9-01a	0.5	200	201	1000	24	25	"	y	Jan-01			
2-10-01a	0.5	200	201	1000	ambient	44	"	y	Jan-01		Replicate of 1-26-01. Acquired temp. data.	repolished 3-7-01
2-12-01a	0.5	200	168	1000	ambient	39	"	y	Jan-01		Countertop temp	repolished 3-7-02
2-14-01a	0.5	200	157	1000	ambient	43	"	y	Aug-00		Countertop temp	repolished 3-7-03

2-16-01a	0.5	200	184	1000	33.7	68	"	y	Jan-01	1670		
2-20-01a	50.0	200	161	1000	34.2	20	"	y	Jan-01			
2-21-01a	80.0	200	150	1000	34.5	20	"	y	Jan-01			
2-22-01a	0.5	200	180	1000	15	88	"	y	Jan-01			To C.B. for RBS 3-1-01
2-26-01a	80.0	200	170	1000	15	21	"	y	Jan-01			To C.B. for RBS 3-1-01
2-27-01t	80	200	180	1000	15	4	tf	n	--	109		To C.B. for RBS 3-1-01
2-28-01t	0.5	200	180	1000	15	6	tf	n	--	87		To C.B. for RBS 3-1-01
3-01-01t	80.0	200	161	1000	15.8	4	tf	n	--	84		To C.B. for RBS 3-7-01
3-02-01t	80.0	200	160	1000	25	4	tf	n	--	84		To C.B. for RBS 3-7-01
3-02-01a	60	200	166	1000	ambient	65	button	y	1-Jan	363		repolished 3-7-01
3-05-01t	80	200	152	1000	35	4	tf	n	na	54		To C.B. for RBS 3-7-01
3-06-01t	0.5	200	184	1000	35	4.7	tf	n	na	110		To C.B. for RBS 3-7-01
3-07-01t	0.5	200	184	1000	25.1	4.9	tf	n	na	106		To C.B. for RBS 3-7-01
3-08-01t	0.5	200	186	1000	5	23.3	tf	n	na	169		To C.B. for RBS 3-12-01
3-09-01a	0.5	200	196	1000	5	72	button	n	Aug-00	64	has not been charted.	To C.B. for RBS 3-12-01
3-13-01a	80	200	164	1000	5	42.7	button	n	Aug-00	103	has not been charted. Save	Save 6-18-01
3-15-01a	80	200	163	1000	5	93	button	y	1-Mar	456		
3-19-01t	80	200	157	1000	24.2	0.5	tf	n	na	0.5	3nm thick exposure for Nancy Missert	To Nancy M. for analysis
3-22-01t	0.5	200	176	1000	25.7		tf	n	na		3nm thick exposure for Nancy Missert	To Nancy M. for analysis
3-23-01a	0.5	200	177	1000	25.7	0.42	button	n	1-Mar	2.6		Re-polished 6-18-01
3-26-01s	0.5	200	177	1000	24.8	7	masked button	n	1-Mar	?	Exposed for John Sullivan. Shoot for 1000 nm thickness	
3-27-01s	0.5	200	177	1000	24.8	5.5	masked button	y	1-Mar	?	pickled and re-exposed 3-26-01s button.	To J. Sullivan for analysis
3-28-01t	0.5	200	177	1000	24.8	2	tf	n		?	3-22-01t additional-exposure for N.M.	To Nancy M. for analysis
4-4-01t	80	200	163	1000	5.3	6.5	tf	n		Add	For C.B.	
4-5-01t	80	200	163	1000	19.9	4	tf	n		98.5	For C.B.	
4-6-01a	80	200	177	1000	5.3	69	masked button	y	1-Mar			Re-polished 6-18-01
4-9-01a	50	200	178	1000	15	21	masked button	y	1-Mar			Re-polished 6-18-01
4-13-01a	0.5	400	336	1000	24.7	100	masked button	y	1-Mar		no H2S data logged due to scale error	
4-17-01a	0.5	400	347	1000	25.6	20	masked button	y	1-Mar		repeat of above. Attempt to get front end data for above.	
4-18-01a	0.5	200	181	1000	25.5	49.6	masked button	y	1-Mar	248	replace inpingement chamber w/ 500ml GES jar.	Save 6-18-01
4-20-01a	50	200	173	1000	25.5	90	Cu strip	y	n/a	?	500ml exposure jar	
5-4-01a	50	200	182	1000	25	235	masked button	y	1-Mar	4337		probably given to Nancy.
5-14-01a	70	200 classIII	154	1000	22.4	27	masked button	y	1-Mar	299	Temp. chamber cooling malfunction	Re-polished 6-18-01
5-14-01b	70	200 classIII	140	1000	29.9	358	masked button	y	1-Mar	5166		
6-1-01a	70	200	131	1000	25.8	137	masked button	y	1-Mar	1951		Re-polished 6-18-01
6-7-01a	80	200	146	1000	25.7	23.7	masked button	y	1-Mar	202	looking into effect of Breiland laser vs break - still lighted	
6-8-01a	80	200	158	1000	25.8	67.2	masked button	y	1-Mar	258	looking into effect of Breiland laser vs break - still lighted	
6-11-01a	0.5	200	146	1000	25.8	334	masked button	y	1-Mar	334	looking into effect of Breiland laser vs break - still lighted	
6-29-01a	70	200	172	1000	24.9	66.3	masked button	y	1-Jun	492	looking into effect of Breiland laser vs break. Observed that Bill's monogrow light is still present in reaction chamber w/o a software start. Physically shutoff the monogrow power supply.	
7-2-01a	50	200	218	1000	25	95	masked button	y	1-Jun	1318	Repeat of 6-29-01a, at 50% rh, no Breiland light.	
7-6-01a	70	200	174	1000	24	67	masked button	y	1-Jun	346	Repeat of 6-29-01a, at 70% rh, no Breiland light and better data resolution.	
7-9-01a	60	200	186	1000	25.3	93	masked button	y	1-Jun	1642	Repeat of 6-29-01 at 60% rh, no light.	
7-13-01a	70	100	96	1000	24.5	64	masked button	y	1-Jun	327	Repeat 7-6-01a with decreased H2S concentration.	
7-17-01a	0.5	200	184	1000	24.5	571	masked button	y	1-Jun	8807	100 ppm O2 supply with bottle. Conditions were changed 5 times, see log book.	
8-10-01a	60	200	190	1000	25.5	69.4	masked button	y	1-Jun	397	No light	
8-14-01a	0.5	200	194	1000	25.4	150	masked button	y	1-Jun	1271	No light	
8-22-01a	20	200	194	1000	25.4	168	masked button	y	1-Jun	653	No light	
8-31-01t	0.5	200	180	1000	25.5	4.85	tf	n	na	20.2	No light	
8-31-01a	0.5	200	178	1000	25.7	166.6	masked button	y	1-Aug	2333	No light. Used a new Metal Samples Cu button.	
9-7-01a	50	200	178	1000	25.6	71	masked button	y	1-Aug	729.8	No light. Used a new Metal Samples Cu button. Limited data acquired.	
9-10-01a	50	200	178	1000	25.8	18	masked button	y	1-Aug	249	No light. Used a new Metal Samples Cu button.	
9-13-01t	0.5	200	178	1000	15.8	19	tf	n	na	101	No light	

9-14-01s	0.5	200	176	1000	15.3	5	tf meander	n	na	?	No light, area not known
9-14-01a	80	200	153	1000	25.8	66	masked button	y	1-Aug	256	No light. Used a new Metal Samples Cu button.
9-17-01t	80	200	158	1000	25.2	4.7	tf	n	na	75	No light
9-18-01t	80	200	140	1000	35.6	5.8	tf	n	na	55	No light. Button reached plateau at 3 hrs. / 50nm then stage 2 @ 4hrs
9-19-01t	80	200	165	1000	15.7	3.9	tf	n	na	96	No light
9-19-01s	80	200	166	1000	15.7	15	tf meander	n	na	??	No light
9-21-01s	0.5	200	181	1000	15.7		tf meander	n	na	??	this sample is a continuation of sullivan 1 (9-14-01s)
9-24-01t	60	200	192	1000	24.6	5.95	tf	n	na	98	No light
9-25-01a	60	200	191	1000	24.8	~48	masked button	y	1-Aug	Na	No light. Terminate test due to dry air loss. No data
9-26-01a	60	200	192	1000	24.9	115	masked button	y	1-Aug	2007	No light. Repeat of 7-9-01 with a new metal samples button.
10-02-01t	0.5	200	196	1000	35.4	**	tf	n	na	**	No light. **Data has not been reduced. See logbook
10-05-01a	0.5	200	198	1000	25.2	313	masked button	y	1-Aug	4533	No light.
10-22-01a	0.5	200	212	1000	24.98	17.9	masked button	y	1-Aug	12.8	No light. 1 ppm O2, balance N2
10-23-01a	0.5	200	224	1000	25.1		masked button	y	1-Aug	11.7	No light. 1 ppm O2, balance N2
10-25-01a	20	200	210	1000	24.89	on test	masked button	y	1-Aug	on test	No light. Repeat of 8-22-01a.

DISTRIBUTION

5	MS 1415	J. C. Barbour, 1112
1	MS 1421	J. P. Sullivan, 1112
1	MS 1415	N. A. Missert, 1112
1	MS 1415	M. J. Campin, 1112
1	MS 1415	A. F. Wright, 1112
1	MS 1415	R. G. Copeland, 1112
1	MS 0601	W. G. Breiland, 1126
1	MS 1415	T. M. Mayer, 1114
5	MS 0889	J. W. Braithwaite, 1832
1	MS 0888	S. J. Lucero, 1832
1	MS 0888	N. R. Sorensen, 1832
5	MS 0888	K. R. Zavadil, 1832
1	MS 0834	H. K. Moffat, 9114
1	MS 9018	Central Technical Files, 8945-1
2	MS 0899	Technical Library, 9616
1	MS 0612	Review and Approval Desk, 9612 for DOE/OSTI
2	MS 0188	C. L. Harvey McDonald, LDRD Office, 1030
2	MS 0885	D. B. Dimos, MS&T Council, 1801